

Measurement of the $K^+ \rightarrow \pi^+ \nu \bar{\nu}$ Branching Ratio

The E949 Collaboration

Abstract

The E949 experiment at Brookhaven National Laboratory (BNL) has collected 1.77×10^{12} K^+ exposure during its 2002 physics run. These data were analyzed via a blind analysis in order to obtain an unbiased background estimate in the signal box for the rare kaon $K^+ \rightarrow \pi^+ \nu \bar{\nu}$ of 0.30 ± 0.02 events. One candidate event is observed, giving an upper limit for the branching ratio $\mathcal{B}(K^+ \rightarrow \pi^+ \nu \bar{\nu}) < 8.8 \times 10^{-10}$ (90% CL). Combining with the other two candidate events observed by the predecessor E787 experiment gives the branching ratio $(1.47^{+1.60}_{-0.93}) \times 10^{-10}$, which is consistent with the Standard Model prediction of $(0.78 \pm 0.12) \times 10^{-10}$. The resulting limit on the magnitude of the Cabibbo-Kobayashi-Maskawa matrix element V_{td} is $0.0024 < |V_{td}| < 0.0322$ at 90% confident level.

Contents

1	Introduction	1
1.1	CP Violation and Rare Decay $K^+ \rightarrow \pi^+ \nu \bar{\nu}$	1
1.2	History of $K^+ \rightarrow \pi^+ \nu \bar{\nu}$ Experiments	5
2	Experimental Method	7
2.1	Overview	7
2.2	The Accelerator and K^+ Beam Line	9
2.3	Beam Counters	11
2.4	Target	15
2.5	Tracking Chamber	16
2.6	Range Stack	18
2.6.1	Scintillator Counters	18
2.6.2	Range Stack Straw Chambers	18
2.7	Photon Veto Counters	20
2.8	Trigger	23
2.8.1	General Trigger Conditions	23
2.8.2	$K^+ \rightarrow \pi^+ \nu \bar{\nu}$ Triggers	24
2.8.3	Monitor Triggers	25
2.9	Data Acquisition	27
2.10	Data Collection	29
3	Data Analysis	30
3.1	Overview of Background	30
3.1.1	Origins of Stopped K^+ Decay Background	30
3.1.2	Origins of Beam Background	30
3.2	Analysis Method and Strategy	34
3.2.1	Blind Analysis Method	34
3.2.2	Bifurcation Method for Evaluating Background	34
3.2.3	Analysis Strategy	36
3.3	Event Reconstruction	37
3.3.1	Clustering in RS	37
3.3.2	Tracking in UTC	37
3.3.3	Tracking in Target and B4	37
3.3.4	Track Passage in IC	38
3.3.5	Tracking in RS and RSSC	38
3.3.6	Kinematic Measurements of a Track	39
3.4	Monte Carlo Simulation	41
3.4.1	Simulation of K^+ Propagation	41
3.4.2	Simulation of K^+ Decay Product	41
3.4.3	Simulation of Trigger	41
3.4.4	Comparison between Data and Simulation	41
3.4.5	Simulation of Charge Exchange Reaction	41
3.5	Data Processing and Pre-selection	43
3.5.1	Filtering Data in Pass 1 Phase	43
3.5.2	Skimming Data in Pass 2 Phase	43

3.6	Selection Criteria of Post Pass 1 and Pass 2	45
3.6.1	Single K^+ Beam Requirements	45
3.6.2	Decay π^+ Kinematic Requirements	49
3.6.3	$\pi^+ \rightarrow \mu^+ \rightarrow e^+$ Decay Sequence	52
3.6.4	Photon Veto	59
3.7	Background Evaluation	63
3.7.1	$K_{\pi 2}$ Background	63
3.7.2	μ^+ Background	66
3.7.3	Single Beam Background	69
3.7.4	Double Beam Background	69
3.7.5	Charge Exchange Background	69
3.7.6	Total background Evaluated from One-Third Sample	70
3.7.7	Optimization of Signal Region	71
3.7.8	Correlation and Single Cut Failure Study	71
3.7.9	Final Background Evaluated from Two-Thirds Sample	73
3.7.10	Systematic Uncertainty	74
3.8	Acceptance and Sensitivity	76
3.8.1	Acceptance Factors from $K_{\mu 2}$ Events	76
3.8.2	Acceptance Factors from $K_{\pi 2}$ Events	77
3.8.3	Kinematic Acceptance Factors from Beam π^+ Events	78
3.8.4	$\pi^+ \rightarrow \mu^+ \rightarrow e^+$ Decay Acceptance from Beam π^+ Events	78
3.8.5	Acceptance Factors from Monte Carlo Simulation	78
3.8.6	Correction to $T \cdot 2$ Inefficiency	79
3.8.7	Normalization to $K_{\mu 2}$ Branching Ratio	79
3.8.8	Confirmation by $K_{\pi 2}$ Branching Ratio	80
3.8.9	Summary of Acceptance and Sensitivity	81
3.9	Examining Signal Region	82
4	Results	84
4.1	Likelihood Method	84
4.2	Branching Ratio of $K^+ \rightarrow \pi^+ \nu \bar{\nu}$	85
4.3	Implication for $\mathcal{B}(K^+ \rightarrow \pi^+ X^0)$	85
4.4	Impact on Unitarity Triangle	86
5	Conclusion	88
6	Acknowledgements	88

1 Introduction

Although the Standard Model (SM) has successfully accounted for all low energy CP-violating phenomena thus far observed, it fails as the source of the CP-violation needed to explain the cosmological baryon asymmetry in our universe[1]. According to Sakharov[2], one of the conditions necessary to generate such an asymmetry is that the elementary interaction violates charge conjugation symmetry (C) and the combined CP symmetry (where P is the parity symmetry). However, the size of the asymmetry needed for this cannot be derived in model calculations based on the SM[3] and new sources of CP violation have been sought for many years in particle physics experiments. Prominent among these are the rare decays $K \rightarrow \pi \nu \bar{\nu}$ which are sensitive to new physics involving both CP-violating and CP-conserving. In this paper, we describe the search for measurement of the reaction $K^+ \rightarrow \pi^+ \nu \bar{\nu}$ performed by Brookhaven National Laboratory experiment BNL-E949. This paper is arranged as follows. We first briefly review CP violation and rare kaon decays, with an emphasis on $K^+ \rightarrow \pi^+ \nu \bar{\nu}$ decays. We then describe previous results on this reaction and discuss the sources of potential background and the methods for suppressing backgrounds. We also discuss the design of the kaon beamline, the detector and the selection criteria used in data analysis and describe the methods used for estimating background levels and for evaluating the acceptance. After examining the signal region, we present the method used for extracting the branching ratio, making full use of our knowledge of the background in the signal region. In the last section, we will show how the measurement of $\mathcal{B}(K^+ \rightarrow \pi^+ \nu \bar{\nu})$ impacts the search for new physics beyond the SM.

1.1 CP Violation and Rare Decay $K^+ \rightarrow \pi^+ \nu \bar{\nu}$

Standard Model CP violation in flavor changing processes arises from a complex phase in the three-generation quark mixing matrix[4]. In the Wolfenstein parameterization[5] of the Cabibbo-Kobayashi-Maskawa (CKM) matrix, the parameters can be written in powers of $\lambda = \sin \theta_c \approx 0.22$:

$$V_{CKM} = \begin{pmatrix} V_{ud} & V_{us} & V_{ub} \\ V_{cd} & V_{cs} & V_{cb} \\ V_{td} & V_{ts} & V_{tb} \end{pmatrix} \simeq \begin{pmatrix} 1 - \lambda^2/2 & \lambda & A\lambda^3(\rho - i\eta) \\ -\lambda & 1 - \lambda^2/2 & A\lambda^2 \\ A\lambda^3(1 - \rho - i\eta) & -A\lambda^2 & 1 \end{pmatrix}. \quad (1)$$

where A , λ , ρ and η are real numbers. CP invariance of the Lagrangian for weak interactions is violated when the CKM matrix is complex. The parameter η quantifies CP violation in the SM.

The unitarity of the CKM matrix implies six unitarity conditions, which can be represented graphically in the form of triangles, all of which must have the same area. The area of these triangles is equal to one half of the Jarlskog invariant, J_{CP} [6]. Applying the unitarity property $V^\dagger V = 1$ to the CKM matrix in (1) yields

$$V_{ub}^* V_{ud} + V_{cb}^* V_{cd} + V_{tb}^* V_{td} \simeq V_{ub}^* - \lambda V_{cb}^* + V_{td} = 0, \quad (2)$$

where the approximations $V_{ud} \simeq V_{tb}^* \simeq 1$ and $V_{cd} \simeq -\lambda$ have been made. This equation can be represented graphically, as shown in Figure 1, where we have divided all of the sides by λV_{cb}^* . The apex of the triangle is given by two well-known Wolfenstein parameters, $\bar{\rho}$ and $\bar{\eta}$, where $\bar{\rho} = \rho(1 - \lambda^2/2)$ and $\bar{\eta} = \eta(1 - \lambda^2/2)$.

B's and K's are so far the only two mesons showing evidence of CP violation in their decay processes. Whether or not the observed CP violation can be completely explained by the CKM phase within the SM can be probed by the determination of ρ and η independently, from B and K decays as shown in Figure 2. Two sensitive methods for making the comparison are:

- A comparison of angle β from the ratio $\mathcal{B}(K_L^0 \rightarrow \pi^0 \nu \bar{\nu})/\mathcal{B}(K^+ \rightarrow \pi^+ \nu \bar{\nu})$ with that from the CP violating asymmetry (\mathcal{A}_{CP}) in the decay $B_d^0 \rightarrow J/\psi K_s^0$.
- A comparison of the magnitude $|V_{td}|$ from $K^+ \rightarrow \pi^+ \nu \bar{\nu}$ with that from the mixing frequencies of B_s and B_d mesons, expressed in terms of the ratio of the mass differences, $\Delta M_{B_s}/\Delta M_{B_d}$.

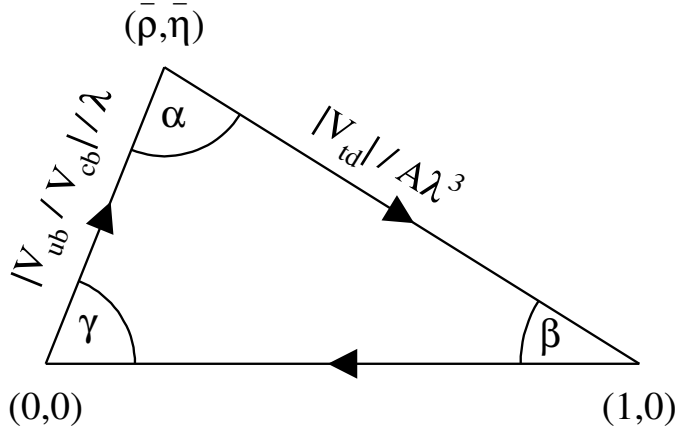


Fig. 1. Unitarity triangles in the ρ - η plane. Two sides of the triangle can be expressed by the CKM matrix elements $|V_{td}|/A\lambda^3$ and $|V_{ub}/V_{cb}|/\lambda$, respectively, where A and λ are parameters in the Wolfenstein parameterization.

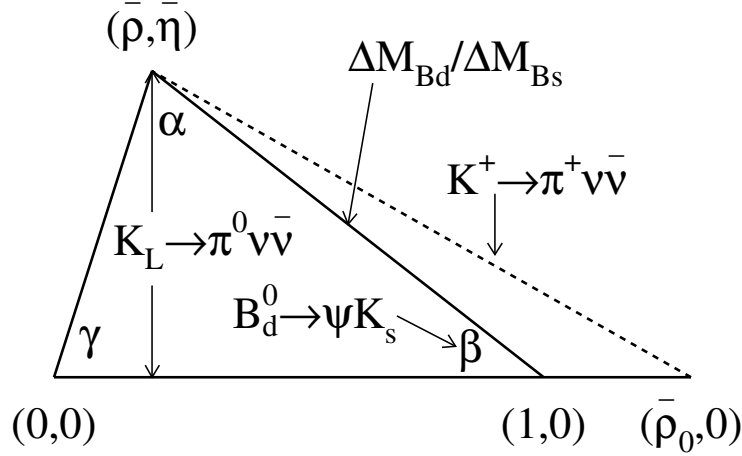


Fig. 2. Unitarity triangle determined by B and K decays. The parameters ρ and η can be determined in two ways: the angle β from the CP violating asymmetry in the decay $B_d^0 \rightarrow J/\psi K_s^0$, and from the length of the side from $\Delta M_{B_s}/\Delta M_{B_d}$ in $B - \bar{B}$ mixing; the height of the triangle from $\mathcal{B}(K_L^0 \rightarrow \pi^0 \nu \bar{\nu})$ and the radius of a circle centered at $(\bar{\rho}_0, 0)$ from $\mathcal{B}(K^+ \rightarrow \pi^+ \nu \bar{\nu})$.

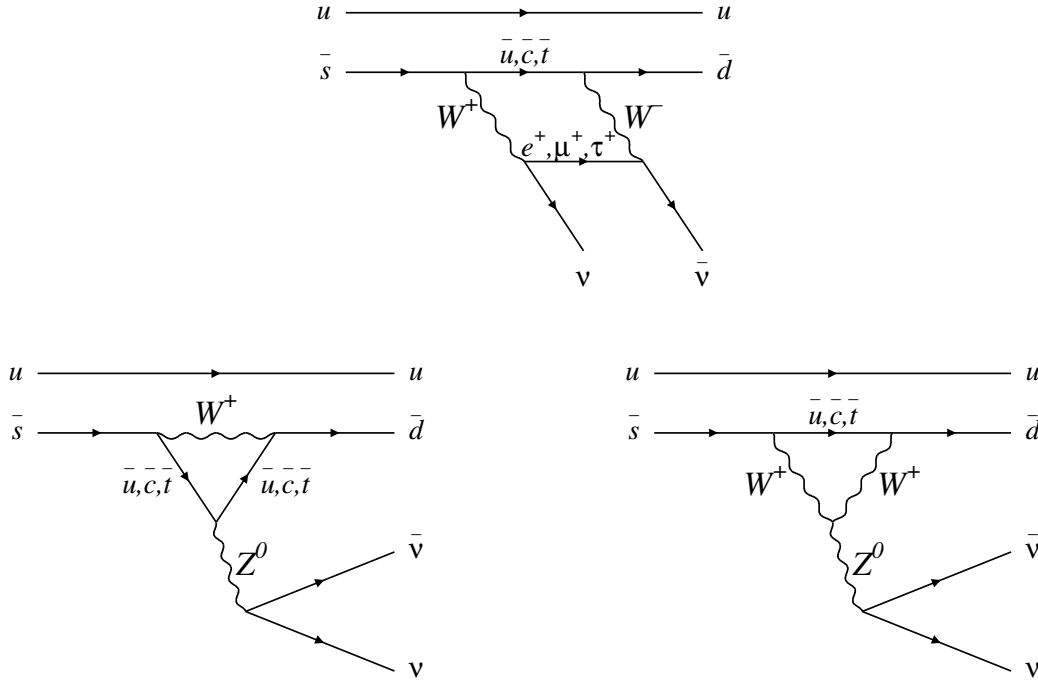


Fig. 3. Second-order weak processes that contribute to the $K^+ \rightarrow \pi^+ \nu \bar{\nu}$ branching ratio: the "Box" diagram (upper) and two "Z-penguin" diagrams (bottom).

Although the decay $K^+ \rightarrow \pi^+ \nu \bar{\nu}$ is a flavor changing neutral current (FCNC) process prohibited at tree level in the SM, it is allowed at the one-loop level. In leading order, it is described by a "Box" diagram and two "Z-penguin" diagrams, as shown in Figure 3. The weak amplitude for this process is represented as

$$\mathcal{M} \sim \sum_{i=u,c,t} V_{is}^* V_{id} \frac{\gamma^\mu q_\mu + m_i}{q^2 - m_i^2}, \quad (3)$$

where the V_{ij} 's are the CKM matrix elements, the γ^μ 's are the Dirac matrices, the q_μ is the momentum transfer, and the m_i 's are quark masses. \mathcal{M} vanishes if all of the quark masses, m_i , are equal, because of the unitarity of the CKM matrix. However, the breaking of flavor symmetry, which results in the variation of quark masses, allows this decay to proceed at a very small rate. The very large mass of the top quark makes its contribution to the $K^+ \rightarrow \pi^+ \nu \bar{\nu}$ branching ratio the largest in spite of the small coupling of top to down quarks (V_{td}) in the CKM matrix.

Following Ref.[8], the branching ratio for $K^+ \rightarrow \pi^+ \nu \bar{\nu}$ is calculated as follows. The effective Hamiltonian can be written in the SM as

$$\mathcal{H}_{eff}^{SM} = \frac{G_F}{\sqrt{2}} \frac{\alpha}{2\pi \sin^2 \Theta_W} \sum_{l=e,\mu,\tau} (V_{cs}^* V_{cd} X_{NL}^l + V_{ts}^* V_{td} X(x_t)) (\bar{s}d)_{V-A} (\bar{\nu}_l \nu_l)_{V-A}, \quad (4)$$

in next-to-leading order (NLO)

$$X(x_t) \equiv X_0(x_t) + \frac{\alpha_s(m_t)}{4\pi} X_1(x_t) \approx \eta_X \cdot X_0(x_t) \quad (5)$$

and

$$X_0(x_t) \equiv C_0(x_t) - 4B_0(x_t), \quad \eta_X = 0.995. \quad (6)$$

$B_0(x_j)$ and $C_0(x_j)$ in (6) are functions of $x_j \equiv m_j^2/M_W^2$, and were derived for the first time by Inami and Lim in 1981[9]. The coefficient X_{NL}^l and the function $X(x_t)$ are the charm and top quark contributions, including QCD corrections at NLO[10–12].

With the top quark mass in the minimal subtraction (\overline{MS}) scheme $m_t = (168.1 \pm 4.1)$ GeV[8],

$$X(x_t) = 1.529 \pm 0.042 \quad (7)$$

is obtained.

The perturbative charm contribution gives the largest theoretical uncertainty and can be described in terms of the parameter

$$P_c(X) \equiv \frac{1}{\lambda^4} \left[\frac{2}{3} X_{\text{NL}}^e + \frac{1}{3} X_{\text{NL}}^\tau \right] = 0.39 \pm 0.07, \quad (8)$$

where $\lambda = \sin \theta_c$, and the error is obtained by varying the charm mass, m_c , the scale factor, $\mu_c = \mathcal{O}(m_c)$ and the coupling constant, $\alpha_s(M_Z^2)$, by reasonable amounts. One obtains

$$\mathcal{B}(K^+ \rightarrow \pi^+ \nu \bar{\nu}) = \kappa_+ \cdot \left[\left(\frac{\text{Im} \lambda_t}{\lambda^5} X(x_t) \right)^2 + \left(\frac{\text{Re} \lambda_c}{\lambda} P_c(X) + \frac{\text{Re} \lambda_t}{\lambda^5} X(x_t) \right)^2 \right], \quad (9)$$

where

$$\kappa_+ \equiv r_+ \frac{3\alpha^2 \mathcal{B}(K^+ \rightarrow \pi^0 e^+ \nu)}{2\pi^2 \sin^4 \Theta_W} \lambda^8 = (4.84 \pm 0.06) \times 10^{-11} \left[\frac{\lambda}{0.224} \right]^8 \quad (10)$$

and the λ_j 's ($\equiv V_{js}^* V_{jd}$) are from the CKM matrix elements. The r_+ ($= 0.901$) represents isospin breaking corrections in relating $K^+ \rightarrow \pi^+ \nu \bar{\nu}$ to the well-measured decay $K^+ \rightarrow \pi^0 e^+ \nu$ [13]. In obtaining the numerical value in (10), we used[14]

$$\sin^2 \Theta_W = 0.231, \quad \alpha = \frac{1}{127.9}, \quad \mathcal{B}(K^+ \rightarrow \pi^0 e^+ \nu) = (4.87 \pm 0.06) \times 10^{-2}. \quad (11)$$

Employing the improved Wolfenstein decomposition of the CKM matrix[15], expression (9) describes in the $\bar{\rho} - \bar{\eta}$ plane an ellipse with a small eccentricity, namely

$$(\sigma \bar{\eta})^2 + (\bar{\rho} - \bar{\rho}_0)^2 = \frac{\sigma \mathcal{B}(K^+ \rightarrow \pi^+ \nu \bar{\nu})}{\bar{\kappa}_+ |V_{cb}|^4 X^2(x_t)}, \quad (12)$$

where

$$\bar{\rho}_0 \equiv 1 + \frac{\lambda^4 P_c(X)}{|V_{cb}|^2 X(x_t)}, \quad \sigma \equiv \left(1 - \frac{\lambda^2}{2} \right)^{-2}, \quad \bar{\kappa}_+ \equiv \frac{\kappa_+}{\lambda^8} = (7.64 \pm 0.09) \times 10^{-6}. \quad (13)$$

Using (9) and varying m_t , $|V_{cb}|$, $P_c(X)$ and $|V_{td}|$, which is constrained by $|V_{ub}/V_{cb}|$ and the $B^0 - \bar{B}^0$ mixing in the $\bar{\rho} - \bar{\eta}$ plane, the branching ratio of $K^+ \rightarrow \pi^+ \nu \bar{\nu}$ is predicted to be

$$\mathcal{B}(K^+ \rightarrow \pi^+ \nu \bar{\nu}) = (0.78 \pm 0.12) \times 10^{-10} \quad (14)$$

within the SM. The values of the parameters are summarized in Table 1. It should be noted that, of the uncertainty of 15% in (14), the theoretical uncertainty is $\sim 7\%$ at present, mainly due to the charm quark contribution.

Theoretically a precise measurement of $\mathcal{B}(K^+ \rightarrow \pi^+ \nu \bar{\nu})$ is one of the cleanest ways to extract the $|V_{td}|$. This is due to the following factors:

- the long-distance contributions to the branching ratio are small[16] and under control, a recent calculation gives a contribution of $(+6 \pm 3)\%$ to the branching ratio[18];

$\lambda = V_{us} = 0.2240 \pm 0.0036$
$\bar{\rho} = 0.187 \pm 0.059$
$\bar{\eta} = 0.354 \pm 0.027$
$ V_{cb} = (41.5 \pm 0.8) \times 10^{-3}$
$ V_{ub}/V_{cb} = 0.092 \pm 0.014$
$ V_{td} = (8.24 \pm 0.54) \times 10^{-3}$
$A = V_{cb} /\lambda^2 = 0.827 \pm 0.016$
$\sin 2\beta = 0.732 \pm 0.049$
$m_t = 168.1 \pm 4.1 \text{ GeV}$
$X(x_t) = 1.529 \pm 0.042$
$P_c(X) = 0.389 \pm 0.073$
$\bar{\rho}_0 = 1 + \lambda^4 P_c(X)/ V_{cb} ^2 X(x_t) = 1 + P_c(X)/A^2 X(x_t) = 1.373 \pm 0.068$
$\xi = f_{B_s}\sqrt{B_s}/f_{B_d}\sqrt{B_d} = 1.24 \pm 0.08$

Table 1. Parameters that are used in the SM prediction of the $\mathcal{B}(K^+ \rightarrow \pi^+ \nu \bar{\nu})$.

- the uncertainty from the hadronic matrix element has been removed by using $\mathcal{B}(K^+ \rightarrow \pi^0 e^+ \nu)$; and
- a recent NNLO calculation[17] has reduced the remaining theoretical uncertainties to $\sim 5\%$, *i.e.* relatively small and reliably calculated as compared with the uncertainties present in other K and B decays.

The theoretical uncertainty will be reduced with better knowledge of QCD corrections to the charm contribution at the next-to-next-leading-order (NNLO) level. A precise measurement of $\Delta M_{B_d}/\Delta M_{B_s}$ in $B^0 - \bar{B}^0$ mixing would also reduce the uncertainty in the SM prediction, once $B_s^0 - \bar{B}_s^0$ mixing has been measured[19]. A precise measurement of the $K^+ \rightarrow \pi^+ \nu \bar{\nu}$ branching ratio therefore allows a stringent test of the SM to be performed and is also a probe for new physics.

1.2 History of $K^+ \rightarrow \pi^+ \nu \bar{\nu}$ Experiments

Searches for this process which began over 35 years ago all have used stopped- K^+ beams. It was believed at the time of the first of these that the branching ratio might be as high as a few $\times 10^{-5}$ [20]. It was recognized that even at this level, a poor signature process such as $K^+ \rightarrow \pi^+ \nu \bar{\nu}$ would need effective particle identification, precise kinematic measurement and the ability to veto extra charged and neutral tracks to discriminate it from common decay modes such as $K^+ \rightarrow \mu^+ \nu$ and $K^+ \rightarrow \pi^+ \pi^0$ (referred as $K_{\mu 2}$ and $K_{\pi 2}$). The earliest published result was from a heavy liquid bubble chamber experiment[21] at the Argonne Zero Gradient Synchrotron, in which a 90% CL upper limit $\mathcal{B}(K^+ \rightarrow \pi^+ \nu \bar{\nu}) < 10^{-4}$ was obtained. In this paper it was recognized that $K_{\pi 2}$ decay in flight and hadronic π^+ interaction in the detector were dangerous sources of potential background.

The final analysis of the Argonne experiment improved the limit to 5.7×10^{-5} [22], but before it appeared in print, a subsequent counter/spark-chamber experiment at the Berkeley Bevatron improved the limit to 1.4×10^{-6} [23]. However this experiment was sensitive to only the most energetic of π^+ , whereas the bubble chamber experiment covered a wide kinematic range. In addition to the background from common K^+ decay modes, this experiment considered possible background from K^+ charge exchange in the stopping target followed by $K_L \rightarrow \pi^+ e^- \nu$, and from beam π^+ which scatter into the detector. The Chicago-Berkeley group continued their program with a setup sensitive to π^+ in the kinetic energy range 60-105 MeV, *i.e.* below that of the potential background process $K_{\pi 2}$ rather than above it. This required reconfiguring their photon veto system so that it became nearly hermetic. Combining results from the two configurations, the branching ratio upper limit was improved slightly to 5.6×10^{-7} [24].

About a decade later, an experiment at the KEK Proton Synchrotron improved the limit to 1.4×10^{-7} [30]. This experiment also was sensitive only to the π^+ with momenta greater than that from $K_{\pi 2}$ (“ $pnn1$ ” region) and its setup resembled that of Ref.[23].

The BNL series of experiments was initiated in the early 1980’s. It was based on a large-acceptance solenoidal spectrometer with a hermetic photon veto situated at the end of a highly pure, very intense stopped- K^+ beam[31] from the Brookhaven Alternating Gradient Synchrotron (AGS). The first phase of E787 ran in 1988-91 and achieved a 90% CL upper limit on the branching ratio of 2.4×10^{-9} [32], using data from the $pnn1$ region. A separate limit of 1.7×10^{-8} [33] was extracted from the kinematic region in which the π^+ is softer than that of the π^+ from $K_{\pi 2}$ (“ $pnn2$ ” region). This program also completed the identification of backgrounds needed to reach the 10^{-10} level of sensitivity and developed methods to reliably measure them.

A major upgrade of both the beamline and the detector was undertaken between 1992 and 1994. The search for $K^+ \rightarrow \pi^+ \nu \bar{\nu}$ resumed in 1995 and continued through 1998. The limit on the branching ratio from the $pnn2$ region was improved by an order of magnitude to 2.2×10^{-9} at 90% CL but the major output of this series of runs was the observation of two clean $K^+ \rightarrow \pi^+ \nu \bar{\nu}$ events[35] in the $pnn1$ region and a measurement of the branching ratio $B(K^+ \rightarrow \pi^+ \nu \bar{\nu}) = (1.57^{+1.75}_{-0.82}) \times 10^{-10}$. The result from the first year’s run[34] (in which an event was observed), $B(K^+ \rightarrow \pi^+ \nu \bar{\nu}) = 4.2^{+9.7}_{-3.5} \times 10^{-10}$, was even higher with respect to the SM prediction of the time ($(0.82 \pm 0.32) \times 10^{-10}$ [10]) and it stimulated a 1999 proposal[36] to continue the program with an upgraded detector E949, using the entire proton flux of the AGS.

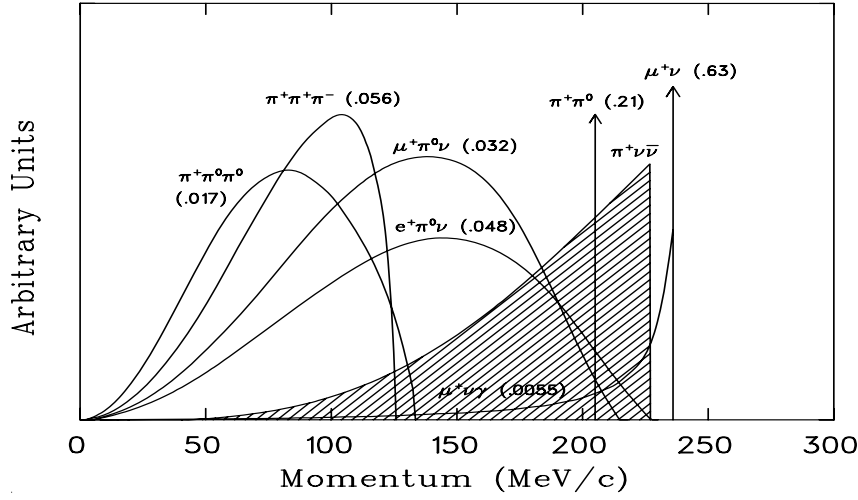


Fig. 4. Momentum spectra (in MeV/c) of charged particles from K^+ decays in the rest frame. The values in the parentheses represent the branching ratios for their decay modes. The hatched spectrum shows the π^+ momentum in the $K^+ \rightarrow \pi^+ \nu \bar{\nu}$ decay assuming the $V - A$ interaction.

2 Experimental Method

2.1 Overview

The advantage of a K^+ -stop experiment is that momenta of charged particles can be used as a distinguish feature in all the K^+ decay modes as shown in Figure 4. The experimental signature of the $K^+ \rightarrow \pi^+ \nu \bar{\nu}$ decay is a single π^+ track with π^+ momentum less than 227 MeV/c plus no other particle from a K^+ decay.

This experiment used the same technique as all the previous $K^+ \rightarrow \pi^+ \nu \bar{\nu}$ experiments: a low momentum K^+ beam stopped in the detector. Measurement of the $K^+ \rightarrow \pi^+ \nu \bar{\nu}$ decay involved an observation of the π^+ in the absence of other coincident activity. The π^+ was identified by its kinematic feature from the energy, momentum and range measurements, and by the observation of a $\pi^+ \rightarrow \mu^+ \rightarrow e^+$ decay sequence. Since the signal rate is expected to be about 10^{-10} level, to achieve this sensitivity the detector was designed to have a powerful π^+ identification to reject both the $K_{\mu 2}$ decay and the $K_{\mu 2 \gamma}$ decay (referred as $K_{\mu 2 \gamma}$), a 4- π solid angle photon veto plus full energy coverage to reject the $K_{\pi 2}$, and a beam K^+ identification to eliminate the beam backgrounds.

The E949 experiment (BNL-E949) was a successor to the E787 experiment (BNL-E787) that ran at the Alternating Gradient Synchrotron (AGS) at BNL from 1987–1999. The E787 detector has been described previously[31] as it existed during the period 1987–1991. The E787 detector was upgraded during 1992–1994, some of these upgrades have been described elsewhere[39,41,43,44], while others will be described here. The E949 detector (Figure 6) was upgraded over the period from 1999–2001[36,37]. Several improvements were made to the detector: additional and improved photon veto systems, improved tracking systems, improved trigger efficiency, and reduced the data acquisition (DAQ) dead time. E949 was designed to run at the same instantaneous rate as E787, and to achieve a factor of five improvement in average sensitivity by running with substantially more proton flux and a higher duty factor and reduced K^+ momentum for a higher stopping fraction. In practice the higher duty factor was not achieved in the engineering run in 2001 or the first physics run in 2002 due to a broken Siemens motor generator (MG) set at the AGS (the Siemens MG was removed from operation on 8/3/01 and the backup Westinghouse MG set was used during the rest of 2001 and 2002) and E949 ran at about twice the beam rate of E787. The experiment was proposed and approved by the U.S. Department of Energy's Office of High Energy

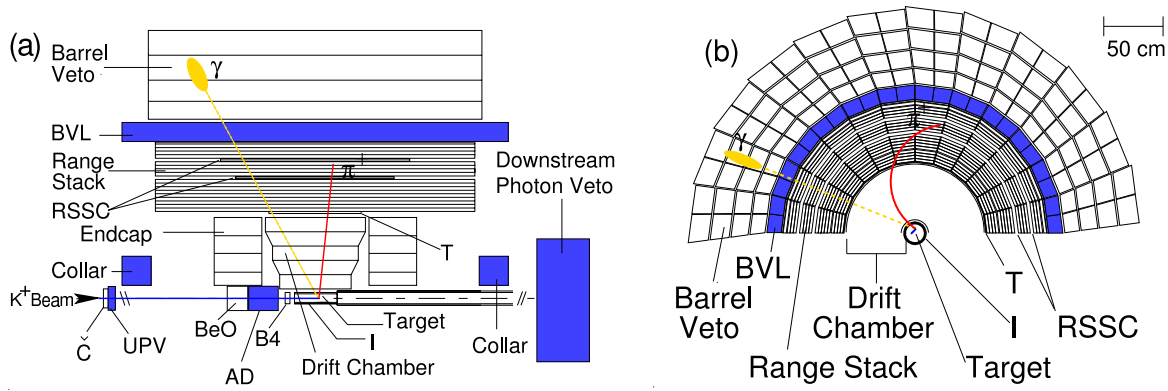


Fig. 5. Schematic side (left) and end (right) views of the upper half of the E949 detector. An incoming K^+ that goes through all the beam instruments and stops in the target undergoes the decay $K^+ \rightarrow \pi^+ \pi^0$. The outgoing π^+ and photon from $\pi^0 \rightarrow \gamma\gamma$ are also shown in the plots. The various detector elements and acronyms are described in detail in the text. A Cartesian coordinate system is used throughout this article, in which the $+z$ is along the incident beam direction and the $+y$ is in the vertical direction.

Physics to run for 60 weeks. After the first 12 weeks of running in 2002 no further funds were provided to complete the experiment. In this section, we will describe the detector and beam.

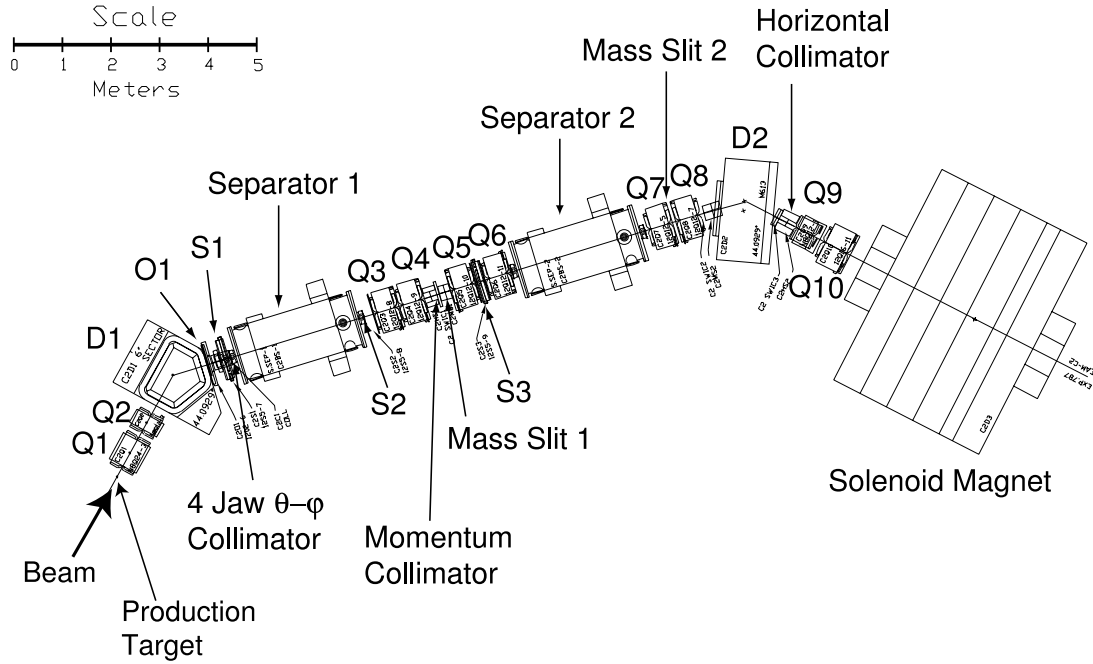


Fig. 6. Low-energy separated beam line III at BNL. The E949 solenoid magnet at the end of LESB III is also shown.

2.2 The Accelerator and K^+ Beam Line

The K^+ beam was produced by a high-intensity proton beam from the AGS at BNL: the entire AGS beam of 65×10^{12} protons (Tp) was delivered to the E949 K^+ production target (C-target). Protons were accelerated to a momentum of 21.5 GeV/c. Prior to 2001 the AGS typically ran at 24 GeV/c, but at this higher momentum the longest spill achievable with the Westinghouse MG set was 0.5 sec. Combined with the longer cycle time of the Westinghouse (3.2 sec between spills, as compared to 2.3 sec with the Siemens), the duty factor at 24 GeV/c was unacceptably low. By lowering the proton momentum to 21.5 GeV/c, the spill length was increased to a maximum of 2.2 sec, resulting in a duty factor of 2.2sec/5.4sec. At this lower proton momentum the production of 710 MeV/c K^+ s was reduced by 10%. The K^+ production target is made of 2/3 of an interaction length of platinum (6 cm along the beam direction), and is located on a water-cooled copper base. At the typical AGS running condition 65 Tp on the production target per 2.2 second spill at 21.5 GeV/c the maximum target temperature was measured to be $\sim 700^\circ\text{C}$.

The Low Energy Separated Beam[38] (LESB III), shown in Figure 6, collected and transported K^+ s emitted at 0° (along with 500 π^+ s and 500 protons at the target for every K^+), and is momentum-selected by dipole magnet D1 (see Figure 6). Two electro-magneto-static separators (Separators 1 and 2 in Figure 6) sweep π^+ s and protons out of the beam. The resulting beam is further selected by a second dipole magnet (D2 in Figure 6). LESB III contains a number of focusing quadrupole (Q1-10), sextupole (S1-3), and octupole (O1) magnets and collimating slits, and has a total length of 19.6 m from the production target to the E949 target with an angular acceptance of 12 msr and a momentum acceptance of 4.5% FWHM. K^+ s with a mean momentum of 710 MeV/c were transported to E949. During most of the 2002 running period the first separator voltage was lowered from the standard voltage of 600kV to $\sim 250\text{kV}$ due to high voltage discharges. This reduced operating voltage necessitated a retuning of the beam line to remove π^+ s with a consequent loss of K^+ s. Under these conditions a $K^+ : \pi^+$ ratio in the beam of 3:1 was achieved with a 40% loss in K^+ flux (typically E787 ran with 4:1). Proton contamination

was suppressed to a negligible level by the separators. At the typical AGS running condition of 65 Tp on the production target per spill, 1.3×10^7 K^+ 's were transported through the beam line.

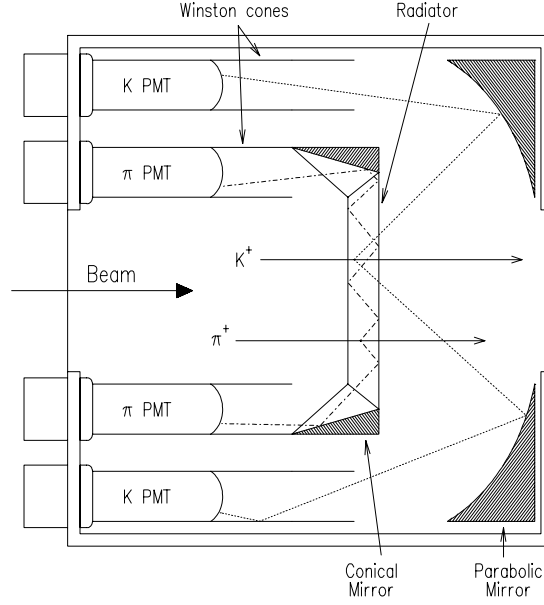


Fig. 7. Side view of the Čerenkov counter.

2.3 Beam Counters

The incoming K^+ beam traversed a large scintillation counter (B0), a Čerenkov counter, two beam wire proportional chambers, a passive BeO and active degrader (AD) and a beam hodoscope (B4) as depicted in Figure 5. The wire proportional chambers and B0 counter are not shown in Figure 5.

The B0 counter was located just downstream of the last quadrupole magnet (Q10) and counted all charged particles in the beam. The Čerenkov counter (see Figure 7) located just downstream of the B0 counter identified particles as K^+ s or π^+ s. The refractive index (n) of the 25 mm thick acrylic radiator is 1.49, providing a threshold for Čerenkov radiation of $\beta_C = 1/n = 0.671$ and a threshold for total internal reflection of $\beta_{ref} = \sqrt{1/(n^2 - 1)} = 0.905$. K^+ s and π^+ s with a momentum of 710 MeV/c have $\beta_{K^+} = 0.82$ and $\beta_{\pi^+} = 0.98$, respectively; the Čerenkov light from K^+ s (π^+ s) was transmitted (reflected) at the downstream surface of the Čerenkov radiator. The K^+ light exited the radiator and was reflected by a parabolic mirror to the outer ring of 14 EMI9954 photomultiplier (PMT) tubes (K^+ Čerenkov counter, C_K), while that from a π^+ was internally reflected within the radiator and directed to the inner ring of 14 PMT's (π^+ Čerenkov counter, C_π). The PMT signals were split, with 90% fed to time-to-digital converters (TDC's) via discriminators and 10% fed into a $\times 10$ amplifier and then to 500 MHz transient digitizers based on gallium-arsenide (GaAs) charge-coupled devices (CCD's)[39]. The pulse-height information in every 2 ns interval was recorded in CCD's to reproduce the time development of the pulses and to detect two particles close in time to each other. The number of photoelectrons in all PMT's provided additional particle identification. At the trigger level the number of Čerenkov discriminator channels firing (typically 5) was used to identify K^+ s and π^+ s. Offline analysis treated all PMT hits coincident with each other as a cluster. It is possible that a single K^+ beam event may contain one more time-coincidence particle (either a K^+ or a π^+). This extra particle can cause additional cluster when passing through the Čerenkov counter. A K^+ was therefore identified by requiring that the C_K had only one hit cluster. The average time of the hits in each cluster was compared to the K^+ decay time; any event with an extra particle coincident with the K^+ decay time was rejected, since an extra particle, not the decay of the initial K^+ , might be origin of the charged track that entered the fiducial region of the detector. Since two incoming particles close in time can fire the same PMT's, and these pileup signals

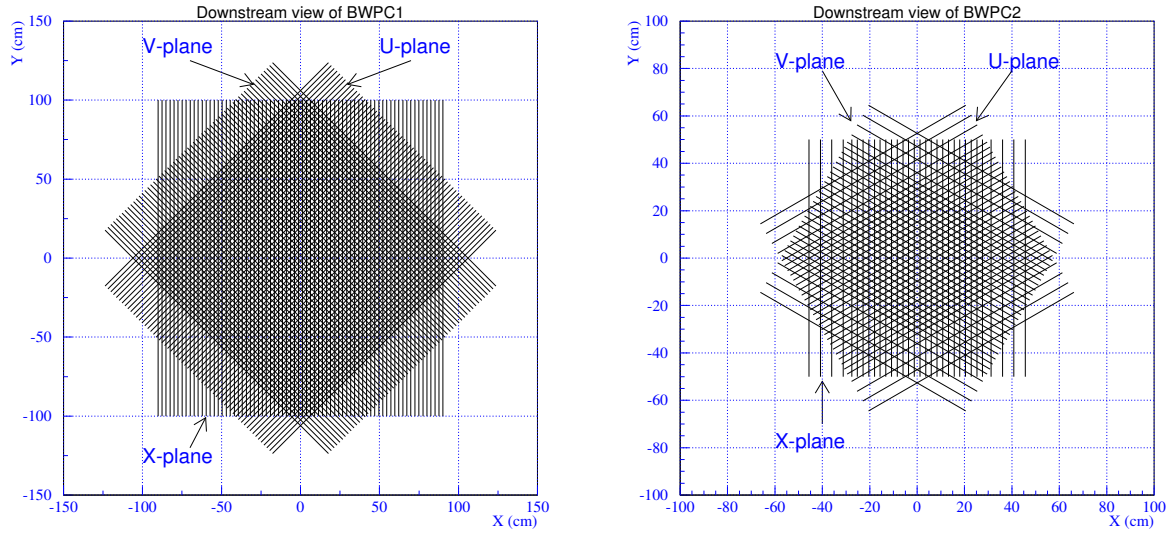


Fig. 8. Cross-sectional views of the beam wire proportional chambers (BWPC's): the first BWPC (left) and the second BWPC (right).

may not be identified by the TDC's. The pulse shapes recorded in the CCD's were therefore used to discriminate such pileup signals.

The two beam wire proportional chambers (BWPC's) were located downstream of the Čerenkov counter and UPV, and monitored the beam profile and identified multiple incoming particles. Cross-sectional views of the BWPC's are shown in Figure 8. The first chamber (BWPC1) contained three planes of sense wires: U, V and X. The direction of the sense wires was vertical (X-plane) and $\pm 45^\circ$ to the vertical (U- and V-planes). The sense wires were 0.012 mm diameter gold-plated tungsten. The X-, U- and V-planes had 72, 60 and 60 readout channels respectively, with 2.54 mm wire spacing. The spatial resolution was 1.5 mm and the active area was 178 mm (horizontal) by 50.8 mm (vertical). The cathode foils were 0.025-mm thick aluminized mylar coated with carbon. The anode-cathode distance was 3.175 mm, and the total thickness of BWPC1 was approximately 56 mm. The second chamber (BWPC2) was located 900 mm downstream of BWPC1 and contained three planes (U, V and X). The direction of the sense wires was vertical (X-plane) and $\pm 60^\circ$ to the vertical (U- and V-planes). Each plane had 24 readout channels with a 2.4-mm wire spacing in the central region (57.6 mm) and 8 channels with a 4.8-mm wire-spacing in the peripheral region (19.2 mm on each end). The cathode foils were 0.008-mm single-sided aluminized mylar coated with carbon. The anode-cathode distance was 1.5875 mm. Both chambers were filled with a mixture of CF₄ (80%) and Isobutane (20%).

Downstream of the BWPC's, a degrader slowed the K^+ s to come to rest in the center of the target. The upstream section of the degrader was inactive with 111.1 mm of beryllium oxide (BeO) and 4.76 mm of Lucite. The total thickness was tuned to stop K^+ s with a momentum of 710 MeV/c in the center of the target. BeO, with high density (3.0 g/cm^3) and low atomic number, minimized the multiple scattering. The downstream active degrader (AD) consisted of 40 layers of 2 mm thick scintillator disks (139 mm diameter) alternating with 2.2-mm thick copper disks (136 mm diameter). The AD was divided into 12 azimuthal segments, and the scintillation light in each segment was sent to a single Hamamatsu R1924 PMT through 14 Bicron BCF99-29-AA-MC wave length shifting (WLS) fibers. The PMT outputs were fed to TDC's and CCD's. The signals from 4 PMT's were multiplexed and fed to a single ADC. The AD identified the beam particles and detected activity coincident with K^+ decays.

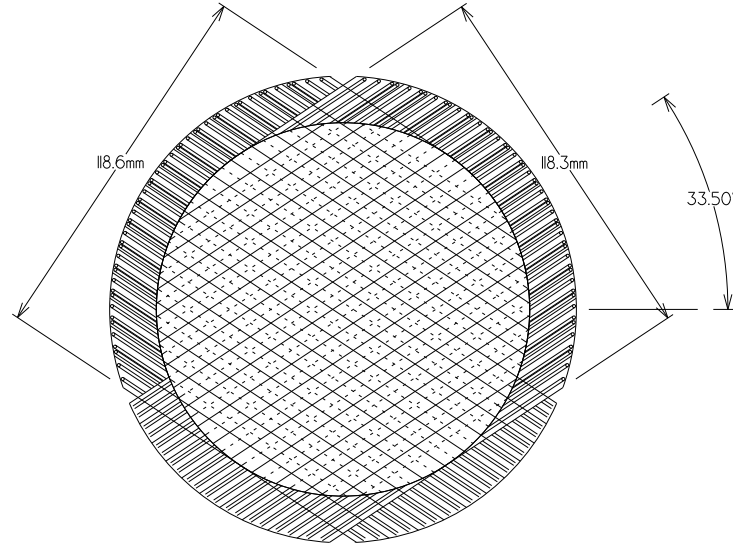


Fig. 9. End view of the B4 hodoscope. Patterns of scintillator fingers on the downstream and upstream surfaces are shown in solid and dashed lines separately.

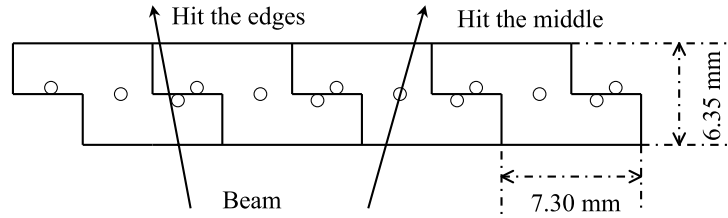


Fig. 10. Schematic cross section of the B4 hodoscope. Arrows indicate difference situations of beam particles passing through the B4 hodoscope. The approximate position of the three wavelength shifter fibers in each finger are indicated by the small circles.

Downstream of the degrader was a beam hodoscope (B4) that detected the position of the incoming particle, giving a 3-dimensional space-point to match to the target and identified the particle as a K^+ or π^+ by measuring its energy deposit. An end view of the B4 hodoscope is shown in Figure 9. The B4 hodoscope consisted of two planes, U and V, with a 119 mm diameter oriented at a 33.40° angle to the horizontal. Each plane had 16 scintillator fingers with a 7.2 mm pitch. The cross section of each finger had a 'Z-shape', as shown in Figure 10, with a 6.35-mm thick middle part and 3.175-mm thick edges. This shape reduced inactive regions and improved the spatial resolution. Three Bicron BCF99-29-AA-MC WLS fibers were embedded in each finger and fed to a single Hamamatsu H3165-10 PMT that was read out by TDC's, ADC's and CCD's. The pulse shape recorded with the CCD provided pileup information. The time development of the output signals were fit with both single- and double-pulse assumptions. If the fitted pulse was more likely to be a double pulse and the time of the second pulse was coincident with the K^+ decay time, the event was rejected. At the same position as the B4 hodoscope, but at larger radius was another scintillator counter, the ring veto (RV). The RV was designed to veto particles that passed through perimeter of the B4 hodoscope. The RV was composed of two 180° arcs of 3.27 mm thick scintillator with an inner diameter varying from 118.5 mm to 120 mm and an outer diameter of 145.5 mm. The two RV elements were readout to H3165-10 PMT's and the signals were split three ways to ADC's, TDC's and CCD's.

Approximately 27% of the incident K^+ s penetrated far enough into the target to deposit 20 MeV or

more energy and satisfy the online trigger criteria. The remaining K^+ s either underwent decay-in-flight, nuclear interaction in the degrader or scattered in the material of the beam instrumentation and did not reach the target. Typically 3.5×10^6 K^+ s entered the target per beam spill.

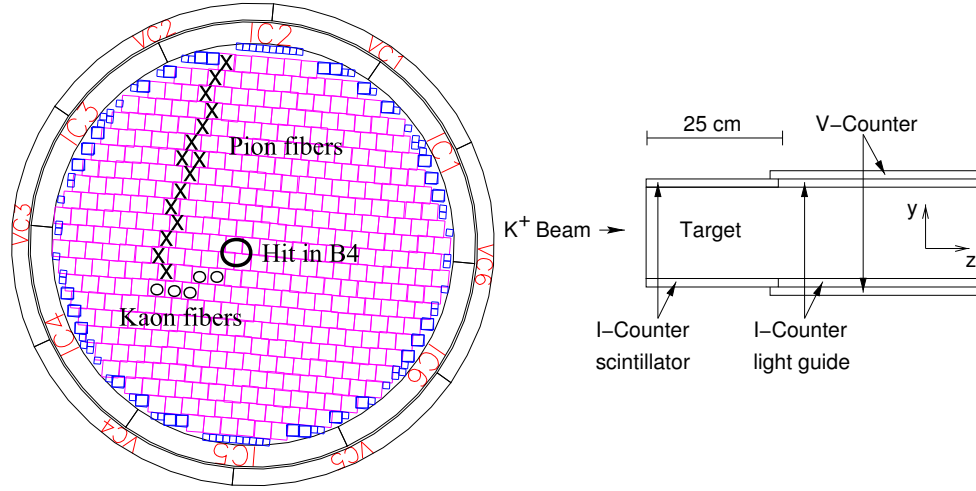


Fig. 11. End (left) and side (right) views of the target. Two layers of 6 plastic scintillators, I-Counter (IC) and V-Counter (VC), surround the target. The smaller squares close to the IC are the edge fibers. The K^+ cluster, the π^+ cluster and the beam entrance point indicated by the B4 are also shown in the end-view of the target.

2.4 Target

The K^+ s, slowed down by the degraders, entered the scintillating fiber target located in the center of the spectrometer. The majority of entering K^+ s lost energy by ionization, came to rest and decayed in the target. The target consisted of 413 5-mm square and 3.1-m long plastic scintillating fibers that were bundled to form a 12-cm diameter cylinder. A number of 1-mm and 2-mm square scintillating fibers (called “edge fibers”) filled the gaps near the outer edge of the target, in order to have a uniform thickness of the target material. End and side views of the target are shown in Figure 11. Each of the 5-mm fibers was connected to a PMT, whereas the edge fibers were grouped into 12 and each group of the edge fibers was connected to a single PMT. The PMTs were read out by ADCs, TDCs and CCDs. The low velocity K^+ s typically lost 20-30 MeV in each fiber, while π^+ s from K^+ decays lost about 1 MeV per fiber, since they traveled nearly perpendicularly and lost energy as minimum ionizing particles (MIPs).

The fiducial region of the target was defined by two layers of 6 plastic-scintillating counters that surrounded the target (see Figure 11). The inner scintillators, called I-Counter (IC), tagged charged decay products before they entered the drift chamber, and provide a trigger signal to the data acquisition system. The IC was 6.4-mm thick at an inner radius of 6.0 cm, and extended 24 cm downstream from the upstream face of the target. Each scintillator was instrumented with a PMT, and was read out by an ADC, a TDC and a 500 MHz transient digitizer (TD) based on a flash ADC[40]. The outer scintillators, called the V-Counter (VC), overlapped the downstream edge of the IC by 6 mm, and served to detect particles that decayed downstream of the fiducial region of the target. The VC was 5-mm thick and 1.96-m long, and was staggered azimuthally with respect to the IC as indicated in Figures 11. Each scintillator was instrumented with a PMT, which was read out by an ADC and a TDC.

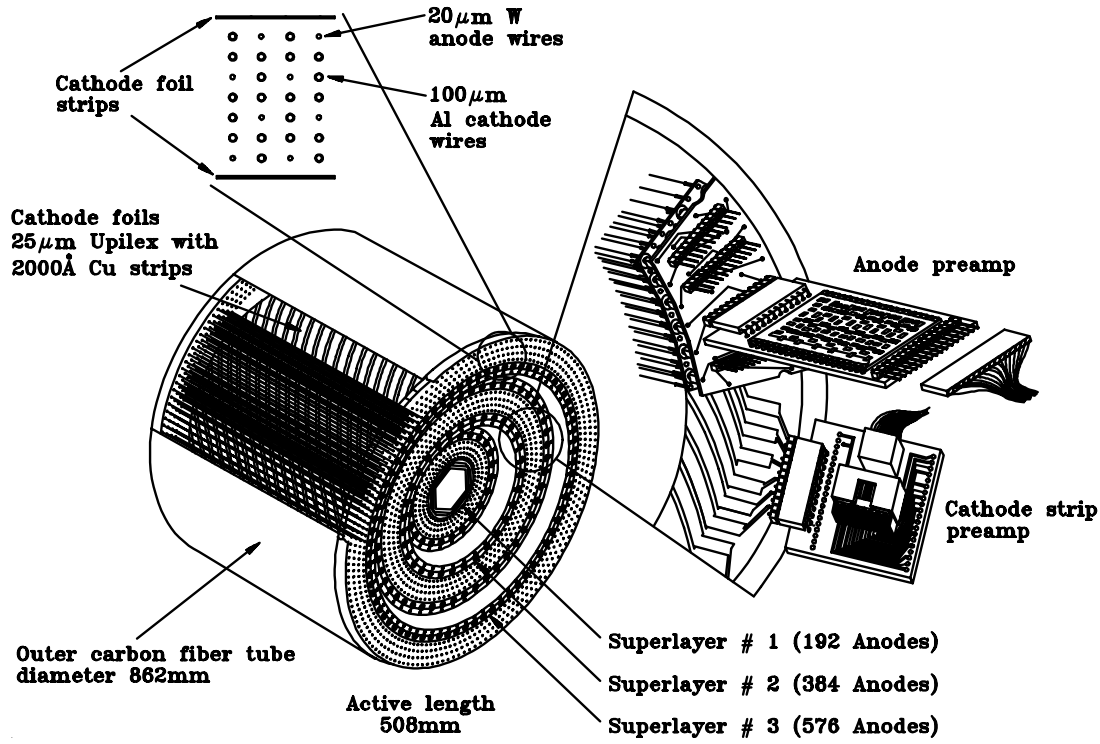


Fig. 12. Schematic view of the drift chamber.

2.5 Tracking Chamber

The tracking chamber consisted of a drift chamber, which is also called "Ultra Thin Chamber" (UTC)[41] and was located just outside of the IC. The whole spectrometer was in a 1 Tesla solenoidal magnetic field. Positively charged particles were bent clockwise in the view from downstream. The primary functions of the UTC were to measure the momenta of charged particles and to provide matching of the charged particle trajectory (track) between the target and the Range Stack (RS) as well.

The UTC had a maximum length of 50.8 cm, and an inner and an outer radii of 7.85 cm and 43.31 cm, respectively. The 12 layers of drift cells were grouped into 3 super layers. The inner, middle and outer super layers all had 4 sub layers each, consisting of 48, 96 cells, 144 cells, respectively as shown in Figure 12. The three super layers have different active lengths (38.8 cm for the inner, 44.8 cm for the middle and 50.8 cm for the outer). Each cell was composed of 9 wires strung axially. A single anode wire, made of gold-coated tungsten with 20-μm diameter, was surrounded in a square by 8 cathode wires made of gold-coated aluminum with 100-μm diameter. Adjacent cells shared the cathode wires at the boundaries. The cells in each layer were staggered by one-half cell with respect to the neighboring layers in order to resolve the left-right ambiguity in track fitting. The super layers were filled with a mixture of argon (49.8%), ethane (49.8%) and ethanol (0.4%) gases. The cathode wires were all grounded, while the anode wires were maintained at 2 kV to achieve a gain of 8×10^4 and a 5 cm/μs drift velocity. Each anode wire was instrumented with an ADC and a TDC. The drift time to the anode wires was used to determine the (x, y) positions for the charged track.

The inner and outer radii of each super layer had helical arrays of cathode strips with a pitch angle of $\sim 45^\circ$. There was a 1 mm gap between the 7 mm wide strips that were composed of 120 nm thick copper with a 30 nm thick nickel coating and were mounted on 25 μm thick Kapton foil. The cathode foils had 48, 72, 108, 144, 180, and 216 strips from the inner to the outer layers, respectively. Each cathode strip was instrumented with an ADC and a TDC. The z position of a charged track was determined by the

charge-weighted mean of the cluster of hit strips with the corresponding anode wire hits. The position resolution was measured to be about 1 mm.

There were 2 inactive regions filled with nitrogen gas between the 3 super layers. Differential pressures in the 5 gas volumes supported the cathode foils (excluding the innermost and outermost foils, which were held in place by support tubes). The total mass in the active region of UTC (excluding the inner and outer support tubes and innermost and outermost foils) amounted to 2×10^{-3} radiation lengths.

The magnetic field in the UTC was continuously read out from two hall probes installed inside the detector. They were both mounted on the inner downstream face of the magnet end plate at a radial position close to the barrel photon veto system. The power supply to the magnet was regulated through a shunt in the output current path and was usually subject to temperature and aging effects. It had been noticed that the hall probes readout drifted downward slowly over the years. There was a 0.4% variation observed throughout the E949 data taking period. This variation was also confirmed by the shift of both $K_{\pi 2}$ and $K_{\mu 2}$ momentum peaks when assuming a constant magnetic field. The measurement of magnetic field was taken into account in the assignment of the charged particle momentum.

The UTC geometrical alignment was done for both the position of anode wires and cathode foil layers. The charged pions from identified $K_{\pi 2}$ decays were used to determine the $x - y$ position each anode wire. In this sample, the charged track was required to be perpendicular to the z direction and to have a momentum consistent with the $K_{\pi 2}$ momentum peak within 5 MeV/c. The residual for each wire measurement was then translated into corrections to the wire position. Cosmic ray trigger data with the magnetic field off was used to do the $r - z$ alignment of the cathode foil layer.

2.6 Range Stack

The Range Stack (RS) was located just outside the UTC at an inner radius of 45.08 cm and an outer radius of 84.67 cm. The RS consisted of both the scintillator counters and the embedded straw chambers, providing energy and range measurement of the charged particles, information on the $\pi^+ \rightarrow \mu^+ \rightarrow e^+$ decay sequence and measurement of the photon activity as well.

2.6.1 Scintillator Counters

The RS scintillator counters consisted of 19 layers of plastic scintillators, azimuthally segmented into 24 sectors as shown in Figure 5. Four contiguous sectors (i.e., sectors 1-4, 5-8, etc.) were grouped into “hextants” for read out and triggering purposes. The scintillators of layers 2-18 had a thickness of 1.905 cm and a length of 182 cm. The scintillators of layer 19 had a thickness of 1 cm; this layer was mainly used to veto charged particles with range longer than that expected for the π^+ from $K^+ \rightarrow \pi^+ \nu \bar{\nu}$. The scintillation light in the layer 2-19 counters was led by Lucite light guides to PMTs at both the upstream and downstream ends. The innermost counters were the trigger-counters (T-counters) and had a thickness of 6.35 mm and a length of 52 cm. The T-counters are thinner than layers 2-19 to suppress triggers due to photon conversions. Seventeen 1 mm diameter WLS fibers (Bicron multi-clad BCF-92) with a pitch of 6.9 mm were embedded in each scintillator and were grouped to illuminate a single PMT for each end. The T-Counters also defined the fiducial region as 2π sr solid angle, nearly the same as the solid-angle acceptance of UTC.

The signal from each PMT of the RS scintillators was passively split 1:2:2 for ADC:TDC:TD read out. Each PMT was read by an ADC and a TDC. The ADCs (LeCroy 4300) recorded charge in a $(-20, +85)$ ns interval about the trigger time, and the TDCs (LeCroy 3377) recorded up to 16 hits in a $(-0.5, +10.0)\mu\text{s}$ interval about the trigger time. The large time interval after the trigger for the TDCs allowed detection of the $\mu^+ \rightarrow e^+$ decay. The time of a hit in the RS counters was obtained from the average of the upstream and downstream TDC times, and the z position of the hit was obtained from the time difference. Signals from 4 PMTs at the same end, same hextant and same layer were multiplexed and read out by a single TD[40]. The TDs recorded the charge in 2 ns intervals (500 MHz sampling) in a $(-0.5, +2.0)\mu\text{s}$ interval about the trigger time with a resolution of 8 bits (0-255 counts). The 500 MHz sampling provided sufficient pulse shape information to separate the pulses from different energy deposits as close as 5 ns apart, and enabled the detection of the $\pi^+ \rightarrow \mu^+$ decay as described in Section 3.6.3. The time window of the TDs was narrower than that of the TDCs in order to reduce the data size. TD signals were demultiplexed offline using TDC information.

The π^+ s from $K^+ \rightarrow \pi^+ \nu \bar{\nu}$ decay had a maximum momentum of 227 MeV/c and a maximum range in plastic scintillator of ~ 40 cm, which was shorter than 45 cm for the total penetration of the RS and target. All of the π^+ s, bent in a 1 Tesla magnetic field, lost their entire kinetic energy and came to rest in the RS. In comparison, the μ^+ s from the $K_{\mu 2}$ decay ($Br(K^+ \rightarrow \mu^+ \nu_\mu) = 63.4\%$ [7]) at rest have a momentum of 236 MeV/c and a range of 54.3 cm in plastic scintillator, generally penetrated the entire RS. Lower momentum μ^+ s from the $K_{\mu 2\gamma}$ and $K_{\mu 3}$ decays ($Br(K^+ \rightarrow \mu^+ \nu_\mu \gamma) = 0.55\%$ and $Br(K^+ \rightarrow \mu^+ \pi^0 \nu_\mu) = 3.27\%$ [7]) as well as μ^+ s from π^+ decay in flight could come to rest in the RS.

2.6.2 Range Stack Straw Chambers

Two range stack straw chambers (RSSCs) were located after layers 10 and 14 in each RS sector. The inner (outer) RSSC consisted of two staggered layers of 24 (28) straws per sector with a length 97.8 (113.0) cm. The average mass density of an RSSC super layer was 0.054g/cm^2 . Each straw tube was 3.4 mm in radius and had a 38- μm thick Kapton-coated Cu/Ni cathode and 50- μm diameter gold-coated tungsten anode wire. A detailed drawing is given in Figure 13. The straw tubes operated with 67% argon and 33% isobutane mixture in a self-quenching streamer mode at 3450V. The x -axis of a chamber is defined to be along the width of the chamber. There were a total of 48 chambers, with 2496 straws

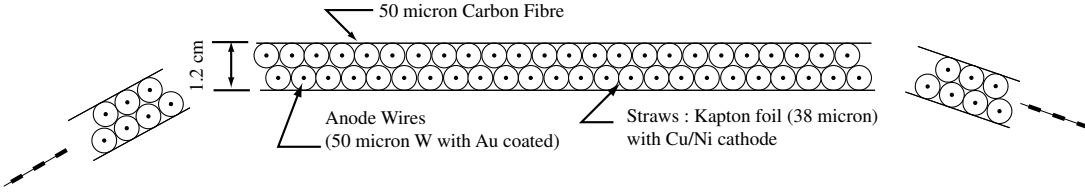


Fig. 13. Schematic end view of the inner RSSC. The tubes run through the beam direction.

installed in the E949 experiment.

Two straws in the same sub-layer were connected in pairs on the upstream end by using a dedicated “jumper card”. Connected straws were separated by 12(14) straws, for the inner (outer) chambers, reducing the electronic channel count from 2496 straws to 1248 pairs. The chambers were read out from only the downstream end because of the severe space constraints.

The position of the hit straws provides the $x - y$ position information, while the end-to-end time difference provides the longitudinal z measurement. Initially, the z resolution was not so good as designed due to the pulse-height dependent time-walk effect. New electronics using an amplifier and two discriminators for each channel were installed. The low threshold discriminator provided the timing and the high threshold discriminator was set above the noise level. A z resolution of 1.5 cm (RMS) was achieved in E949 compared 3 cm observed in E787.

2.7 Photon Veto Counters

The detection of any activities coincident with the charged track is crucial for suppressing the backgrounds for $K^+ \rightarrow \pi^+ \nu \bar{\nu}$. Photons from the $K_{\pi 2}$ and the other radiative decays were detected by the hermetic photon detectors as already shown in Figure 5. The photon detectors, surrounding the K^+ decay vertex in a 4π solid angle, were located in the barrel, upstream and downstream end caps, and near the beam line. The photon veto was performed by the Barrel Veto (BV), the Barrel Veto Liner (BVL), the upstream and downstream End Caps (ECs), the Upstream Photon Veto (UPV), the upstream and downstream Collar detectors (CO), the downstream Microcollar detector (μ CO), the Downstream Photon Veto (DPV), the Ring Veto (RV), as well as the AD, the target and the RS photon vetoes. The DPV was part of the E949 detector upgrade but was only used in the $pnn2$ analysis, where a more stringent photon is needed.

The 1.9-meter-long, 14.3-r.l. BV covering $2/3$ of the 4π sr solid angle was located in the outermost barrel region with an inner radius of 94.5 cm and an outer radius of 145.3 cm. The BV was divided into 48 azimuthal sectors. Each sector consisted of four radial segments, in which there were 16 (inner most), 18, 20, 21 (outer most) layers of 1-mm thick lead and 5-mm thick plastic scintillator. The photon energy left in the scintillators accounted for 30% of the total energy deposit in the BV. The azimuthal boundaries of each sector were tilted so that no crack was left along the radial direction for the photons from the decay vertex. Each end of every module was read out by a PMT and the signals were recorded by an ADC and a TDC. The time resolution of individual BV counter, which was measured to be 1.2 ns, was limited by the sampling time of the TDCs.

The BVL located between the RS and the BV, replaced with the outermost layers 20 and 21 of the RS in E787. Each BVL counter was 10 cm wide and 220 cm long. There were 48 azimuthal sectors in total. Each sector consisted of 12 layers of 1-mm thick lead and 5-mm thick plastic scintillators, all of which gave a total of 2.29 radiation lengths in thickness. Each end of a BVL module was read out by a PMT and the signals were recorded by an ADC and a TDC. Adjacent sectors in each end were grouped and read out by the TDs. The timing resolution of individual BVL counter was observed to be 0.7 ns, which was also limited by the TDC sampling time. A comparison of radiation length with and without the BVL is shown in Figure 14. A factor of two photon veto rejection gain was expected with this radiation length increase.

The EC[43] was located in the 1 Tesla magnetic field and had roughly one-third of the 4π sr photon coverage. The upstream EC detector consisted of 75 undoped Cesium Iodide (CsI) crystals segmented to the four rings (13, 14, 21 and 27 crystals from the inner to outer rings, respectively), and the downstream EC detector consisted of 68 crystals in the four rings (11, 13, 19 and 25 from inner to outer rings, respectively). A total of 143 crystals with a pentagonal cross-section were used in the EC as shown in Figure 15. Each crystal measured in 25 cm long (13.5 radiation lengths), and the whole EC detector was designed to minimize photon escape through its radial cracks. Fine-mesh PMTs[44], which maintained high gains in strong magnetic fields, were attached directly to the crystals to achieve efficient light collection (see Figure 15). Only the fast component of the CsI light output with a decay time of ~ 0.5 ns at a wavelength of 305 nm was selected by ultraviolet (UV) transmitting optical filters. The slow component was completely blocked. Since the EC was exposed in a high counting-rate environment near the beam line, beam particles could cause many irrelevant hits so that the photons from a $K_{\pi 2}$ decay might be masked if this accidental hit arrived earlier (see Figure 16). The PMT signals were read out by ADCs, TDCs, and CCDs. The pulses recorded in the CCDs were analyzed by a pulse-finding algorithm, in order to separate two pulses close in time and reduce the possibility of accidental vetoes and the inefficiencies of photon detection.

The UPV was mounted to the downstream face of the Čerenkov counter and was 3.1 radiation length thick, with an outer dimension of 284 mm \times 284 mm and an inner hole for the beam of 175 mm (hor-

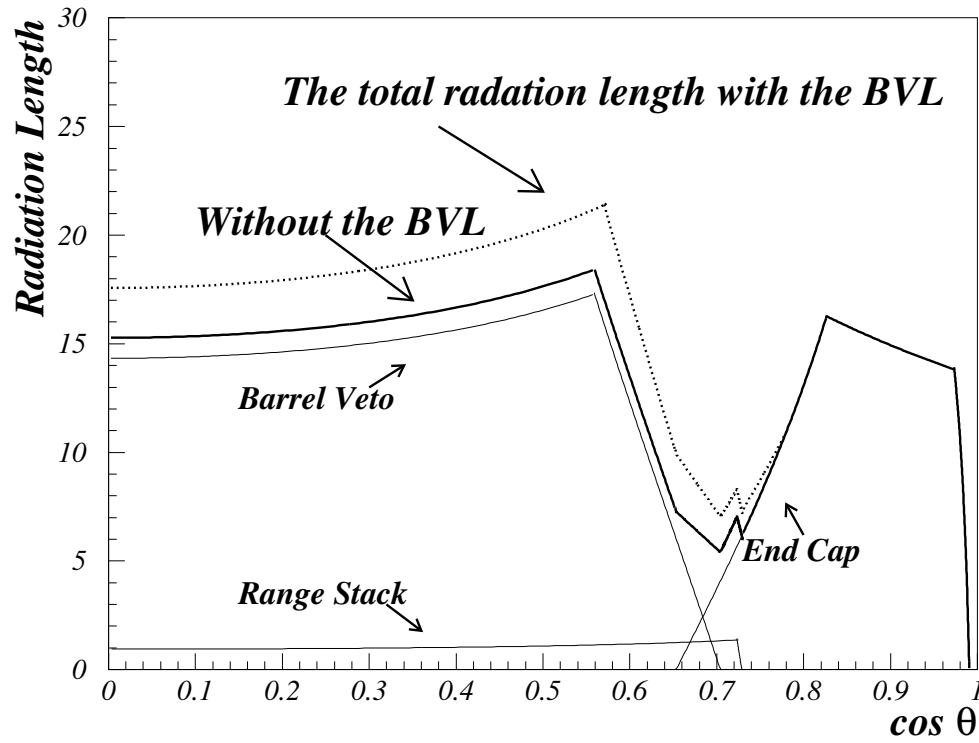


Fig. 14. Radiation length with (solid curve) and without (dotted curve) the BVL as a function of the cosine of polar angle.

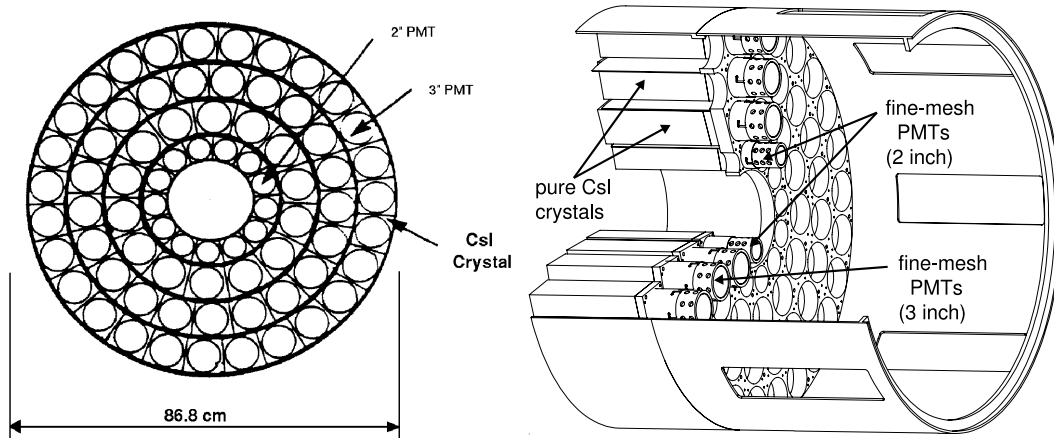


Fig. 15. End view (left) and back view (right) of the End Cap.

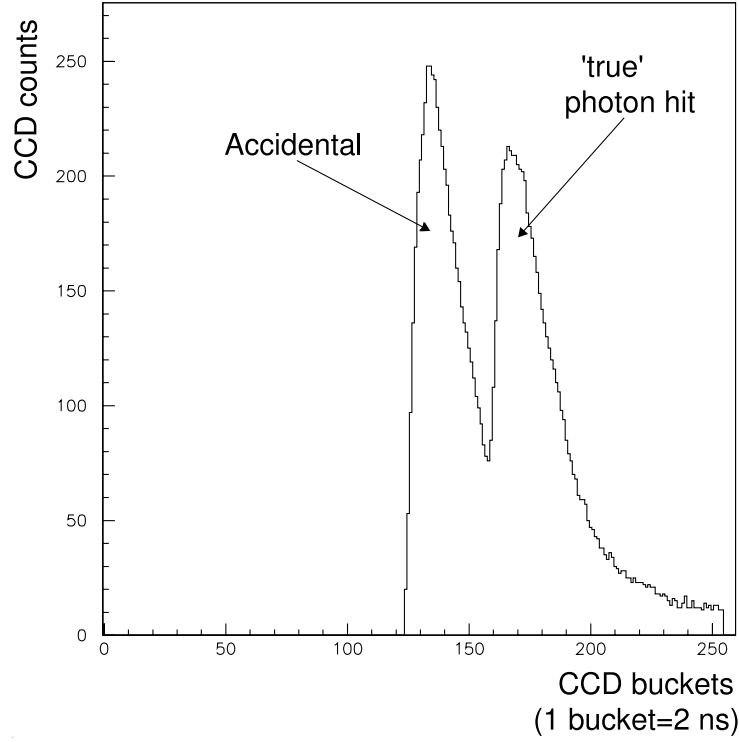


Fig. 16. Pulses recorded in the End Cap CCD. The first pulse is due to an early accidental hit and the second pulse is due to the photon from the $K_{\pi 2}$ decays.

horizontal) \times 40 mm (vertical). The 12 layers of 2 mm BC404 plastic scintillator were each read out by 21 WLS fibers to one of two Hamamatsu R1924 PMT's. The UPV signals were split three ways to Analog-to-Digital Converters (ADC's), TDC's and CCD's.

The CO detectors were placed just behind the UPV and the downstream EC. Both the upstream CO and the downstream CO consisted of 24 2-mm thick lead sheet absorbers and alternatively stacked 25 layers of 5-mm thick scintillator plates of BC404(Bicron), providing about 9 radiation lengths to the beam direction. The CO was used to detect photons emitted with a small dip angle ($0.970 < \cos\theta < 0.995$) in both upstream and downstream regions. The downstream side of the CO was also supplemented by a smaller counter called the μ MC.

2.8 Trigger

Typically 3.5×10^6 K^+ s entered the E949 target every spill. The trigger selected $K^+ \rightarrow \pi^+ \nu \bar{\nu}$ events from the large number of K^+ decays and scattered beam particles with requirements on the range of the π^+ track, the presence of a $\pi^+ \rightarrow \mu^+ \nu_\mu$ decay, the absence of other activity at the time of the π^+ and the presence of a K^+ at an appropriately earlier time.

The trigger was composed of two stages: a fast Level-0 trigger with a decision time of ~ 100 ns and a slower Level-1.n trigger with a decision time of 10-100 μ s. The Level-0 trigger was based on scintillator signals from the beam, target, range stack and photon veto systems, processed with a combination of NIM logic and custom-built boards. The Level-1.n trigger was composed of two components running in parallel, Level-1.1 and -1.2 triggers, that involve partial processing of TD and ADC data, and operated on the lower rate events that pass the Level-0 trigger.

The trigger was constructed in Fastbus and contained the following modules: **Need to give the names of the modules** The trigger was upgraded for E949 with the addition of a new Level-0 trigger board and meantimers for the photon veto signals[45].

E949 collected data with triggers for $K^+ \rightarrow \pi^+ \nu \bar{\nu}$ signal, and for other physics studies and calibrations. The latter were prescaled and used for the purpose of detector calibration and monitoring and measurement of acceptance. In this paper, the triggers for calibration and other physics are called the “monitor” samples.

2.8.1 General Trigger Conditions

The E949 trigger consisted of two-stage hardware systems. The first stage, called “Level-0”, performed event selection based on *AND/OR* logic with discriminated signals from each detector. The next stage, called “Level-1”, involved two functions of more complexed hardware processing named “Level-1.1” and “Level-1.2”

A block diagram of the Level-0 trigger system is shown in Figure 17. The Level-0 trigger is a demand for a kaon in the beam followed by a single charged track into the RS. A K^+ was identified by a coincidence of hits from the Čerenkov counter, energy-loss counter and target. A charged track was required at this level to have a coincidence of the hits from the IC’s and the first layer (T-counter) and second layer in the same RS sector. The Level-0 trigger made a decision within ~ 38 ns based on the combination of logic signals (the actual combination varies according to the physics mode), introducing a minimum of 40 ns of dead time. When an event passed the Level-0 trigger, the dead time was extended to 100 ns to allow further processing. In total, the Level-0 trigger contributed 2.5% to the dead time at typical operating conditions. Following the Level-0, the Level-1.1 trigger was based on information from the TD system for the RS counter in which the charged track was determined to have stopped. Stopped π^+ s were preferentially selected (over μ^+ s) by looking for the $\pi \rightarrow \mu$ decay by comparing the pulse height to the pulse area (for early decays) or by looking for a second detached pulse. This was done by a custom-built ASIC which had access to the TD memories. The ASIC could also reduce the TD data size for readout by discarding the waveform samples outside the “prompt” time window, keeping instead a calculation of the pulse area and leading-edge time. The prompt window typically extended from 0.5 (2) μ s before (after) the π^+ track. For typical running conditions, Level-1.1 provided a decision in about 10 to 20 μ s with a rejection of ~ 11 and a signal acceptance $\sim 85\%$, which was measured using Beam π^+ monitor sample after the full offline cuts applied.

The Level-1.2 had two components. One of them, called “Level-1.1 afterburner”, is unrelated to the photon veto. The condition rejected events with an accidental hit near the stopping counter. This hit may defeat the Level-1.1 with an fake double pulse. The other component, called “HEX afterburner”, was used for the photon veto, and rejecting events with hits in both of the two adjacent hexants while the $T \cdot 2$ counter and the stopping counter were found in the same hexant. This usually indicates that a single hexant fully contained the trajectory and hits and, those observed in the other hexant came from another

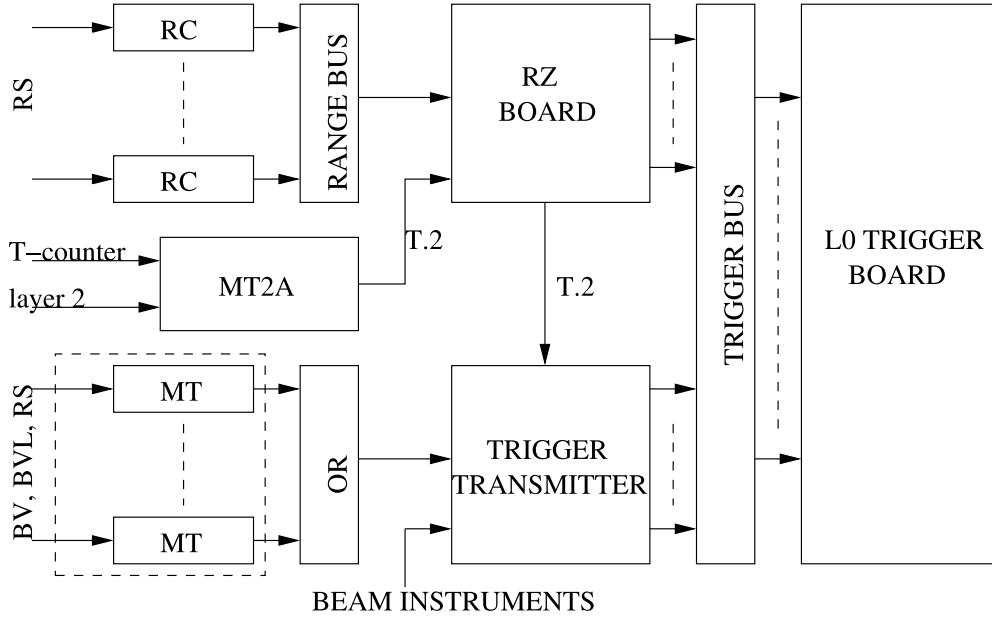


Fig. 17. Block diagram of the L0 trigger system.

particle. The Level-1.2 trigger introduced a dead time of up to $100 \mu\text{s}$ per Level-1.1 trigger.

2.8.2 $K^+ \rightarrow \pi^+ \nu \bar{\nu}$ Triggers

The trigger conditions for $K^+ \rightarrow \pi^+ \nu \bar{\nu}$ were designed differently according to the π^+ momentum. For high π^+ momentum, the trigger condition, called *pnn1*, was defined as:

$$pnn1 = \frac{KB \cdot DC \cdot (T \cdot 2) \cdot (6_{ct} + 7_{ct}) \cdot \overline{19_{ct}} \cdot \overline{zfrf} \cdot L0rr1 \cdot (BV + BVL + EC)}{HEX \cdot L1.1 \cdot L1.2} \quad (15)$$

where KB required that a K^+ was identified in the K^+ Čerenkov counter, and was detected in the B4 counter and the target. The delayed coincidence (DC) required that the time of the outgoing π^+ in the IC was at least 1.5 ns later than the time of the incoming K^+ in KB . The $T \cdot 2$ signal was a coincidence of the OR of the IC's and the first layer of the RS (T counter) with the second layer (2 counter) in the same sector, which ensured that the π^+ entered the RS and defined the fiducial volume of the detector. The trigger bit $6_{ct} + 7_{ct}$ required that π^+ reached the 6th or 7th layer of the RS and suppressed the copious 3-body $K^+ \rightarrow \pi^+ \pi^- \pi^+$ or $K^+ \rightarrow \pi^+ \pi^0 \pi^0$ backgrounds. The $\overline{19_{ct}}$ signal required that the π^+ should not reach the 19th layer in order to suppresses $K^+ \rightarrow \mu^+ \nu_\mu$ ($K_{\mu 2}$) background. The “*ct*” designated the RS sectors that were associated with a $T \cdot 2$ ($T \cdot 2$ sector plus the next two clockwise sectors: this was the direction that a positive particle moves in the magnetic field). The $L0rr1$ bit was a refined calculation of the charged track range, which included the number of target fibers hit and a measurement of the z-position of the track from flash TDC's on layers 10–12 as well as the deepest layer of penetration of the track; this rejected events with long range such as the μ^+ from $K_{\mu 2}$ decay. The photon veto $\overline{BV + BVL + EC}$ and HEX were from the barrel veto, barrel veto liner, end-cap and RS, respectively, which removed events with photons such as $K^+ \rightarrow \pi^+ \pi^0$ ($K_{\pi 2}$), $K^+ \rightarrow \pi^0 \mu^+ \nu_\mu$ ($K_{\mu 3}$) and $K^+ \rightarrow \mu^+ \nu_\mu \gamma$ ($K_{\mu 2 \gamma}$). The \overline{zfrf} condition was an fiducial cut on the z-position of the charged track in each layer from the meantimers, vetoing tracks that cross anywhere near the edge of the fiducial volume. The $L1.1$ and $L1.2$ represent the level-1.1 and level-1.2 triggers, which used data processed from the TD's and ADC's respectively.

For lower π^+ momenta the trigger condition, called $pnn2$, was defined as:

$$pnn2 = \frac{KB \cdot DC \cdot (T \cdot 2) \cdot 3_{ct} \cdot 4_{ct} \cdot 5_{ct} \cdot 6_{ct} \cdot}{(13_{ct} + \dots + 18_{ct}) \cdot 19_{ct} \cdot (BV + BVL + EC)} \cdot HEX \cdot L0rr2 \cdot L1.1 \cdot L1.2 \cdot (ps16 + \overline{C_\pi}) \quad (16)$$

Where $L0rr2$ was a cut on the refined range calculation of the low-momentum charged track (it was set to cut only events with too many target hits).

The Level-0 $pnn1$ ($pnn2$) trigger had a rejection of ~ 700 (1200), combined with the Level-1.1 trigger rejection of ~ 11 (10) and the Level-1.2 trigger rejection of ~ 2 (2), the entire trigger therefore had a rejection of ~ 15000 (25000), and reduced the 2.6×10^6 K^+ s entering the target when the detector was live to 160 (100) events per spill.

2.8.3 Monitor Triggers

In addition to the $K^+ \rightarrow \pi^+ \nu \bar{\nu}$ triggers, there were monitor triggers for calibration and normalization, as well as triggers for other physics modes. All triggers were prescaled except for the $K^+ \rightarrow \pi^+ \nu \bar{\nu}$ triggers and the 1γ trigger for study of the decays $K^+ \rightarrow \pi^+ \gamma \gamma$ and $K^+ \rightarrow \pi^+ \gamma$.

To monitor detector performance several triggers were employed, including $K_{\pi 2}$, $K_{\mu 2}$, Beam π^+ and Beam K^+ . These monitor samples were used for calibration and acceptance studies. They were taken simultaneously with the pnn triggers and were prescaled so that their impact on the total dead time was small.

The $K_{\mu 2}$ decay has the largest branching ratio. Since the final state does not contain photons or additional tracks and the daughter μ^+ does not interact with the nuclei it was a convenient sample for a variety of acceptance measurements as well as several calibrations. This sample was also used for the normalization of the experiment; the measurement of the $K_{\mu 2}$ branching ratio effectively normalizes the counting of K^+ s to the well known $K_{\mu 2}$ branching ratio. The trigger condition for $K^+ \rightarrow \mu^+ \nu_\mu$ ($Km2$) was defined as follows

$$Km2 = KB \cdot (T \cdot 2) \cdot (6_{ct} + 7_{ct}) \cdot \overline{17_{ct} + 18_{ct} + 19_{ct}} \quad (17)$$

The final state of the $K_{\pi 2}$ decay mode contains one charged π^+ and two photons from π^0 decay. Since the π^+ momentum is monochromatic, it can be used to check the measurements of charged track momentum, range and energy. Also the π^+ can be used to study particle identification, and the photons can be used to study the photon veto. Two $K_{\pi 2}$ triggers were defined, a loose one, $Kp21$:

$$Kp21 = KB \cdot (T \cdot 2) \cdot (6_{ct} + 7_{ct}) \cdot \overline{19_{ct}} \quad (18)$$

and a tighter one, $Kp22$:

$$Kp22 = KB \cdot DC \cdot (T \cdot 2) \cdot (6_{ct} + 7_{ct}) \cdot \overline{19_{ct}} \cdot HEX \cdot L1.n \quad (19)$$

Among the incoming beam particles there were many π^+ s, including some that scattered into the fiducial volume of the RS. These beam π^+ s were identified by the Čerenkov counter. The kinematic features of this π^+ sample was almost the same as the $K^+ \rightarrow \pi^+ \nu \bar{\nu}$ signal except that the target pattern was different. This sample was suitable for calibrating the dE/dx of π^+ s and for studying the acceptance. The trigger condition for the beam π^+ was defined as:

$$\text{Beam } \pi^+ = \frac{\pi B \cdot \overline{DC} \cdot IC \cdot (T \cdot 2) \cdot}{(BV + BVL + EC)} \cdot HEX \quad (20)$$

In the K^+ beam trigger, only the K^+ Cerenkov counter was involved. Therefore, this monitor sample was used to evaluate the individual trigger efficiencies. The trigger condition for the K^+ beam monitor was defined as:

$$\text{Beam } K^+ = KB \quad (21)$$

The charge exchange process (CEX), $K^+n \rightarrow p + K_L^0$ followed by $K_L^0 \rightarrow \pi^+ l^- \bar{\nu}_l$ can be a background to the $K^+ \rightarrow \pi^+ \nu \bar{\nu}$ search when the low momentum charged lepton l^- from the K_L^0 decay is undetected. The main issue for this background study is how to precisely obtain the corresponding reaction rate. Since K^0 has equal fraction of K_L^0 and K_S^0 , there is no difference between $K^+n \rightarrow p + K_L^0$ and $K^+n \rightarrow p + K_S^0$. Experimentally, the K_S^0 decays to $\pi^+ \pi^-$ can be well identified. The decay rate as measured from $K^+n \rightarrow p + K_S^0$ can be applied to the determination of the $K^+ \rightarrow \pi^+ \nu \bar{\nu}$ background from $K^+n \rightarrow p + K_L^0$. Based on this consideration, a trigger condition for CEX to tag two charged tracks was defined as:

$$\text{CEX} = KB \cdot \overline{DC} \cdot 2(T \cdot 2) \cdot (6_{ct} + 7_{ct}) \cdot \overline{EC + \pi B} \quad (22)$$

High energy cosmic rays can penetrate the entire detector with almost no deflection, leaving a straight track in the detector when the magnetic field is off. This feature of high energy cosmic rays can be used for the geometrical alignment of the detector elements. The trigger condition required:

$$\text{Cosmic} = T \cdot 2 \cdot IC \cdot \overline{BG} \text{ or } T \cdot 2 \cdot (> 1 \text{ non-adj } IC) \quad (23)$$

Type	Model	Standard	Resolution	Subsystems
ADC				
	LRS 4300B LRS 1881	Camac Fastbus	10 bits 13 bits	RS,BV,BVL,EC,Beam Target,UTC
TDC				
	LRS 3377 LRS 1879 LRS 1876	Camac Fastbus Fastbus	0.5ns 2ns 1ns?	RS, BVL UTC,EC,Beam BV,TT
WFD				
	TD CCD	Fastbus Fastbus	500 MHz sampling 8 bits, 10 μ s depth 500 MHz sampling 8 bits, 256ns depth	RS,BVL,IC B4,Target,EC

Table 2. Digitizing electronics for E949 (needs to be double-checked)

2.9 Data Acquisition

Analog- and discriminated- signals from the detector were digitized by commercial ADC and TDC, and custom-built waveform digitizer (TD and CCD) systems. When an event was accepted by the trigger system, the digitized data for the event was transferred to a buffer module or a local crate controller. At the end of each spill, the data for the spill was transferred to a host computer. A block diagram of the DAQ system is shown in Figure 18. A summary of the digitizing electronics is in Table 2.

For the Fastbus systems, SLAC Scanner Processor (SSP) modules[46] served as crate controllers and to read out and reformat/buffer the data from the front-end after each trigger accept. The CAMAC ADCs were read out through the FERA bus by a Struck XXX(**need to give the module number**) DSP (Fastbus) module. The CAMAC TDC's were read out by custom-built DY3 modules[47] which pushed the data into VME memory boards. The readout time per event (as determined by the slowest crate) was typically 850 μ s.

At the end of each spill, the data from the Fastbus buffer memories were read out via the cable segment (12-15 MB/sec) by Struck XXX(**need to give the module numble**) SFI modules, each controlled by a MVME 2604 single-board computer (SBC) running VxWorks. The VME memory boards were read out by a separate SBC. Data was transferred from the SBC's to the host computer (SGI Origin 200) via Ethernet (9 MB/sec per link) through a simple network switch. Event fragments from the readout segments were combined by Event Builder processes running on the host computer. Complete events were distributed to "consumer" processes which included data logging and online monitoring. $K^+ \rightarrow \pi^+ \nu \bar{\nu}$ triggers were written to two DLT-7000 drives at 5 MB/sec per drive; a third DLT drive was used to log monitor triggers.

A slow control system, based on the MIDAS[48] framework, ran independently of the main DAQ system and was used to monitor a variety of experiment conditions, including crate voltages and temperatures.

Under typical running conditions, we wrote 300 (**need an accurate number**) events/spill with a typical event size of 80 kB **need an accurate number**. This was well within the maximum throughput of the system of about 50 MB/spill. The DAQ dead time was due entirely to the speed of the event-by-event readout of the front-end electronics at the crate level; typically this amounted to about 12%(**need an accurate number**).

The total dead time introduced by the trigger and DAQ was typically 25%.

2.10 Data Collection

The E949 experiment had its first physics runs for 12 weeks from March to June in 2002, about 20% out of the approved beam time by DOE. The data collected on disk in this run period corresponds to 1.77×10^{12} K^+ 's exposure in the target. The $K^+ \rightarrow \pi^+ \nu \bar{\nu}$ data sample are classified into two categories: the momentum region above and below the $K_{\pi 2}$ peak, referred as *pnn1* and *pnn2* sample.

3 Data Analysis

The branching ratio of the $K^+ \rightarrow \pi^+ \nu \bar{\nu}$ decay is expected to be at a level of 10^{-10} in the SM. Unlike the $K_{\mu 2}$ background and the $K_{\pi 2}$ background, the $K^+ \rightarrow \pi^+ \nu \bar{\nu}$ decay signal is of a continuum momentum with no peak. To ensure that an observed candidate event really come from the $K^+ \rightarrow \pi^+ \nu \bar{\nu}$ decay, one must require all the backgrounds be completely understood and be eventually suppressed to less-than-one event level. In this section, after a brief overview of the sources of background, the technique of data analysis will be described, including the selection criteria, background evaluation, signal candidate search and acceptance measurement.

3.1 Overview of Background

Data surviving from the online trigger were primarily from background events as shown in Figure 19. According to their origins, these events are classified into stop K^+ decay related and beam related backgrounds.

3.1.1 Origins of Stopped K^+ Decay Background

The stop K^+ decay related backgrounds can be further categorized into two types: π^+ -related, μ^+ -related backgrounds. As shown in Figure 4, multi-body K^+ decays can be suppressed by setting a signal momentum region higher than the $K_{\pi 2}$ peak but lower than the $K_{\mu 2}$ peak, namely the $pnn1$ sample. However, since $K_{\pi 2}$ and $K_{\mu 2}$ are both of large branching ratios (20.92% and 63.44%), they can migrate into the signal region through either resolution effect or scattering effect. For the $K_{\mu 2}$ decay mode, the background originates from a $K_{\mu 2}$ peak event or a $K_{\mu 2}$ range tail event when the particle identification is fooled. This is also applicable to the $K_{\pi 2}$ decay mode when the photon escapes from the detection. Since the photon carries part of energy from a radiative $K_{\mu 2}$ decay, the μ^+ range, energy and momentum will not be in the peak positions, resulting in the observed μ^+ band events in Figure 19. Because of the phase space limit, the $pnn1$ analysis only considers the K^+ decay related backgrounds from $K_{\mu 2}$, $K_{\mu 2\gamma}$ and $K_{\pi 2}$.

3.1.2 Origins of Beam Background

The beam related backgrounds are categorized into three types: single beam background, double beam background and charge exchange (CEX) interaction background. These events can show up in the π^+ band and have most of the kinematic characters as the signal events.

The single-beam background involves the following situations: (1) A K^+ enters the apparatus and decays in flight to a π^+ plus a π^0 as illustrated in Figure 20. The kinematic values of the π^+ can be shifted upward to the signal region by the Lorentz boost, faking a $K^+ \rightarrow \pi^+ \nu \bar{\nu}$ signal event. (2) A π^+ beam misidentified as a K^+ scatters in the target and then enters the fiducial region of the detector as illustrated in the bottom diagram of Figure 20. This π^+ can mimic a target fiber pattern for signal and, its continuum momentum distribution can cover the signal region as shown Figure 19. Rejection to these two background requires good time delayed coincidence measurement and K^+ beam identification.

The following cases are classified as the double-beam background. In the first case, one K^+ enters and comes to rest in target another K^+ enters the target and decays in flight to π^+ . This decay product π^+ then goes through the fiducial region of the detector (see the top diagram in Figure 21). The second case is almost the same as the first one, except that the π^+ scatters in the target and enters the fiducial region. (see the bottom diagram in Figure 21). Both cases can imitate a $K^+ \rightarrow \pi^+ \nu \bar{\nu}$ signal if the decay products from first K^+ is missed. Rejection to these two backgrounds must rely on the ability in observing extra activities coincident with the charged track in the beam instrumentation, target and RS.

In CEX background, a K^+ beam (~ 100 MeV at the entrance of the target) produces K_S^0 via charge exchange reaction. The other reaction products are not easily identified in the target. A K^0 being a superposition of the two mass eigenstates, K_S^0 (mean life 8.95 ns) and K_L^0 (mean life 51.8 ns) promptly

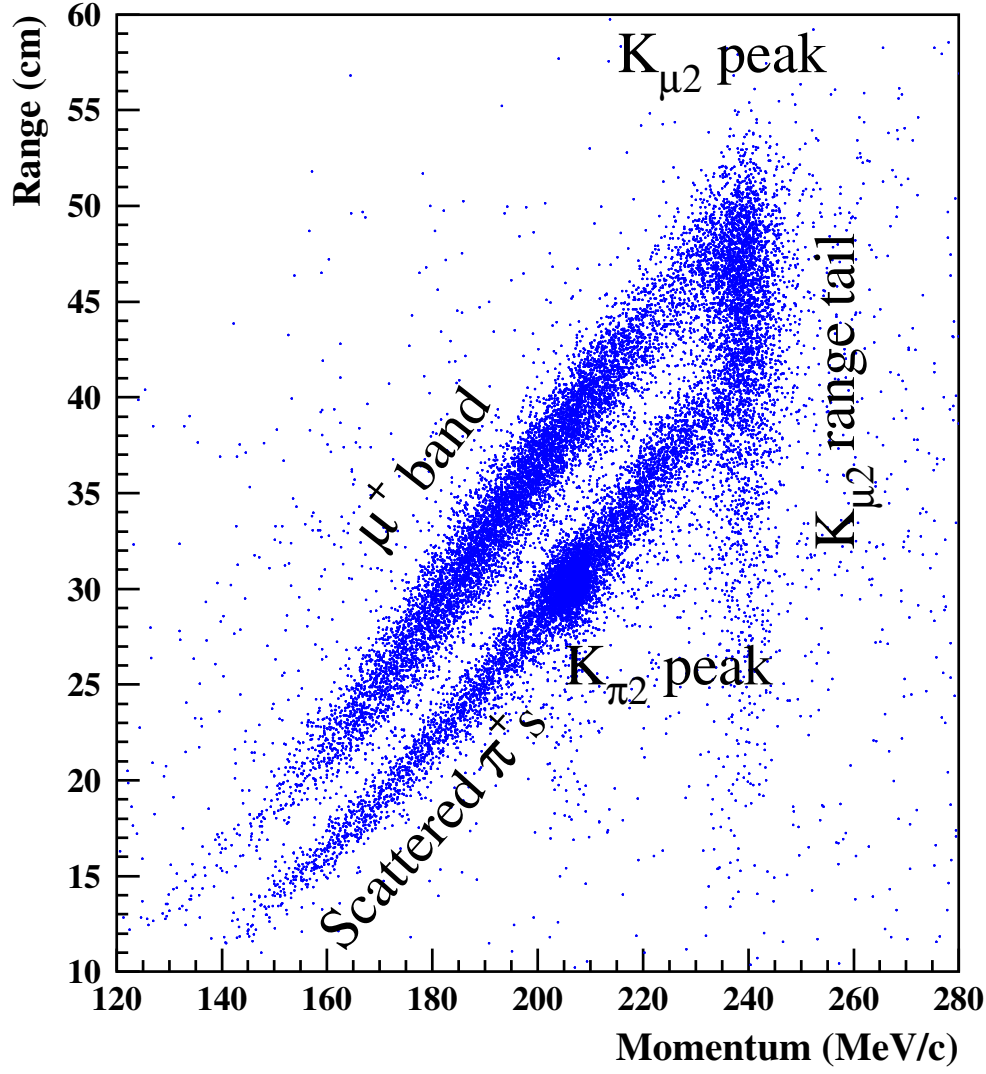


Fig. 19. Range in a plastic scintillator (in cm, y -axis) versus the momentum (in MeV/ c , x -axis) of the charged particles for events that pass the $pnn1$ or $pnn2$ trigger.

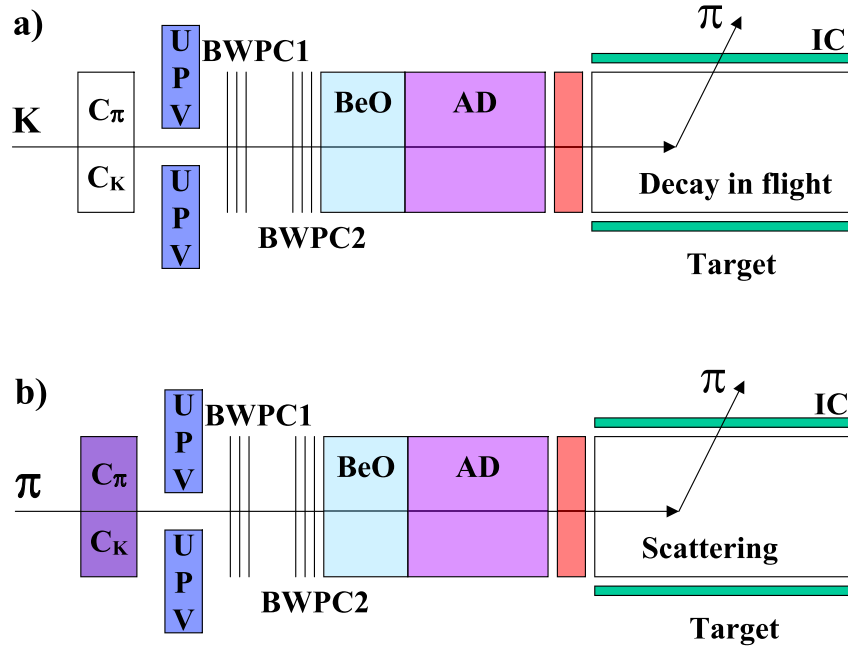


Fig. 20. Schematic diagrams of the single beam background: a) single K^+ beam background and b) single π^+ beam background. The various detector elements and acronyms are described in detail in the text.

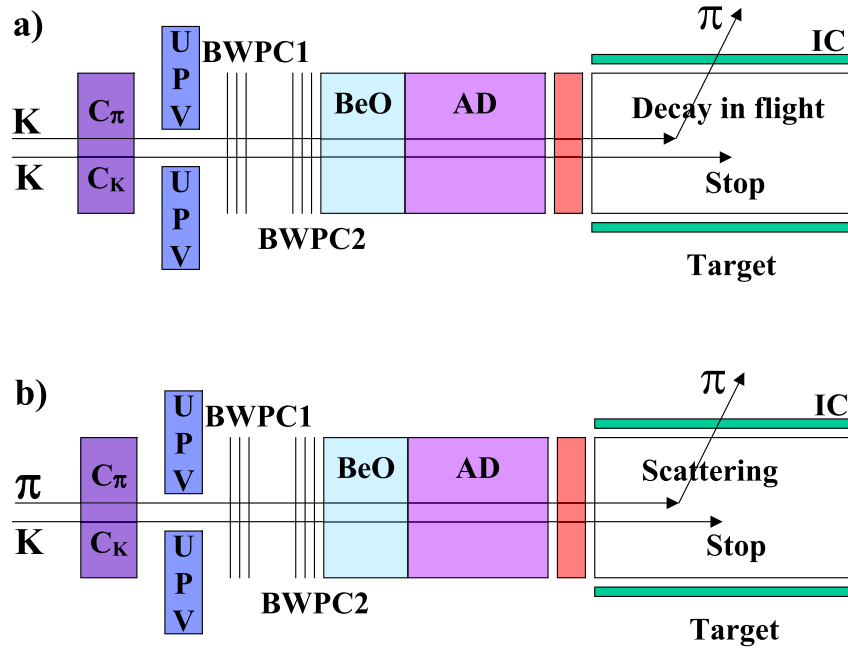


Fig. 21. Schematic diagrams of the double beam background: a) $K^+ - K^+$ double beam background and b) $K^+ - \pi^+$ double Beam background. The various detector elements and acronyms are described in detail in the text.

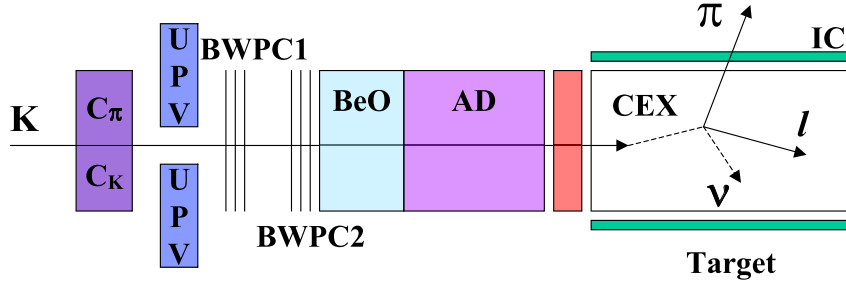


Fig. 22. Schematic diagram of the charge exchange interaction background. The various detector elements and acronyms are described in detail in the text.

turns into a K_L^0 (50% probability), and 67.6% of K_L^0 decays semi-leptonically to $\pi^\pm l^\mp \nu_l$, where l stands for e (K_{e3}^0) or μ ($K_{\mu3}^0$). These three body decays can be a background if the energy of lepton can be too low to be detected beyond the target. Because both the $pnn1$ and $pnn2$ triggers require only one charged track in each event, most of them will be rejected by the triggers. The signature of a K_{e3}^0 or a $K_{\mu3}^0$ background is a π^+ track plus a soft undetected e^- or μ^- (see Figure 22).

Rejection to the CEX can be achieved by using the fact that a K_L^0 does not deposit energy along the path in the target, leaving a gap between K^+ and π^+ fibers in the target. Also can be exploited is that this CEX reaction process has no time delay. Both of which will be the key ingredients in rejecting the CEX background.

3.2 Analysis Method and Strategy

Disentangling the $K^+ \rightarrow \pi^+ \nu \bar{\nu}$ from background is difficult because of the poor kinematic signature and very small expected rate of the $K^+ \rightarrow \pi^+ \nu \bar{\nu}$ signal. Backgrounds must be estimated from the data when possible because background mechanisms cannot be well simulated at a level commensurate with the required sensitivity of less than $\sim 10^{-10}$. As detailed below, care is taken to limit or avoid bias in background estimation that may rely on samples with low statistics.

3.2.1 Blind Analysis Method

A so-called “blind” analysis method is adapted to search for the $K^+ \rightarrow \pi^+ \nu \bar{\nu}$ signal. That is, background sources are identified as *a priori* and, the signal region for the $pnn1$, determined in such that the sensitivity is optimized, is “blinded” or hidden until the analysis is complete. When possible, selection criteria are developed using the monitor samples to avoid examining the signal region. If monitor samples are inadequate and the $pnn1$ trigger sample must be used, at least one selection criterion is inverted to avoid examining the signal region. In addition, the background evaluations are performed such that the final background estimates are obtained from the different samples than that used to determine the selection criteria. The $pnn1$ data are randomly divided into one-third and two-thirds portions uniformly sampled throughout the data-taking period. The one-third portion is used to determine the selection criteria and an unbiased background estimate is obtained from the two-third portion. When the background analysis is complete, the signal region is unblinded and the properties of any signal candidates are carefully examined to exclude flaws in the analysis procedure. If no flaws are found, as is the case for the results reported here, the estimate of the $K^+ \rightarrow \pi^+ \nu \bar{\nu}$ branching fraction remains unbiased.

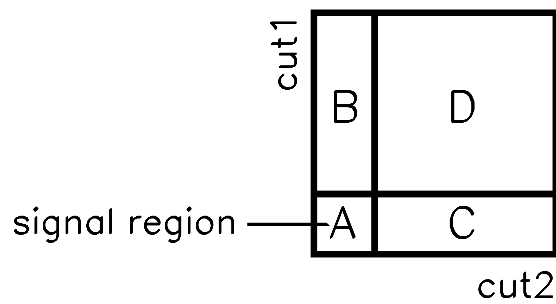
3.2.2 Bifurcation Method for Evaluating Background

The bifurcation method is based on a simple algebra, providing an evaluation of background with information outside the signal region. Three separated background regions are defined by the different cut configurations, in order to give an estimate of the background level inside the signal region. A pictorial explanation for the bifurcation method is shown in Figure 23.

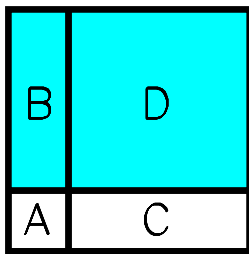
This method relies on the assumption that the two bifurcation cuts are uncorrelated. Each figure in Figure 23 shows the parameter space of two cuts, namely “CUT1” and “CUT2”. The number of background events in the signal region (i.e., region “A”) is A events. If the two cuts are uncorrelated, that is, if the rejection of a cut does not depend on the rejection of the other cut, the ratio of the number of background events in region “A” to region “B” must be equal to the ratio in region “C” to region “D”, i.e., $A/B = C/D$. Background events in the signal region are therefore obtained from the relation $A = BC/D$.

In practice, the bifurcation analysis is done through two branches. A “normalization branch” analysis is to get the number of events in B region. On the other hand, a “rejection branch” study is to get the ratio of D/C . The rejection is defined as $R = 1 + D/C$. The background level is then estimated as $N_{Bkg} = B/(R - 1)$ in the signal region. For the case of very small statistics, “CUT1” is subdivided into another two cut categories, and B is estimated in the same way as the “first” bifurcation.

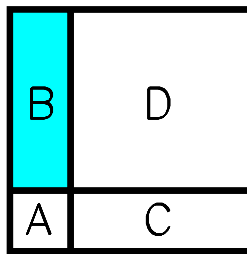
To check if the two bifurcated cuts are indeed uncorrelated, one can loosen both them simultaneously. The loosen factors are controlled by the so-called background functions, in which the loosen factors are the inputs and the outputs are the cut positions. They can also provide the relative background level and the acceptance as well. With the loosen cut positions, the previous four regions (A, B, C, D) become (A', B', C', D'). It should be noted that the signal region A in A' should be masked out, resulting in new region in A' is referred to as the “outside-the-box” region. This number should agree with the observed one from $B'C'/D'$, if the CUT1 and CUT2 are truly uncorrelated. This can thus provide an access to the evaluation of systematic uncertainty.



if cut1, cut2
 uncorrelated,
 $A/B = C/D$
 $A = BC/D$

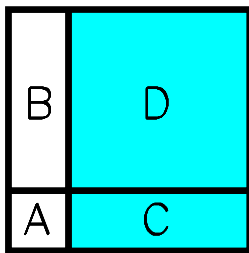


invert cut1
 B+D events

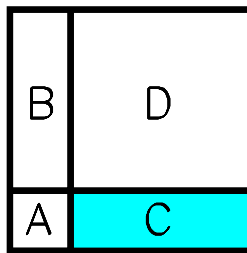


apply cut2
 B events

$$N = B$$



invert cut2
 C+D events



apply cut1
 $R = (C+D)/C$

$$\begin{aligned} \text{bg} &= N/(R-1) \\ &= BC/D \end{aligned}$$

Fig. 23. Pictorial explanation of the bifurcation method.

3.2.3 Analysis Strategy

Data analysis will take the following key steps to determine the selection criteria, evaluating the background level, investigating the systematic uncertainty, measuring the acceptance and finally deriving the branching ratio.

- Data will be first reconstructed and go through a number pre-selection criteria for removing the obvious junk. Then they will be randomly divided into one-third and two-thirds portions, in which three sub-samples will also be skimmed out according to the background features, to simplify the analysis (see Section 3.5).
- Blind analysis will be adopted in designing, calibrating and tuning the selection criteria. Signal and background samples should be from the monitor trigger samples whenever they are applicable. If the one-third of three skimmed sub-samples must be used, at least one critical selection criterion should be inverted to avoid accidentally looking into the signal region (see Section 3.6).
- Background level will be initially evaluated by applying the bifurcation method to the one-third data. At least two uncorrelated cuts with large background rejections will be chosen and then inverted sequentially to create high-statistic background data samples. A simple algebra will be used to derive the background levels estimated in the signal region (see Section 3.7.1-3.7.5).
- The final cut positions will be optimized with respect to the total background level estimated from the one-third data. This can be achieved by using the background functions estimated in the bifurcation analysis (see Section 3.7.6-3.7.7).
- Correlation between the bifurcated cuts will be checked by conducting a series of re-evaluating the background levels outside the signal region. A study of single cut failure will also be conducted to investigate the possible loop hole. Whether or not there is a bias in the analysis can be checked by comparing the results between the one-third and two-third portions. Final background evaluations will come from the two-thirds portion (see Section 3.7.8-3.7.9).
- Acceptances will be measured with the monitor trigger samples except for the signal phase space and the trigger efficiency. Both of these two exceptions will be obtained from Monte Carlo. The branching ratio of $K_{\pi 2}$ will be used to validate the acceptance measurement. Single event sensitivity will be from the inverse product of the total K^+ exposures and the acceptance. (see Section 3.8).
- Signal region will be examined after the final total background level is estimated to be much less than one event. Events observed in this region are all counted as the signal candidates (see Section 3.9).
- Branching ratio will be either simply from the sensitivity measurement if no event is observed, or from a likelihood analysis incorporated with the background functions in the signal region if candidates are found (see Section 4).

3.3 Event Reconstruction

Throughout this analysis, the events are reconstructed under the assumption that they are $K^+ \rightarrow \pi^+ \nu \bar{\nu}$ events with only a single charged track each in the detector. The kinematics of the track are then calculated using a π^+ hypothesis.

3.3.1 Clustering in RS

Track reconstruction starts from finding clusters in RS. The hit counters of a positively-charged track (referred as the track counters) are searched using the TDC timing information in RS. A good $T \cdot 2$ sector must be the first two coincident RS layers in the same sector. From this $T \cdot 2$ sector, the adjacent 10 ns coincident counters with energy greater than 0.5 MeV are then searched in the outgoing and clockwise direction to find the track counters. A good cluster should cross at least six layers from inside out. Once a RS track cluster is identified, the track time t_{rs} will be computed by averaging the measurements of the track counters. The stopping counter is defined as the outermost layer and the most clockwise sector in this cluster. The $T \cdot 2$ hit in a cluster will provide a guideline for tracking in UTC.

3.3.2 Tracking in UTC

When a RS cluster is established, UTC tracking can start from searching clusters of the hit anode wires in $x-y$ plane[41]. Hit wires in each super layers are grouped into clusters based on their spatial proximity to one another. The drift distance is derived from the time measurement after pedestal subtraction. Using a straight line fit to get a crude vector in each super layer. These vectors are then linked to form a track segment in the UTC. A circle track of fit is performed with a set of drift distances plus a left-right ambiguity solution. The radius of circle gives the measurement of transverse momentum, taking account of the magnetic field variation described ed in Section 2.5.

If an UTC track in $x-y$ plane is successfully found, the corresponding track projection on the $r-z$ plane will be searched at each UTC cathode foil, and clustering the hit strips based on timings. A ± 15 ns of time consistence is required for the strip hits belonging to the same cluster in each foil. Due to the high rate, cathode strip may be affected by the accidental hits, which may cause a confusion in determining the z position. A pulsate method is applied to distinguish multiple hits in one cluster. The calculation of the z position for a cluster adopts the ratio method suggested by Reference[54], which uses three strips with highest ADC counts to derive the centroid, reducing the bias on the z position measurement due to the noise. A straight line fit is performed in $r-z$ plane if the z hits are found in at least 3 foils, determining the slope and intercept. The slope divided by the radius gives a measurement on the cosine of polar angle, which is then used to convert the measured transverse momentum to the longitudinal one.

In case of more than one track pointing to the same $T \cdot 2$ sector, the one closest to the first RS sector crossing point or to the clock-wise edge of the stopping counter otherwise, will be picked up as the good UTC track. The UTC tracking efficiency is checked with the $Km2$ monitor data and is measured to be better than 95%. The inefficiency is due to the fact that high rate environment can give more chance to pick up accidental hits in the UTC tracking, and can thus cause a problem of pattern recognition.

3.3.3 Tracking in Target and B4

After an UTC track is found, target pattern recognition starts to look for the K^+ and π^+ fibers on a 1 cm space passage along the UTC track extrapolation in the target. Traveling nearly in almost along the target fibers, the K^+ beam usually deposits more energy (usually greater than 4 MeV) in each fiber and has time coincidence with the beam time t_{BW} as well. On the contrary, the daughter π^+ travels nearly perpendicular to the target fibers, and thus leave less energy (1 MeV in average) in each fiber and have time coincidence with the track time t_{rs} . The t_{BW} , t_{rs} and fiber energy are the key elements to identify the K^+ and π^+ fibers. All the K^+ and π^+ fibers are linked to form a K^+ cluster and a π^+ cluster. A good event should only have one K^+ cluster and one π^+ cluster. The corresponding energy (δE_K , δE_π)

and time (t_K, t_π) are calculated from the sum and average of the clusters, respectively. The range of π^+ in the target is calculated as the arc traveled by the π^+ from the K^+ decay position to the inner wall of the IC. The π^+ hypothesis is always made for all the charged particles from the K^+ decay.

Because of the unknown entry and stop ends of the incoming beam, the target reconstruction can be complicated. This can be improved by using the B4 measurement on the K^+ entrance point, which is reconstructed by clustering the hits in the two B4 layers according to their locations and times determined by both TDC and CCD informations. Each B4 cluster can provide the other beam time measurement t_{BM} and the dE/dx measurement. The cluster with t_{BM} closest to the t_K is chosen as the one caused by the K^+ beam. The entrance point is determined by averaging all the hits in this cluster with corresponding energy weight. A 0.36 cm position precision can be obtained by the B4 hodoscope in the $x - y$ plane.

Target CCD information can help the pattern recognition and give better accuracy in finding the fiber clusters, especially for the pile-ups of hits in a fiber. When t_K and t_π are separated by more than 2 ns, the CCD pulses in all of the K^+ fibers are studied to identify if there is any hidden π^+ energy. The resulting correction can thus provide a full target π^+ energy measurement. The K^+ decay vertex in $x - y$ plane is determined by the K^+ fiber closest to the UTC track but furthest from the K^+ entrance point determined by the B4, while the z position is calculated from the UTC track extrapolation in $r - z$ plane.

Hit fibers caused by possible photon(s) or other beams are all taken from the rest belonging to neither K^+ nor π^+ fibers, as long as their energies are greater than 0.1 MeV, with a swath wider than 1 cm and in ± 5 ns time consistent with the t_{rs} . These photon fibers are used for the target photon veto and the π^0 energy reconstruction.

Once the first round of target reconstruction is finished, one can know the π^+ passage and K^+ decay vertex in the target. The procedure of UTC track fitting will be repeated with these additional information. This can give a better position solution for the left-right ambiguity in the UTC track reconstruction, since a good charged track should have a good matching between target and UTC. Iteration of the target reconstruction is also performed with the improved UTC track.

3.3.4 Track Passage in IC

The hit IC sector should be the same one determined by the UTC track extrapolation. An ideal IC hit is only one sector per event, though there is an exception of IC sector crossing. It is observed that 1% of tracks with extra hits in IC's, confusing the measurements of energy and time in IC's. This is solved by also using the TD information in addition to the TDC and ADC information. The IC time t_{IC} is always the one closest to the t_{rs} and, the corresponding energy is taken as the energy of IC. The range of track in the IC is computed from the inner wall to the outer wall using the UTC track extrapolation. If there is an IC sector crossing, the energy is from the sum of two IC sectors and the t_{IC} is from the average with energy weight.

3.3.5 Tracking in RS and RSSC

With a charged track well reconstructed in UTC and target, the tracking in RS starts from the previously found RS cluster. The stopping counter is first analyzed by fitting with a TD double pulse assumption to find a $\pi^+ \rightarrow \mu^+$ decay signature. This can also determine the μ^+ energy E_μ from the π^+ decay at rest.

Sector crossing search in RS is conducted as illustrated in Figure 24. A $K^+ \rightarrow \pi^+ \nu \bar{\nu}$ candidate should not have no more than 2 sector crossings. Precise position measurement in $x - y$ plane can be obtained from the sector crossing points in $x - y$ plane. The z position is determined by using the end-to-end timing difference with ADC weight in each hit counter except for the T-counter, though the resolution is about 4 to 5 cm.

Another precise position measurement is provided by the RSSC's. The candidate RSSC clusters are searched in the hit chambers. All the adjacent hit straw tubes are linked together to give a cluster in each

RSSC layer. Then one cluster per layer is picked according to which is the closest to a series of arcs drawn from the UTC extrapolation to the T counter through the sector crossings. The $x - y$ position is from the average of two sub-layers or the inner (or outer) layer. To avoid cross-talk effect, the earliest hit in one sub-layer is chosen as the true hit. The z measurement is given by the time difference, and the precision is about 1.5 cm.

A RS track in $x - y$ plane is fitted by using the entrance point provided by the UTC track extrapolation, the sector crossing point(s), the RSSC hit position(s) and the expected positions predicted by the energy deposits in the RS layers, taking account of that the track is propagated by losing energy with the Bethe-Block equation and by bending in a 1 Tesla magnetic field. The fitting χ^2 is minimized by changing the incident momentum and the angle at the entrance to RS (see Figure 24).

The range in the RS is calculated from the path length of the fitted track with the polar angle correction, in which the projection of the track onto the $r - z$ plane is simply from the extrapolation of the UTC track to the center of stopping counter. The total energy deposit of the track in the RS is obtained by summing up the energy deposits in the track counters, with δE_μ subtracted from the energy in the stopping counter.

3.3.6 Kinematic Measurements of a Track

Energy and range measurements of charged tracks, as well as the momentum measurement, are crucial to distinguish the π^+ s in the signal region from backgrounds due to the $K_{\pi 2}$ and $K_{\mu 2}$ decays, since both of them have monochromatic momenta of 205 and 236 MeV/c, respectively. The UTC gives a measurement of momentum for a charged track when it flies out the target. The RS provides most of energy and range measurements for the charged tracks. Final results should also combine the measurements from the target and the correction for the UTC dead material as well.

Finally, the total momentum P_{tot} of a charged track is corrected for the contributions from the UTC, the target and the IC. The total range R_{tot} (energy E_{tot}) of the track is calculated by adding the target range (energy), the IC range (energy) and the RS range (energy). Since the momentum loss in both target and IC is calculated from the range, a certainty level of correlation between P_{tot} and R_{tot} is expected and should be considered in the bifurcation analysis. All of these three kinematic measurements also include tiny contribution from the dead materials of the UTC as well. A successful track reconstruction provides measurements on the basic quantities, such as P_{tot} , R_{tot} , E_{tot} , t_K , t_π and t_{rs} , etc. In this analysis, the momentum, energy and range resolutions were measured to be 1.1%, 2.8% and 2.9% (RMS) for the fully contained $K_{\pi 2}$, respectively. For the $K_{\mu 2}$ decays, they are 1.3%, 2.9% and 3.1%.

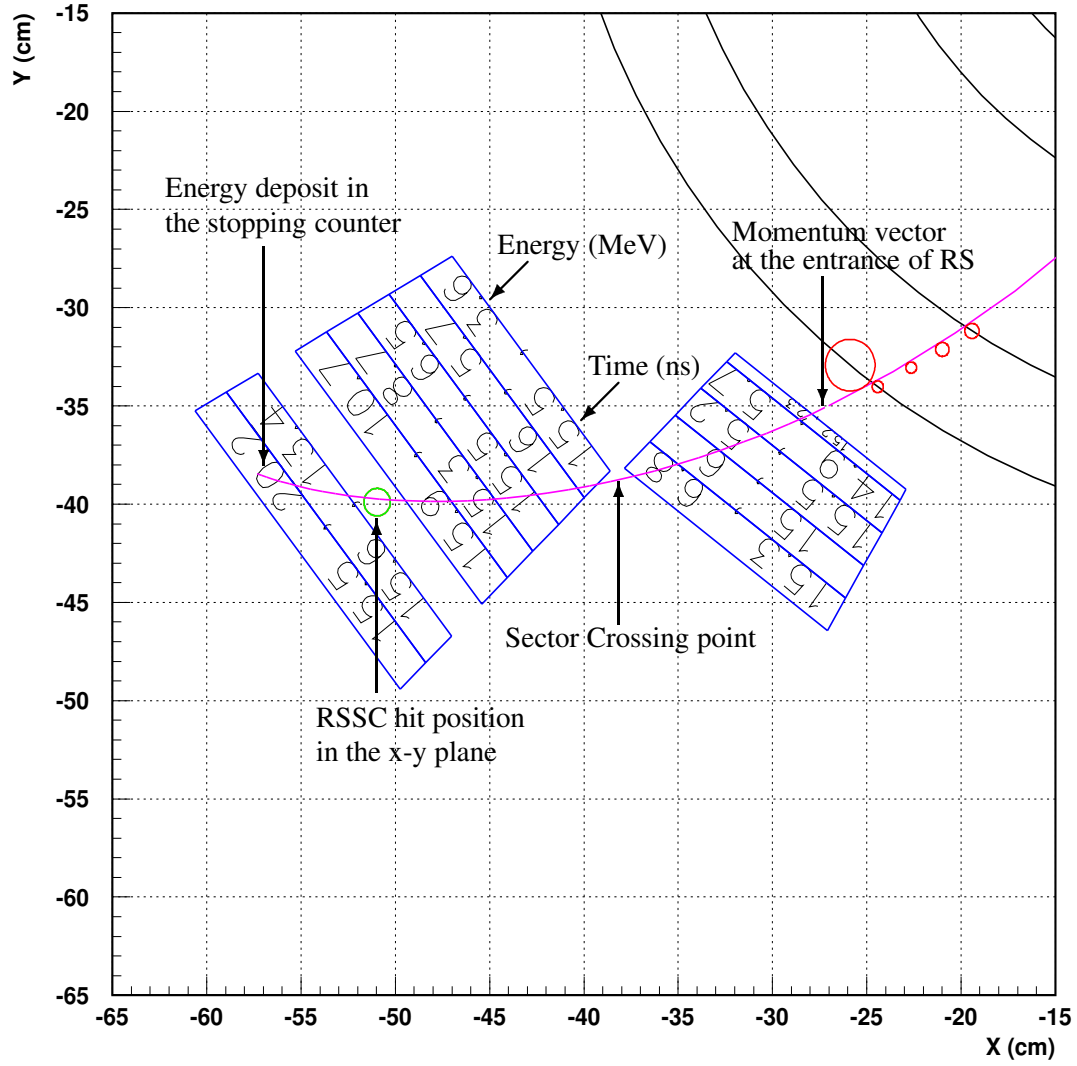


Fig. 24. Illustration of the Range Stack track fitting in $x - y$ plane. All the relevant definitions are given in this plot.

3.4 Monte Carlo Simulation

Detector responses were modeled by a Monte Carlo simulation package, which was written specially for the E787 experiment. The package is an amalgam of subroutines from the EGS4 program and a number of routines written specially for the experiments, including all of the detector elements, except for the beam instrumentation upstream of the target. Simulation sample was generated with the same format as the data except for the TD and CCD pulse-shape information.

3.4.1 Simulation of K^+ Propagation

The simulation of K^+ decays starts from a beam file with the x, y, z positions of K^+ decays in the target, the energy deposits of each K^+ in the B4 hodoscope and the target before the K^+ came to rest. This file is obtained from an analysis of the stopping distribution of the $Km2$ monitor data.

3.4.2 Simulation of K^+ Decay Product

The $K^+ \rightarrow \pi^+ \nu \bar{\nu}$ decay is generated with the matrix element of semi-leptonic $K_{\ell 3}^+$ decay via the (V-A) interaction, while the $K_{\mu 2}$ decay and the $K_{\pi 2}$ decay are generated via pure phase space. Among the K^+ decay products, photon and electron interactions and their energy deposits are calculated using the routines from the EGS4 electromagnetic-shower simulation package[52]. For charged particles like μ^+ s, π^+ s, K^+ s and protons, the energy deposits are calculated by adding the energy losses of each ionization along the steps taken by the particles. The number of ionization and excitation events is determined by dividing the total average energy deposited along the step, obtained using the Bethe-Bloch formula, by the minimum energy a particle loses in scintillator because of an event, taken to be 65 eV. Multiple Coulomb scatterings of charged particles with various nuclei in the detector are calculated according to the theory of Moliere[49], with corrections for the spin of the scattered particle and the form factor of the nucleus[50]. Hadronic interactions of positively charged π^+ s in the plastic scintillators are calculated using a combination of data and phenomenological models[51]. There is an option in the simulation package, allowing users to turn off nuclear absorption reactions and decays in flight of π^+ s. This is useful in study of the acceptance.

3.4.3 Simulation of Trigger

All the trigger conditions are simulated except for the DC, Level-1.1, Level-1.2 and those related to the beam instruments. Since the beam file generated from the $Km2$ monitor data includes the trigger bias, a correction is needed to recover the true beam distribution. This was done by introducing a proper weight function, which is derived from a comparison between the simulated $Km2$ trigger sample and the real data. In order to get a better precision, the perpendicular tracks are used to calculate the $Km2$ trigger acceptance as a function of radial distance of the stopping position in $x - y$ plane.

3.4.4 Comparison between Data and Simulation

The accuracy and performance of the Monte Carlo simulation are verified by comparing the different kinematic resolutions between data and simulation as given in Table 3 for the $K_{\pi 2}$ decay mode. A significant deviation is observed in the range resolution, which is still not understood yet. This difference will be treated as a systematic uncertainty in acceptance measurement. It should also emphasize that the main role of Monte Carlo simulation in the E949 experiment is to estimate the acceptance factors that cannot be obtained from real data (e.g. geometrical and relevant trigger acceptances).

3.4.5 Simulation of Charge Exchange Reaction

Estimate of the CEX background level is obtained from the Monte Carlo simulation. The CEX simulation needs a number of inputs, such as the CEX re-generation rate as a function of K_L^0 energy, the K_L^0 decay vertex and the K_L^0 momentum, all of which can only be taken from the real data. A special

Experiment	σ_P (MeV/c)	σ_R (cm)	σ_E (MeV)
Data	2.299 ± 0.006	0.866 ± 0.002	2.976 ± 0.005
UMC	2.399 ± 0.029	1.018 ± 0.008	3.018 ± 0.025

Table 3. Comparison of the momentum, range and energy resolutions between data and simulation for the $K_{\pi 2}$ peak.

CEX monitor trigger as described in Section 2.8.3 were used for collecting data with two charged tracks from the K_S^0 decay. Reconstructing the K_S^0 momentum and production location can allow one to access the CEX process via the measurement on the re-generation rate, momentum distribution and the B4 hit information, etc. The information for these K_S^0 's are then applied for simulating the generation of their counterpart K_L^0 's.

3.5 Data Processing and Pre-selection

Data are stored on 300 magnetic tapes with a total data size up to 7 Tera bytes. Two steps of data processing (“Pass1” and “Pass2”) are taken to reduce and skim the data to a reasonable volume.

3.5.1 Filtering Data in Pass 1 Phase

The Pass 1 cuts consist of both event reconstruction quality cuts and loose μ^+ background rejection cuts. Bad runs labeled during the data period were removed. Track should be successfully reconstructed. Good charged tracks should not stop in those which had a hardware problem. The track momentum measured by UTC should be less than 280 MeV/c. A $\pi^+ \rightarrow \mu^+$ double pulse should be found by the TD pulse fit to the stopping counter. No extra hit can be observed in the stopping counter. No track hit can be found in the RS hexants consisting of 4 contiguous RS sectors around the stopping counter. Since a photon activity around the stopping counter can cause a confusion in energy measurement, no sector crossing is allowed in the stopping layer. The charged track should not come to rest in the support materials for the second RSSC layer embedded between the 14th and 15th layers. The PASS 1 cuts can reduce the data volume by nearly a factor of two.

3.5.2 Skimming Data in Pass 2 Phase

The Pass 2 cuts are applied to skim the sample surviving from the Pass 1 cuts into three categories for μ^+ -enhanced, γ -enhanced and beam background enhanced, respectively, in order to simplify the background study. Each category was randomly divided into one-third portion and two-third portion. In total there are six streams, the first three and the second three had identical Pass cuts. The Pass 2 cuts consist of five data skimming criteria: quality of the target reconstruction, loose version of the photon veto, quality of the $\pi^+ \rightarrow \mu^+$ double pulse fitting result, single K^+ beam requirement and the delayed coincidence cut. as detailed below

- The target reconstruction requires that the K^+ decay vertex should be inside the target volume. $|t_K - t_{BM}| < 4$ ns and $|t_\pi - t_{IC}| < 5$ ns. The energy deposit in the IC should be consistent with that derived from the expected range.
- The loose photon veto rejects events with $|t - t_{rs}| < 2$ ns and energy greater than 1.5 MeV in BV, or $|t - t_{rs}| < 1.5$ ns and energy greater than 3.5 MeV in EC, or $|t - t_{rs}| < 1.5$ ns and energy greater than 3.0 MeV in RS, or $|t - t_{rs}| < 1$ ns and energy greater than 5.0 MeV in target.
- The $\pi^+ \rightarrow \mu^+$ sequence requires a decay μ^+ pulse in the stopping counter, rejecting the events with hits around this counter and timings to be consistent with the μ^+ time within ± 2.5 ns and 5 ns later than the t_{rs} .
- The beam requirements for signal events are that the B4 dE/dx is greater than 1 MeV that the t_{BM} is off from the t_{rs} by more than 1.5 ns and less than 4 C_π hits to be consistent with the t_{rs} within ± 1.5 ns time window.
- The delayed coincidence requires $t_K - t_\pi > 1$ ns.

Because of the nature of the Pass 2 cuts listed in Table 4, Skim 1-4, Skim 2-5 and Skim 3-6 are $K_{\pi 2}$ -enhanced, μ^+ -enhanced and beam-enhanced sub-data sets. These six Pass 2 output data streams can therefore promote the study in both developing the final selection criteria and evaluating the backgrounds. One should be aware that signal candidates, by the definitions of the Pass 2 cuts, are still kept in either one of the six stream. Study of selection criteria using these samples should always be done with at least one cut inverted to ensure that a blind analysis is truly conducted.

Cuts	Skim 1 or 4	Skim 2 or 5	Skim 3 or 6
Target reconstruction	✓	✓	✓
Photon veto		✓	✓
$\pi^+ \rightarrow \mu^+$ sequence	✓		✓
K^+ beam requirement	✓	✓	
Delayed coincidence		✓	

Table 4. The cuts in Pass 2 for selecting the data streams. The Skim 1 or 4 portion, the Skim 2 or 5 portion and the Skim 3 or 6 portion are used for studying the $K_{\pi 2}$ background, the $K_{\mu 2}$ background and the beam background, respectively. See text for more details.

3.6 Selection Criteria of Post Pass 1 and Pass 2

More selection criteria are designed and applied in order to gain more background reduction. According to their characteristics, the selection criteria are classified into four categories: single K^+ beam selection criteria, kinematic reconstruction, π^+ identification and photon veto. All the cuts are performed to optimize the background rejection and the signal acceptance. Data samples used for this study come from either the one-third data (from Skim 4 to Skim 6) or the monitor trigger events defined in Section 2.8.3, depending on the natures of selection criteria that are studied.

3.6.1 Single K^+ Beam Requirements

The cuts ensuring a single K^+ beam are also called as the “PS” cuts, since they mainly deal with the extra particles scattering either along the beam instrument or in the target. To study the characteristics of various beam background, the $Km2$ monitor and the Beam π^+ monitor are chosen as the acceptance and rejection sample, respectively. These PS cuts make full use of time measurements from various sub-detectors, energy loss measurement and pattern recognition information in both the B4 and the target as detailed below.

Beam Times

Timing measurements like t_{C_K} , t_{C_π} and t_{BW} , t_{BM} provided by the C_K , C_π , BWPC and B4 are used to reject extra beam particles scattering in the target when one of them agrees with the track time t_{rs} within ± 2 ns. Since the incoming K^+ beam intensity was high and could cause a TDC pile-up, the above time comparison also uses the CCD information from the C_K , C_π and B4 hodoscope. Figure 25 show the single K^+ beam signal indicated by the $Km2$ monitor and the beam background other than the $K_{\mu 2}$ or $K_{\pi 2}$ peak events rejected in the $pn n1$ or $pn n2$ momentum distribution.

Energy Loss in B4

The dE/dx cut tuning uses the acceptance sample from the $Km2$ monitor and the rejection sample from the beam π^+ monitor with no requirement on any B4 hodoscope measurement. This cut requires that the energy deposit by an incoming beam particle should be consistent with a K^+ . In E949, the K^+ velocity is about $0.57c$ slower than the π^+ ($0.97c$)[53], resulting in more K^+ energy deposit than the π^+ in the B4 hodoscope as shown in Figure 26. K^+ beam events are required to have a energy loss in B4 greater than 1.1 MeV.

Delayed Coincidence

The acceptance samples are taken from the $K_{\mu 2}$ peak events in the $Km2$ monitor, while the rejection sample is from the Skim 6 sample. The delayed coincidence cut requires $t_\pi - t_K > 2$ ns. As shown in Figure 27, the distribution of $t_\pi - t_K$ for K^+ decays at rest shows an exponential curve as expected with a lifetime of 12 ns. The distribution for the scattered π^+ 's or K^+ 's decaying in flight, on the contrary, shows a prompt peak around 0 ns. Since the accuracy of time measurement in target can give impact on the values of $t_\pi - t_K$, this cut will be tightened up to 6 ns when the uncertainty of timing measurement is large.

Beam Likelihood

The K^+ beam, which come to rest in the target, should have a good match among the energy deposits in the B4 hodoscope (B4 dE/dx), the energy deposits in the target and the stopping z positions related to the K^+ path length. Unlike a stopped K^+ , the single beam background with a scattered π^+ or a decay-in-flight K^+ does not have usual stopping z position definition in target. What the target reconstruction gives is very likely to be the position where the scattering or the decay-in-flight takes place. As a result,

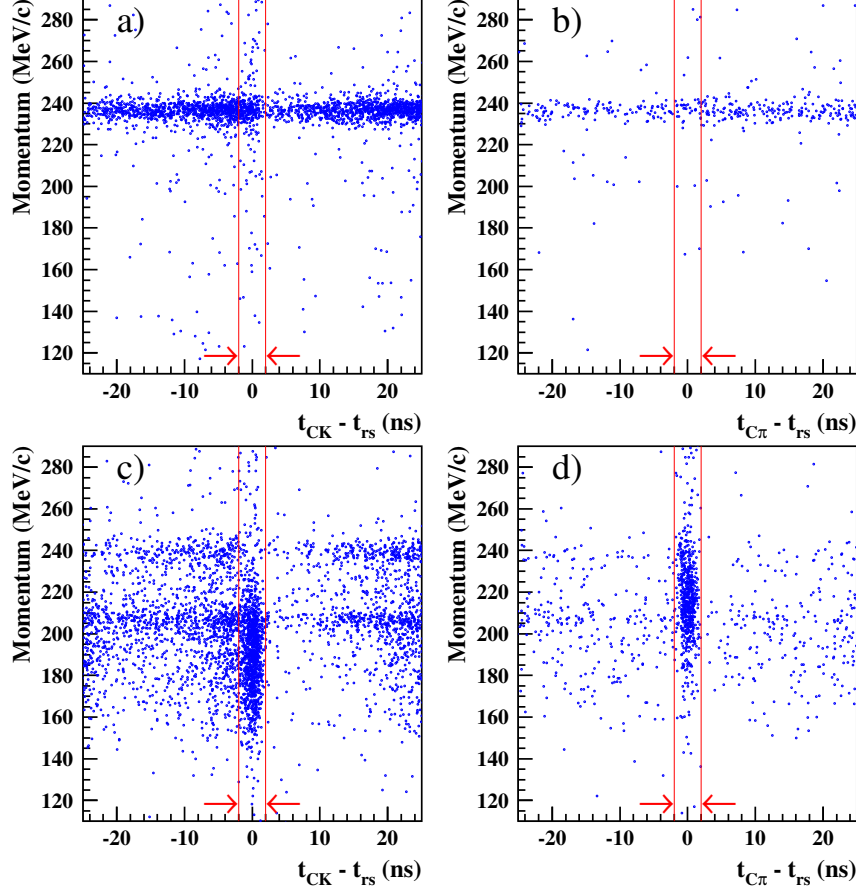


Fig. 25. The momentum of charged particle versus the TDC time given by the C_K and C_π relative to the track time t_{rs} . The $Km2$ monitor is used for representing the single K^+ beam events as shown in a) and b). The corresponding plots for those presented in the $pnn1$ or $pnn2$ trigger are also shown in c) and d). The arrows indicate the rejected timing regions with beam background contamination. The statistics in these plots for $pnn1$ or $pnn2$ trigger only accounts for about 0.1% of total K^+ flux.

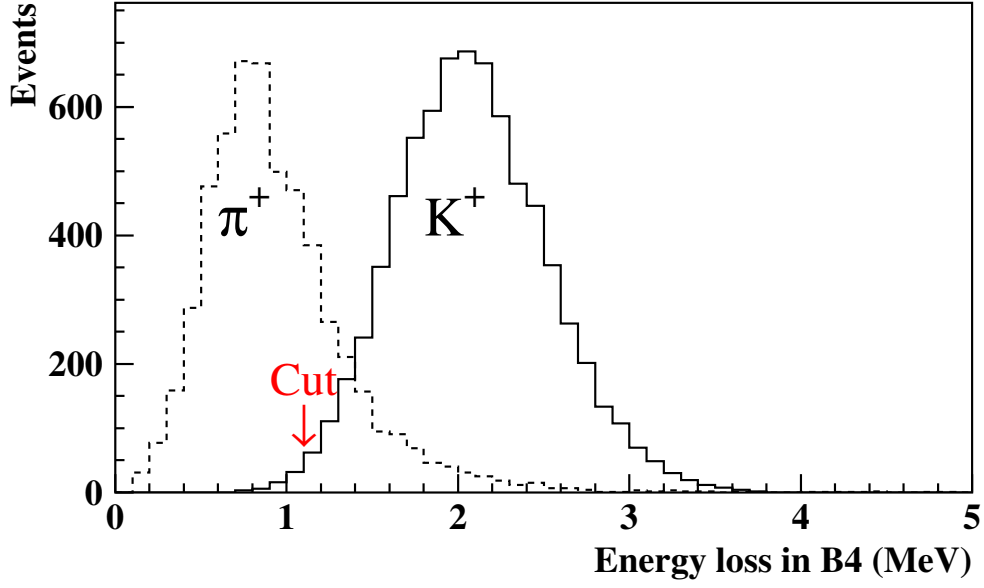


Fig. 26. The energy loss in the B4 hodoscope for K^+ beam (solid) and π^+ beam (dashed). The K^+ 's are from $Km2$ monitor trigger data, while the π^+ 's are from the selected π^+ beam events in the $pnn1$ trigger data. The arrow indicates the cut position.

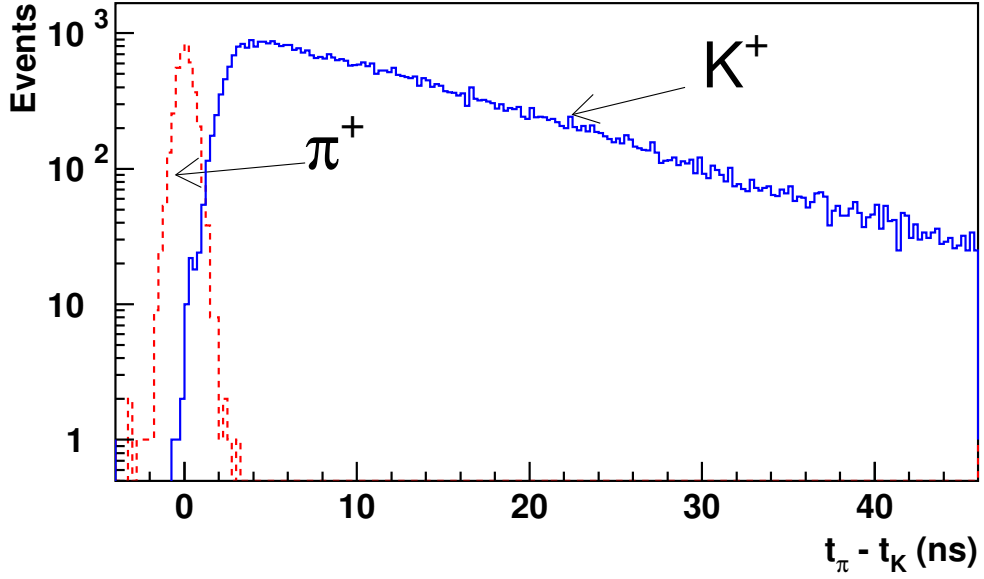


Fig. 27. Distribution of the time difference, $t_\pi - t_K$, for decay-at-rest K^+ (solid) from the $Km2$ monitor and the scattered π^+ (dashed) events from the Skim 6 sample.

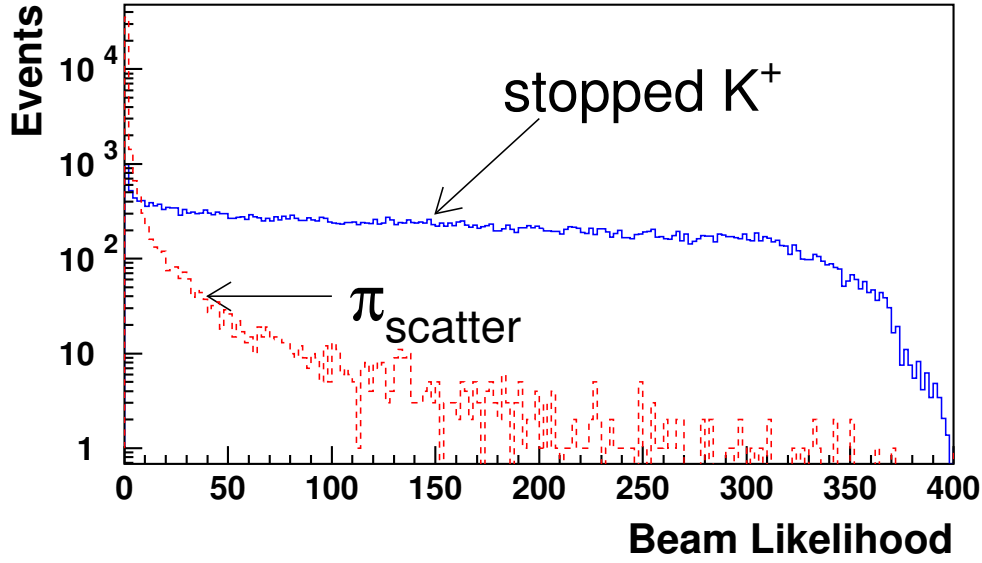


Fig. 28. Beam likelihood for K^+ decays at rest (solid) from the $Km2$ monitor and the Beam π^+ monitor (dashed) from the beam pion monitor. To have a reliable likelihood, the energy deposit in the target is required to be greater 25 MeV and, the number of K^+ fibers is required to be greater than 2.

the corresponding path length will disagree with the energy loss for a normal K^+ stop in the target. A best way to fully exploit these distinguishing features is to combine all the three quantities in a likelihood function. The signal sample used in the calculation is from the $K_{\mu 2}$ peak events in the $Km2$ monitor. Figure 28 show the likelihood distributions for signal, background and the cut position as well.

Pathology Cuts

In the target scintillator volume, charged particles and photons can either undergo nuclear interactions or have electromagnetic showers, complicating the target pattern recognition. Consequently, there may be some unknown mechanisms which can lead to background events into the signal region. An effective way to prevent this is to inspect the background events that show up outside the signal region to be described in Section 3.7.8. This can still help one to spot some specific features in either the K^+ cluster or the π^+ cluster or the other isolated hit fibers or the IC hit. Once a suspected background mechanism is observed, one has to use some cuts to enhance this type of background so that a dedicated cut can be designed to minimize the chance with a loop hole in the analysis. Exploiting these features gives a number of so-called “pathology cuts”. Despite of possible smaller rejection for individual cut, all together can help one to gain further rejection to the backgrounds. Below are the major situations addressed by the pathology cuts.

- Target π^+ cluster with an indentified kink. This is an indication of a hard scattering process, which may lead to a wrong measurement on kinematic quantities.
- B4 ADC/TDC energy/time inconsistent with the CCD energy/time within 1.5 MeV and 2 ns, respectively. Large deviation usually indicates an incident double beam background.
- Target π^+ fiber next to the decay vertex with energy greater than 3.5 MeV. This may indicate an actual K^+ fiber being mis-identified as a π^+ fiber, causing a wrong measurement on kinematic quantities.

- Target π^+ fiber with energy greater than 5 MeV. This may imply a $K_{\pi 2}$ or a radiative $K_{\mu 2}$ event with a photon hiding in the π^+ fiber.
- Target K^+ fiber found near the IC in coincidence with the IC TD time within ± 3 ns. This is often an indication of a double beam background registered by the IC other than the target.
- Target fiber in the opposite side of the π^+ cluster with respect to the vertex having energy greater than 2 MeV and time consistent with the t_π within ± 3.0 ns as well. This usually indicates a $K_{\pi 2}$ event with a π^0 in the opposite side of the π^+ .
- Target π^+ cluster having a back-to-back track feature with respect to the K^+ decay vertex. This usually indicates a double beam or a cosmic ray background screwed up with the first K^+ beam.
- Target edge fiber having energy greater than 5 MeV and time consistent with the t_{rs} within ± 4 ns of the track time. This can reject either an event with photon activities in the edge fibers, or a double beam event with the second beam hiding in the track.
- Any activity found in either the UPV or RV in time consistent with the t_{rs} within ± 4 ns.

Most of the pathology cuts are found to be related to the target pattern recognition. Any improvement on this will give a better rejection to the pathology type of background, which usually cannot be tagged in the usual procedure of background analysis until being proceeded down to the outside-of-the box study.

3.6.2 Decay π^+ Kinematic Requirements

The π^+ kinematic reconstruction gave range-, energy- and momentum-related measurements. All the relevant cuts are put into one category and called the “KIN” cuts. According to the nature of the kinematic aspects, one can split the KIN cuts into several sub-groups as described below.

Fiducial Cuts

The π^+ stopping layer is required to be between the 11th and 18th RS layers. No charged track is allowed to stop in the RSSC layer embedded between the 14th and the 15th RS layer. Events are rejected if the stopping layer is 14th with a RSSC hit found in the same RS sector or one sector clockwise of the stopping counter. The cosine of polar angle for a charged track is required to be within ± 0.5 . The track must stop inside the RS fiducial volume. The z position from the UTC track extrapolation to each RS layer is required to be as narrow as ± 30 cm to reject the $K_{\mu 2}$ background with longer path length in RS. To ensure a good UTC measurement, charged tracks should also be inside the effective UTC fiducial volume, which is defined as ± 25 cm along the center of z position at the UTC outer most layer.

Signal Phase Space

The phase space cuts require that the momentum, kinetic energy and range should be in the following regions: $211 \leq P \leq 229$ MeV/c, $115 \leq E \leq 135$ MeV, $33 \leq R \leq 40$ cm. Since any systematic shift can lead to either the $K_{\pi 2}$ or the $K_{\mu 2}$ background migrating into the signal region, the resolutions of kinematic valuables are first checked. It is observed that these resolutions are somewhat correlated to the direction of the charged track. To reduce this effect, the phase space cut are also defined according to the following conditions: $Pdev = \Delta P / \sigma_P \geq 2.5$, $Edev = \Delta E / \sigma_E \geq 2.5$, $Rdev = \Delta R / \sigma_R \geq 2.75$. Where the ΔP , ΔE and ΔR are the deviation from the $K_{\pi 2}$ kinematic peak positions. The σ_P , σ_E and σ_R are the corresponding resolutions, which are correlated to the azimuthal and polar angles.

Tracking Quality in UTC and RS

Charged tracks should be well reconstructed in both the $x - y$ and $r - z$ planes in UTC. An ideal event with a charged track can cause maximum 12 anode wire layer and 6 cathode foil hits. To ensure a good measurement requires at least 4 cathode foil hits. Further quality checks based on the $K_{\mu 2}$ monitor are performed with respect to the $K_{\mu 2}$ momentum peak, taking account of all the possible circumstances that can lead to a bad momentum measurement, such as no hit in the outermost of foil layer, or less than 12 layers of the anode wire hits, or tracks overlapping, or too many wire hits in a cluster being excluded in the fit, etc. The probability of track fit was tighten up to 0.1 in either the $x - y$ or the $r - z$ plane. The cuts were tuned so that the momentum resolution effect could not give significant contribution to the $K_{\pi 2}$ and μ^+ background estimates in Section 3.7.

Another good way to ensure a good UTC measurement is to have a matching check among UTC, RS and RSSC's. In $x - y$ plane, this can be achieved by checking the match between the UTC extrapolation and the positions of the sector crossing and the RSSC hits. Similarly, in the $r - z$ plane the check can be done between the UTC extrapolation and the z positions measured by RSSC and RS. In these checks the μ^+ 's in Skim 5 are selected with all the other cuts applied, except that the maximum momentum is not required and the $\pi^+ \rightarrow \mu^+ \rightarrow e^+$ decay sequence cuts (see Section 3.6.3) are also inverted. The π^+ 's in Skim 6 are selected with all the cuts applied, except that the cuts on single K^+ beam (see Section 3.6.1) are inverted.

Tracking Quality in Target

A good target tracking relies on the clearness of signal target pattern. This requires the track to be no more than 2 cm away from the B4 hit position to the nearest target K^+ fiber. The K^+ decay vertex should be in the nearest to the extreme tip of the K^+ cluster. No more than one fiber gap is allowed either between the K^+ decay vertex and the closest π^+ fiber.

A target track may include either π^+ fibers with photons or photon fibers mis-identified as the π^+ fibers, leading to a wrong energy measurement and even a wrong event classification if the photon veto also fails. The π^+ fibers are therefore examined using the likelihoods based on the comparisons of the time, energy, and distance to the track between the expected from the simulated $K^+ \rightarrow \pi^+ \nu \bar{\nu}$ sample and the measured from the $Kp21$ monitor.

Energy Loss in RS

It is noted that a μ^+ from the $K_{\mu 2}$ may become a background due to a particle being scattered. Also a π^+ from the $K_{\pi 2}$ may become a background due to either a photon or an accidental hit being hidden in the track counters. The resulting background can be removed by using the energy measurement in each RS layer to compare with the expected from the range.

The energy deviation is required to be within $\pm 4\sigma$'s for each RS counter as shown in Figure 29. In addition to each layer, a probability is also calculated with all track counters except for the T-counter, the stopping counter and the counters with sector crossing. As shown in Figure 30, the probability cut can provide a good separation between π^+ 's and μ^+ 's.

Another way to reject the μ^+ background is to calculate the likelihood from the energy ratio of track in the i -th layer: $\Delta E \equiv \log E_{\text{ext}}^i - \log E_{\text{meas}}^i$, in which the Landau tail energy can properly be taken into account. This calculation is done up to the layer prior to the stopping layer. As shown in Figure 31, a good π/μ separation is seen. It is noted that this cut on the likelihood is not fully but correlated with the cuts on the confidence level.

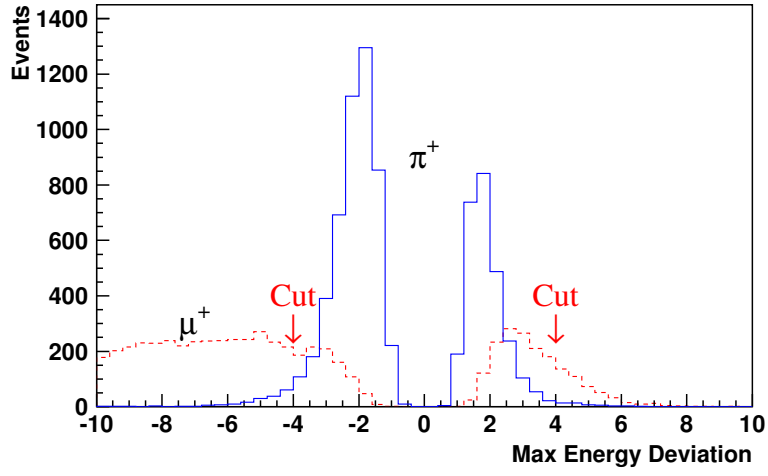


Fig. 29. Distributions of the maximum energy deviation for π^+ 's (solid) and μ^+ 's (dashed). The cut positions are indicated by the arrows.

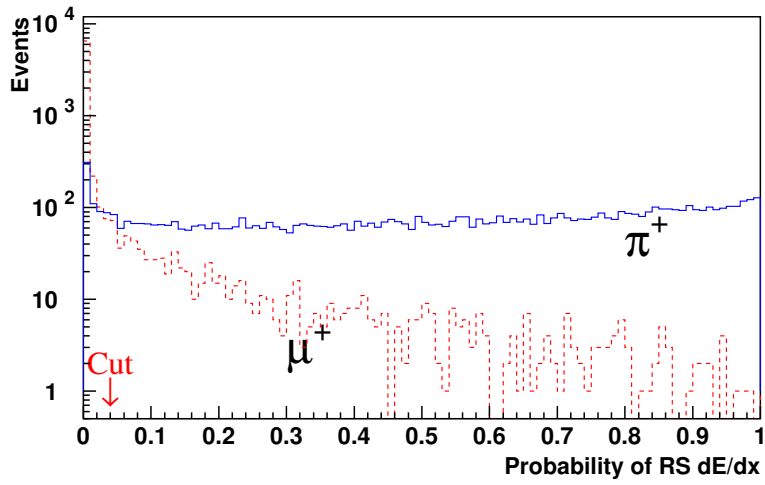


Fig. 30. Distributions of the probability in the RS dE/dx measurement for π^+ 's (solid) and μ^+ 's (dashed). The arrow indicates the cut position.

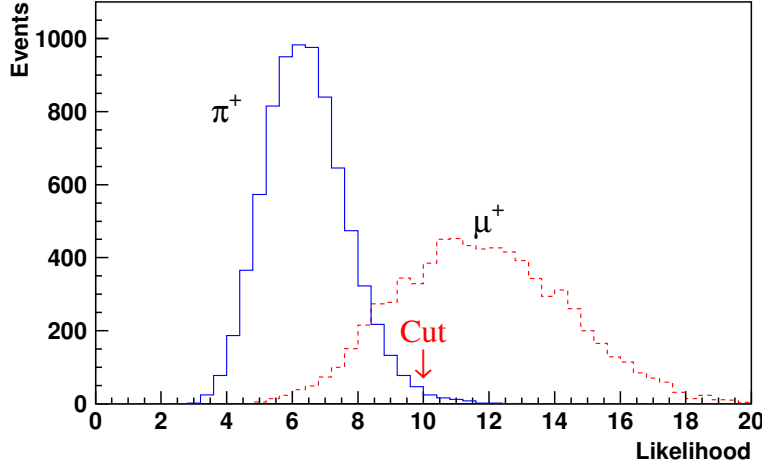


Fig. 31. Likelihood distributions of the RS energy measurement for π^+ 's (solid) and μ^+ 's (dashed). The arrow indicates the cut position.

Range-energy Consistency in IC and Target

Despite of poor energy measurements on IC and target, they can still provide a certain level of particle identification as that from the RS. Signal and background samples used in this study are from the $Kp21$ and $Km2$ monitors. The measured energy (δE_{IC}) minus the expected from the range in the IC is required to be between -5 to 1.75 MeV. The total measured target range (δR_{tg}) and energy (δE_{tg}) are used to cut events in which $\delta R_{tg} > 12$ cm or $\delta E_{tg} > 28$ MeV or $10.5\delta E_{tg} > 28\delta R_{tg}$ or $10\delta E_{tg} < 21.5(\delta R_{tg} - 2)$, since these events may have a photon hiding along the π^+ track in the target.

Range-momentum Consistency in UTC and RS

This cut is used to check whether the range of the charged track is consistent with that for a π^+ . The range deviation in RS is defined as $\chi_{rm} = (R_{meas} - R_{exp})/\sigma_R$, where R_{meas} is the measured range in RS, while R_{exp} is the expected range calculated from the momentum measured by the UTC with a π^+ hypothesis, and σ_R is the sigma of the measured range as a function of the momentum.

The background μ^+ 's and the signal π^+ 's are selected from Skim 5 and Skim 6 samples as used in the study of energy loss in the RS, except that the maximum momentum requirement is also applied in Skim 5 to remove the $K_{\mu 2}$ range tail events. The distributions of the range deviation for π^+ 's and μ^+ 's are shown in Figure 32. A good π/μ separation is observed.

3.6.3 $\pi^+ \rightarrow \mu^+ \rightarrow e^+$ Decay Sequence

The cuts for identifying the $\pi^+ \rightarrow \mu^+ \rightarrow e^+$ decay sequence were all put into a special group, called as the “TD” cuts, since the TD information records the pulse shape, providing a tool to recognize the the decay sequence. As can be seen below, the TD cuts, independent of the kinematic reconstruction and photon veto, are afforded by the observation of the $\pi^+ \rightarrow \mu^+ \rightarrow e^+$ decay sequence in the stopping counter. The signature for this decay sequence is as follows:

- Three energy deposits or pulses are found in the stopping counter corresponding to π^+ kinematic energy, $\pi^+ \rightarrow \mu^+ \nu_\mu$ decay (26.0 ns[7]) and $\mu^+ \rightarrow e^+ \nu_e \bar{\nu}_\mu$.
- The kinetic energy of the μ^+ from $\pi^+ \rightarrow \mu^+ \nu$ decay is 4.1 MeV, but due to saturation the observed energy is about 3.04 MeV[55]. The path length of a 4.1 MeV μ^+ is ~ 1.4 mm and the fraction of

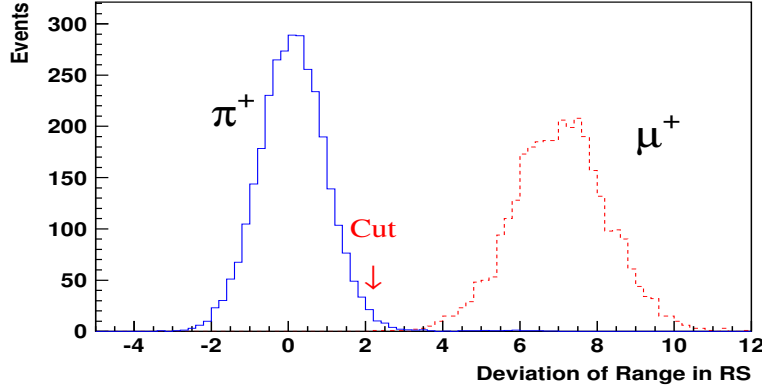


Fig. 32. Distributions of the range deviation in the RS for π^+ 's (solid) μ^+ 's (dashed) tracks. The arrow indicates the cut position.

μ^+ exits the stopping counter without depositing more than 1 MeV is only $\sim 1\%$ of π^+ decays.

- The e^+ from $\mu^+ \rightarrow e^+ \nu_e \bar{\nu}_\mu$ decay has a kinetic energy of $E < 53$ MeV. Most of the e^+ 's exit the stopping counter and deposit energy in the other RS counters.

The three energy deposits from the $\pi^+ \rightarrow \mu^+ \rightarrow e^+$ decay sequence should be observed by the TDs and TDCs at both ends of the stopping counter. Figure 33 shows the time development of the activity in and around the stopping counter when all the activity occurs within the TD gate of $(-0.5, 2.0)\mu\text{s}$.

For the μ^+ background, only two pulses from the $\mu^+ \rightarrow e^+$ decay are produced. A μ^+ can fake a π^+ when an extra pulse due to statistical fluctuation is detected in addition to the two pulses of $\mu^+ \rightarrow e^+$ decay. To suppress the μ^+ background, two stages of cuts are imposed.

In the first stage evidence for the $\pi^+ \rightarrow \mu^+ \nu_\mu$ decay is sought. The pulse development in the stopping counter as recorded by the TDs is fitted with a single- and double-pulse hypothesis in an interval of ~ 4 π^+ lifetimes (typically 104 ns). The template shapes used in the fit are derived from the average of measured pulses from μ^+ traversal for each end of each RS counter. In addition, a correction is applied to the template shape to take into account the change in shape due to propagation along the counter. The parameters of the single-pulse fit are the time, the total area of the pulse and a constant corresponding to a pedestal of typically 3 TD counts. The parameters of the double-pulse fit are the time of the first pulse, the time difference of the two pulses, the total pulse area, the fractional area of the second pulse and the pedestal. A fit to a triple-pulse hypothesis is attempted if evidence for a third pulse is found based on a rudimentary analysis of the TD information or if evidence for the $\pi^+ \rightarrow \mu^+ \nu_\mu$ decay from the double-pulse fit is lacking. The two additional parameters in the fit are the time difference of the third pulse with respect to the first and the fractional area of the third pulse. The results of the single- and double-pulse fit hypotheses for $\pi^+ \rightarrow \mu^+ \nu_\mu$ decay are shown in Figure 34.

At the first stage, loose requirements are applied on the observed μ^+ energy $1 < E_\mu < 14$ MeV and on the relative quality of the results of the single- and double-pulse fits, $r(u/s \text{ or } d/s) > 1$ and $r(u/s) \times r(d/s) > 1$ where the quantities are defined in Table 5.

At the second stage, a five cuts (Table 6) are applied to suppress the following four mechanisms when a $\mu^+ \rightarrow e^+$ decay can fake the three-pulse $\pi^+ \rightarrow \mu^+ \rightarrow e^+$ decay sequence.

1. π^+ time accidental: Accidental activity produces the first pulse, while the $\mu^+ \rightarrow e^+$ decay gives the second third pulses in timing sequence.

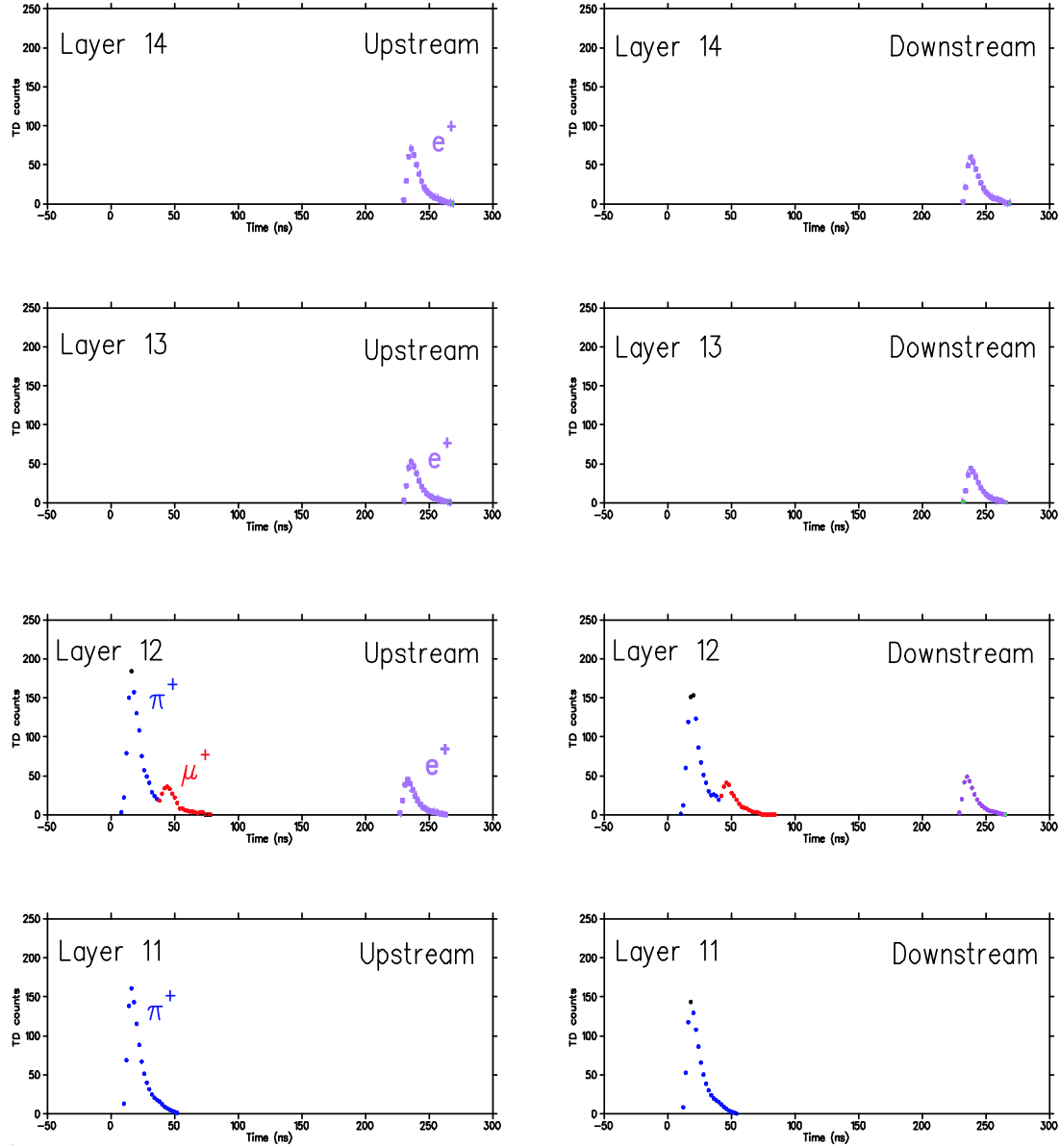


Fig. 33. The pulse height in 2 ns intervals in and around the stopping counter recorded by the TDs of the upstream and downstream ends of the RS counters. The π^+ enters from the inner layers, traversing layer 11 and stopping in layer 12. The $\pi^+ \rightarrow \mu^+ \rightarrow e^+$ decay sequence is observed in the stopping counter. The μ^+ from the $\pi^+ \rightarrow \mu^+ \nu_\mu$ decay is contained in the stopping counter. The activity due to the positron from the $\mu^+ \rightarrow e^+ \nu_e \bar{\nu}_\mu$ decay occurs in the stopping counter and layers 13 and 14.

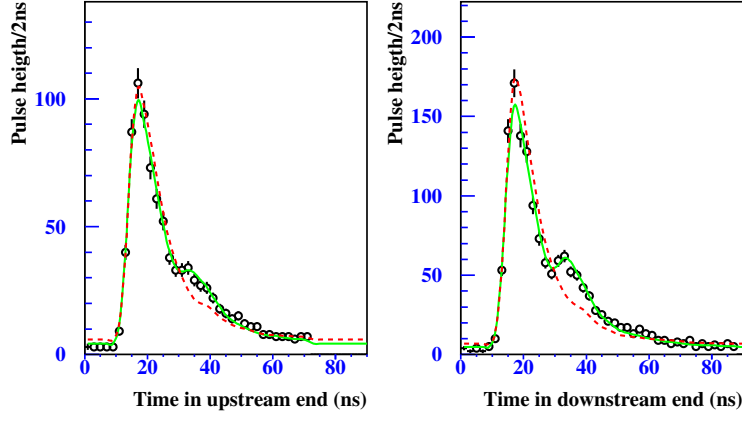


Fig. 34. Results of fits with the single- and double-pulse hypotheses to the TD pulse shapes in the stopping counter for $\pi^+ \rightarrow \mu^+ \nu_\mu$ decay. The fits to the TD pulse shapes are done for the downstream and upstream ends, separately. Data (open circles) from upstream end and downstream end of the stopping counter are fitted separately. The solid curve is for the double-pulse hypothesis and the dashed curve is for the single-pulse hypothesis.

Quantity	Definition or use
E_μ	Energy of the second pulse
T_μ	Time of the second pulse
$\chi_N^2(i)$	χ^2 for the N -pulse hypothesis for end i (i =upstream,downstream)
$r(i)$	$\chi_1^2(i)/\chi_2^2(i)$
$\log_{10}(r(u/s) \cdot r(d/s))$	neural net input
$\log_{10}(\chi_1^2(u/s) \cdot \chi_1^2(d/s))$	neural net input
dz	$= z_\pi - z_\mu$, neural net input component
dt	time difference between both ends for the second pulse, neural net input

Table 5. Definitions of quantities determined by the pulse-fitting in the stopping counter. The z positions are determined from the energy ratio between the two ends of the stopping counter. The z position of the nominal π and μ pulse is z_π or z_μ , respectively. The term “second” pulse identifies the μ^+ -candidate pulse. The neural net is described in the second stage of cuts.

Cut	π^+ time accidental	Early μ^+ decay	μ^+ time accidental	Tail fluctuation
π^+ time consistency Cut	✓			
$\mu^+ \rightarrow e^+$ decay requirement		✓		
Cut on μ^+ time accidental			✓	
Cut on μ^+ time accidental in the track counters			✓	
Neural net $\pi^+ \rightarrow \mu^+$ decay cut			✓	✓

Table 6. List of the backgrounds targeted by $\pi^+ \rightarrow \mu^+ \rightarrow e^+$ decay sequence cuts.

2. Early μ^+ decay: The $\mu^+ \rightarrow e^+$ decay occurs at an early time (≤ 100 ns), producing the first and second pulses, and accidental activity makes the third pulse.
3. μ^+ time accidental: The $\mu^+ \rightarrow e^+$ decay makes the first and third pulses, while accidental activity occurring between the time the μ^+ stops and when it decays produces the second pulse.
4. Tail fluctuation: Noise induced in the transport of the signal from the PMT to the TD, dubbed “tail fluctuation”, on the falling edge of μ^+ -induced pulse is identified as the second pulse. The decay positron from the μ^+ decay makes the third pulse.

π^+ Time Consistency Cut

This cut suppresses the π^+ time accidental background. When accidental activity makes the first pulse and a charged track makes the second pulse in the stopping counter, the timing of the first pulse obtained by the TD ($t_{\pi,TD}$) is not coincident with the track time (t_{RS}) obtained from the other RS counters along the track. Events are rejected if $|t_{\pi,TD} - t_{RS}| > 2.5$ ns.

$\mu^+ \rightarrow e^+$ Decay Requirement

This cut requires that the third pulse in the stopping counter should be consistent with a positron originating from the $\mu^+ \rightarrow e^+$ decay in the stopping counter. The positron from the $\mu^+ \rightarrow e^+$ decay generally deposits energy in the stopping counter and other neighboring counters as depicted in Figure 35. The positron finding starts by looking for a cluster of TDC hits in the RS counters in the region within ± 1 sectors and ± 2 layers of the stopping counter. The cluster is required to be adjacent to the stopping counter and to have hits in the same sector as the stopping counter. Candidates for the positron are found by requiring that the average time of the hits in the cluster is coincident (within ± 2.4 ns) with the TDC time in the stopping counter. The z positions of the hits in the cluster, obtained from the end-to-end time differences of the hits, are also required to be consistent with the z position in the stopping counter. If the coincident TDC hits are due to a track that passed through the stopping counter, then hits may be found on both sides of the stopping counter (Figure 35). The positron from the stopping counter can be determined by distinguishing between one-side and both-side tracks. The early μ^+ decay background is removed by requiring that the nominal μ^+ pulse from the TD pulse fitting is inconsistent with the time of the cluster.

Cut on μ^+ Time Accidental

Accidental activity in the stopping counter is frequently associated with activity in other RS counters as well as the BV, BVL and EC. Hence, events with activity coincident with the μ^+ time in the stopping

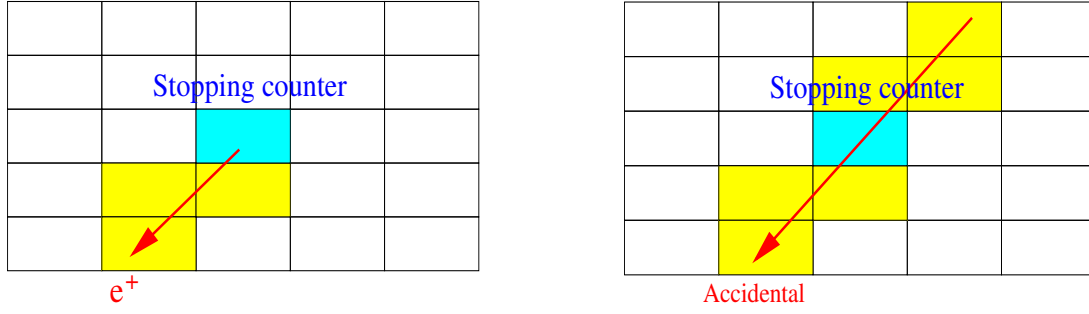


Fig. 35. Schematic view of signal (left) and background (right) of the $\mu^+ \rightarrow e^+$ decay. Each rectangle represents a RS counter. The central counter represents the stopping counter and the shaded rectangles represent hit counters. The arrow indicates the possible direction of the positron or charged track producing the hits.

counter are targeted for rejection. The time windows and energy thresholds for the various subsystems in RS, BV, BVL and EC are optimized in order to have the highest rejection power at a given acceptance value of 94% for this cut. Events are rejected if the energy sum of the hits within a time window in any of the subsystems is greater than the threshold.

Cut on μ^+ Time Accidental in the Track Counters

This cut rejects the μ^+ time accidental background by performing fits to a double-pulse hypothesis in the two RS counters along the track prior to the stopping counter. The purpose is to eliminate accidental activity that overlaps the charged track and makes a second pulse in the stopping counter. If the time of the fitted second pulse is within ± 5 ns of the μ^+ time in the stopping counter, the fitted energy of the second pulse is greater than 1 MeV and the χ^2 ratios of the single- to the double-pulse fit hypotheses, $r(i)$, are greater than four, then the event is rejected.

Neural Net $\pi^+ \rightarrow \mu^+$ Decay Cut

This cut targets the tail fluctuation background. Such fluctuations can mimic the energy deposit for a μ^+ on the falling edge of the π^+ -induced pulse. Tail fluctuations generally yield both a small time difference with respect to the first pulse and a low pulse area in the apparent second pulse. The variables shown in Figure 36 and described in Table 5 differ for events induced by $\pi^+ \rightarrow \mu^+ \nu_\mu$ and $\mu^+ \rightarrow e^+ \nu_e \bar{\nu}_\mu$ decay. Application of a fixed cut to each variable would cause a non-negligible acceptance loss. In order to achieve a higher acceptance at the same rejection as the fixed cuts, a Neural Network (NN) technique is adopted.

The NN function is derived via a Multi-Layer Perception (MLP) program incorporated in the library of Physics Analysis Workstation (PAW)[56]. To create the NN function, the π^+ scattering and $K_{\mu 2}$ range tail events in the $\pi \nu \bar{\nu}(1)$ trigger, which pass all other $\pi^+ \rightarrow \mu^+ \rightarrow e^+$ decay sequence cuts, are used as signal and background samples, respectively. A 5-variable NN function is obtained using the six variables shown in Figure 36 with the differences in z position and time combined to create a single input variable, $\chi^2(z, t) \equiv (dz/\sigma_{dz})^2 + (dt/\sigma_{dt})^2$, where σ_{dz} (σ_{dt}) is the resolution of the dz (dt) distribution. The distributions of the output of the NN function for π^+ s and μ^+ s are shown in Figure 37.

As an added benefit of the combination of variables in a single NN, the rejection as a function of acceptance can be easily obtained by changing the NN cut position as shown in Figure 38. The cut position at 0.76 in the output of the NN function is determined so that the acceptance of this cut is 85%.

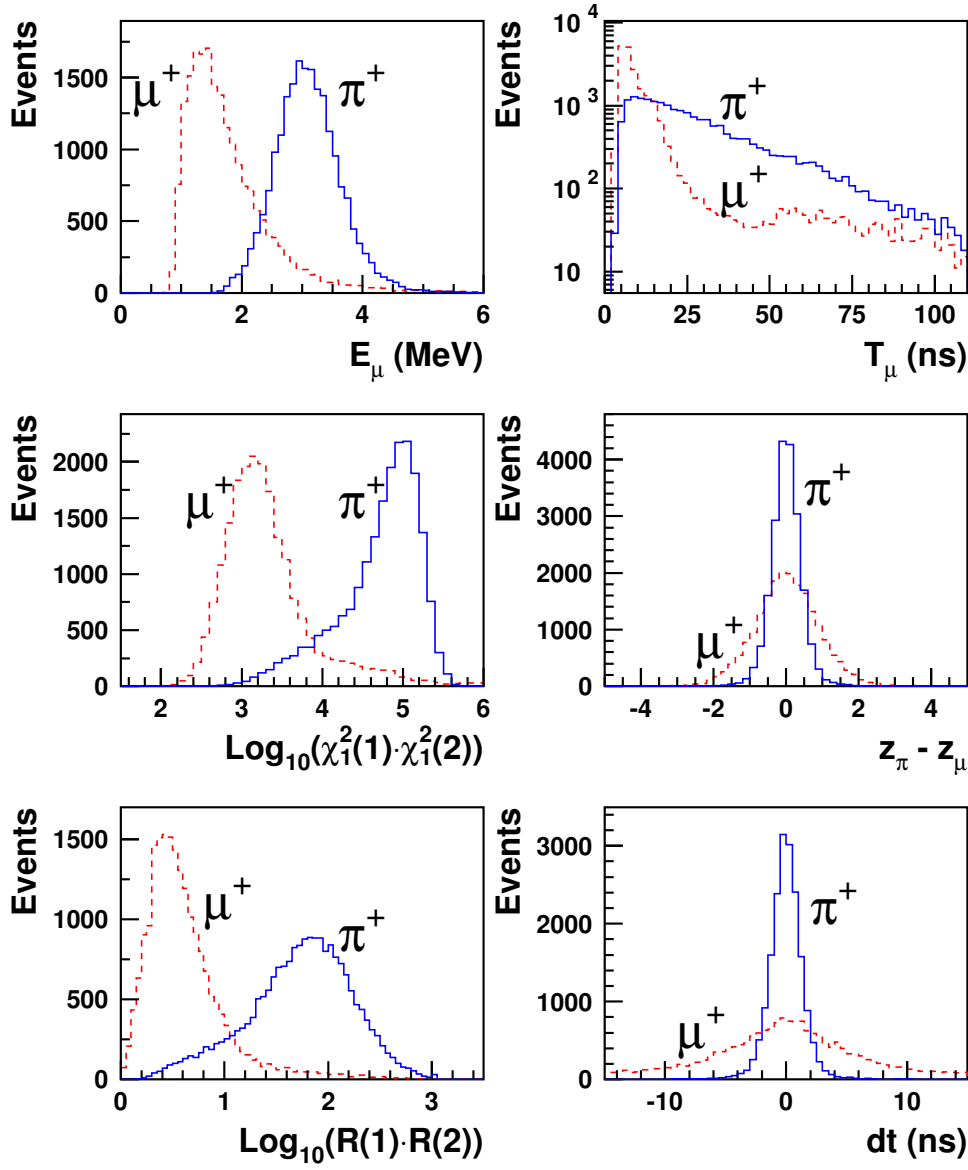


Fig. 36. Distributions of the input variables for the Neural Net function in $\pi^+ \rightarrow \mu^+ \nu_\mu$ induced (solid) and $\mu^+ \rightarrow e^+ \nu_e \bar{\nu}_\mu$ induced (dashed) decays. The energy of the second pulse (top left), time of the second pulse (top middle), log of the product of the χ^2 ratios of single- to double-pulse fits for both ends (top right), log of the product of the single-pulse fit χ^2 's for both ends (bottom left), z position difference between the first and second pulses obtained from the energy ratio of both ends (bottom middle), and time difference of the second pulses in both ends (bottom right).

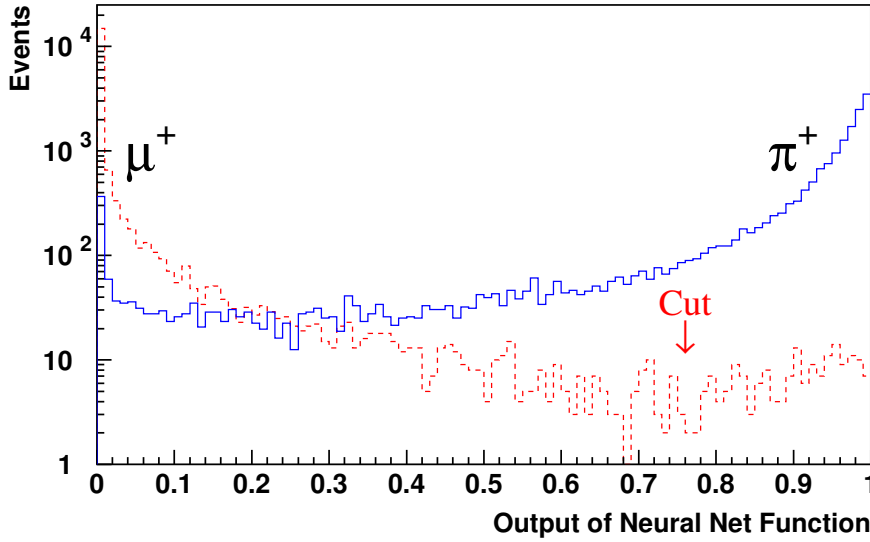


Fig. 37. Distributions of the outputs of the NN function for π^+ (dashed) and μ^+ (solid) events. Events with an output of the NN function less than 0.76 are rejected.

3.6.4 Photon Veto

As already stated previously, the total rejection for π^0 against backgrounds associated with photons is required to be in an order of 10^6 , including those from both online and offline. A rejection factor of 10^4 is already achieved by the online photon veto, leaving a further 10^2 rejection factor to be achieved by the offline analysis.

Search for the photons coincident with the track time is performed in the subsystems of BV, BVL, RS, EC, target, IC, VC, CO and MC. Timing resolution of each photon detection system is a key index to determine the time window of photon veto. Figure 39 shows the measurements of the timing resolution for each system as a function of the visible energy.

The time window and energy threshold in each category are optimized by changing their cut positions to achieve better acceptance and rejection. Rejection sample is from the Skim 4 with much more $K_{\pi 2}$ events in the $pnn1$ trigger, while the acceptance sample is from the $Km2$ monitor. To ensure the events are from the $K_{\pi 2}$ peak, the measured range, energy and momentum of the charged tracks should be within 3σ 's of the peaks. For the $K_{\mu 2}$, the range of track is required to be longer than 40 cm to get rid of any event which may contain photon(s).

The optimization process starts from the initial set of cut parameters, which are not required to be optimal. Every time a new set of parameters is introduced, the rejection and acceptance are re-measured with them. This sequence is performed for all the cut categories with a rule that when one category is perturbed, all the other categories are kept unchanged. If the rejection successfully increases without losing the acceptance or the acceptance increases without losing rejection, the set of parameters will be a good input for next iteration. More preferable case is that both rejection and acceptance improved. Figure 40 illustrate this tuning process for the photon veto. The optimization process continues until no more gain is obtained in the rejection without losing the acceptance. The boundary point is measured at every given acceptance position. As a result, a profile curve, which gives the most effective rejection, is obtained.

Figure 40 shows the rejection of the photon veto cuts against the $K_{\pi 2}$ background as a function of acceptance. The cut position for each category is determined so that the $K_{\pi 2}$ background is reasonably

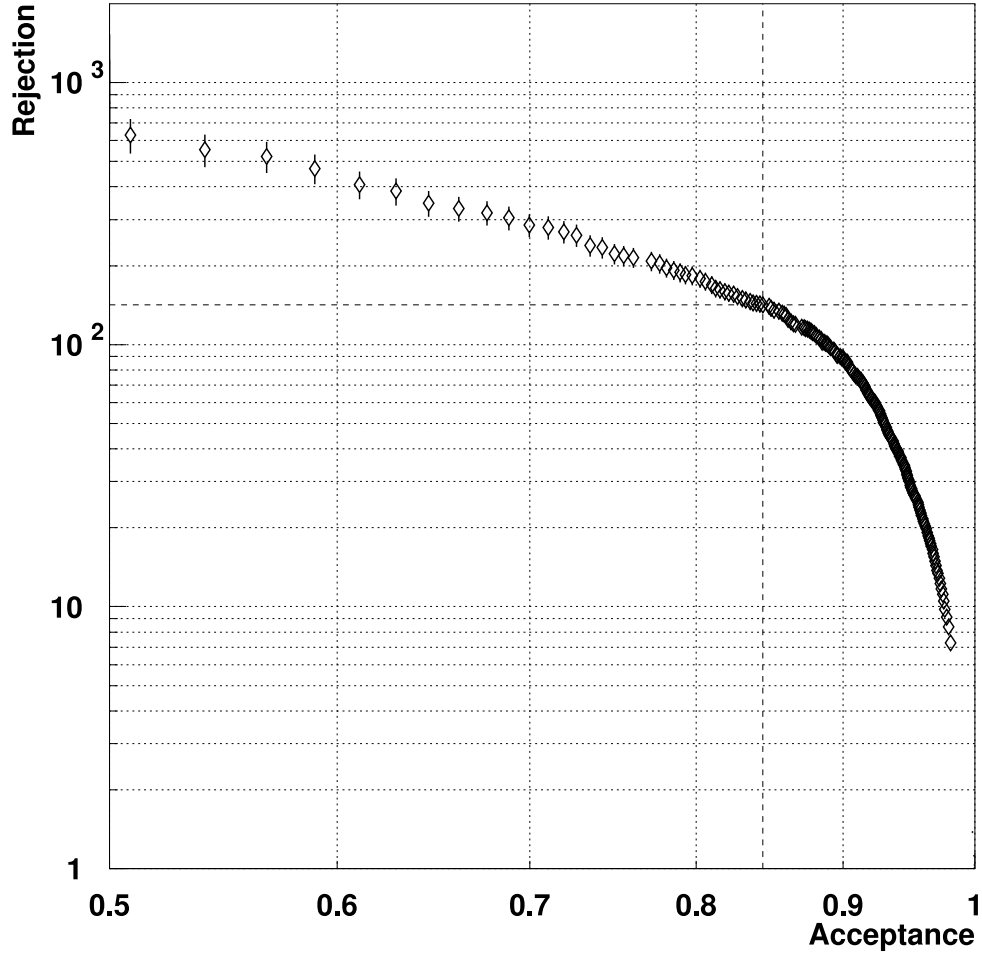


Fig. 38. Rejection of the Neural Net $\pi^+ \rightarrow \mu^+$ decay cut as a function of the acceptance. The intersection of the vertical and horizontal dashed lines shows the rejection and acceptance at the nominal cut position.

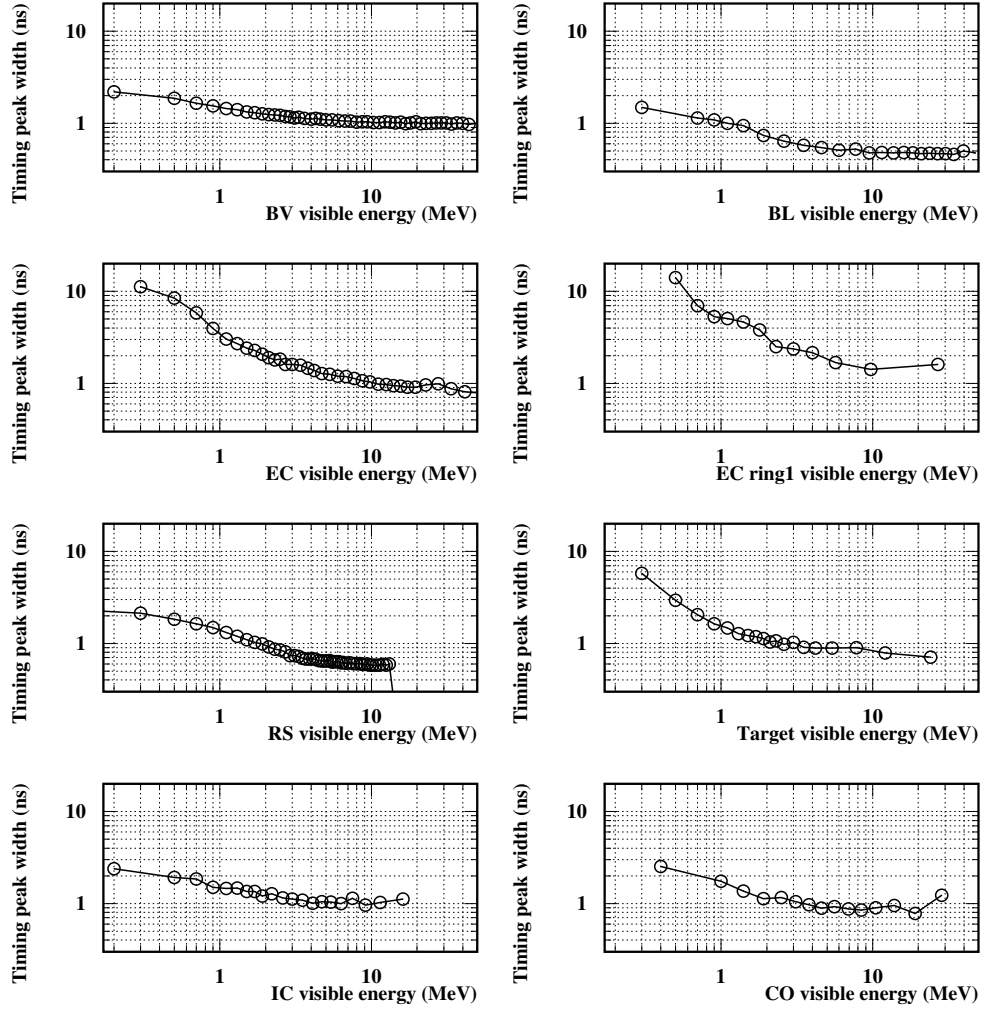


Fig. 39. The timing resolution as a function of visible energy in various photon detectors. Due to statistical shortage, the plots for the VC and MC are not available.

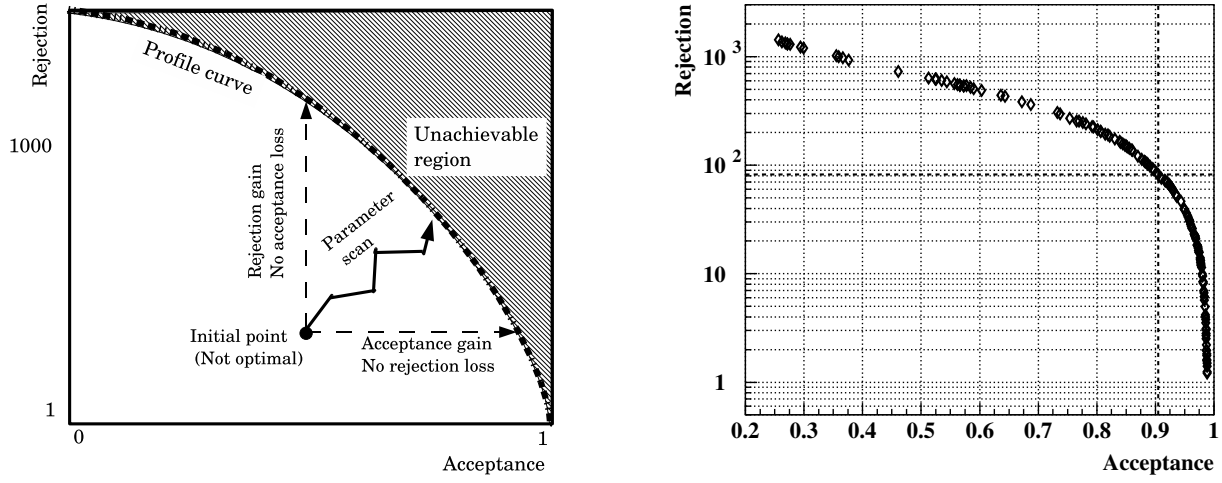


Fig. 40. Illustration of the optimization process to determine the photon veto parameters (left plot). Rejection of the photon veto cuts against the $K_{\pi 2}$ background as a function of the acceptance (right). The cross point of the vertical and horizontal lines shows the rejection and acceptance at the cut position.

suppressed in the background estimation. An acceptance of 90.5% and a rejection factor of 84.3 ± 1.2 are achieved using this set of cut positions. The time window and energy threshold for each category are tabulated in Table 7. The total offline photon veto is not a simple multiplication of all the rejections listed in Table 7 because of the correlations among them.

Category	Time window (ns)	Energy threshold (MeV)	Rejection
BV	± 4.50	0.20	14.556
BVL	± 2.00	0.00	1.247
RS	± 1.50	3.80	3.329
EC	± 2.25	3.80	2.296
Inner EC	± 1.75	1.00	1.186
Target	± 1.30	4.79	1.493
IC	± 2.25	0.40	1.321
VC	± 2.00	1.60	1.054
CO	± 1.25	0.80	1.052
MC	± 1.50	2.80	1.003

Table 7. Time window and offline energy threshold for each category of the photon veto cuts. Also listed are individual rejection contributed by each sub-system.

Bkg.	CUT1	CUT2	Sample	B	$(C + D)/C$	BC/D
$K_{\pi 2}$	PV	KIN	Skim 4	0.295 ± 0.092	85.2 ± 2.5	0.0035 ± 0.0011
$K_{\mu 2}$	TD	KIN	Skim 5	2.25 ± 0.58	$(4 \pm 1) \times 10^2$	0.0051 ± 0.0018
μ^+ band	TD	KIN	Skim 5	1.99 ± 0.47	$(4 \pm 1) \times 10^2$	0.0045 ± 0.0015
Single-beam	DC	B4	Skim 6	8	$(7 \pm 3) \times 10^3$	0.0011 ± 0.0007
$K^+ - K^+$	BWPC	B4	Skim 6	0.038 ± 0.028	117.0 ± 36.8	0.0003 ± 0.0003
$K^+ - \pi^+$	BWPC	B4	Skim 6	0.26 ± 0.11	$(7 \pm 4) \times 10^3$	< 0.0001

Table 8. Results of the bifurcation analyzes for the backgrounds in the one-third sample. All the results for the region B are from the second bifurcations except for the single-beam background due to the statistical reason in the measurement of normalization branch. Errors are statistical only. See text for more details.

3.7 Background Evaluation

The signal region was always masked until all the background evaluations were completed. As already stated in the previous section, the $pnn1$ trigger data are randomly divided into 1/3 and 2/3 portions for the cuts tuning and the final background estimates, respectively. As already described in Section 3.1, the stopped K^+ decay background and the beam background can be even categorized into more concrete ones for the merit of background study:

- $K_{\pi 2}$ background;
- $K_{\mu 2}$ range tail background;
- μ^+ band backgrounds;
- single beam background;
- $K^+ - K^+$ double beam background;
- $K^+ - \pi^+$ double beam background;
- CEX background.

All of them, except for the CEX background, are estimated using the real data by means of a bifurcation method. Table 8 gives the bifurcation cuts, the sample stream definitions and the results for the one-third $pnn1$ trigger data. This one-third analysis was done first, cuts were tuned and optimized, and the two-third analysis was used to give the final background evaluation. Since the normalization branch usually leaves no or only one event in region B , a second bifurcation analysis is performed in this branch to statistically give a better evaluation. Details are given in the following sections.

3.7.1 $K_{\pi 2}$ Background

The normal $K_{\pi 2}$ decay event has a charged track with a monochromatic momentum, range and energy plus two photons. When the photons escape from detection, the $K_{\pi 2}$ event can sneak into the signal region by a resolution effect.

The two bifurcation cuts are the phase space cut in the KIN cuts (CUT1) and the PV cuts (CUT2), since both of them can independently give a powerful rejection to the $K_{\pi 2}$ background. In order to remove the μ^+ and beam backgrounds (corresponding to the first row in Figure 23), the bifurcation analysis sample was selected from the Skim 4 sample by applying the TD cuts, the PS cuts and the KIN cuts except the phase space cuts,

In the normalization branch, the $K_{\pi 2}$ events with photon activities are selected by inverting the PV cuts ($\overline{\text{CUT1}}$). The phase space cuts in the KIN cut category, namely CUT2, are applied to the above selected $K_{\pi 2}$ sample, resulting in no event ($B = 0$) left in the normalization branch (corresponding to the second row in Figure 23).

In the rejection branch, the $K_{\pi 2}$ events with momentum, energy and range in the $K_{\pi 2}$ peak are selected by inverting the phase space cuts in the KIN cut category ($\overline{\text{CUT2}}$), giving 95797 events for the region $C + D$. The PV cuts (CUT1) are then applied to the remaining $K_{\pi 2}$ events, leaving 1124 events for the region C (corresponding to the third row in Figure 23).

Obviously, using the results given above will give rise to a large statistical uncertainty in $K_{\pi 2}$ background estimate, since the phase space cuts in the KIN cut category rejects all the $K_{\pi 2}$ events in this Skim 4 sample. Another approach to estimate the number of events in the normalization branch is to conduct the second bifurcation analysis, which separates the phase space cuts on the low boundary into E cut and RP cut, since the E measurement is almost independent of the R and P measurements. The E cut and the RP cut are treated as new CUT1 and CUT2 in the second bifurcation analysis and then are applied sequentially to the selected $K_{\pi 2}$ sample in the normalization branch.

Changing the cut positions on the $Rdev$, $Pdev$ and $Edev$ gives the number of events in the normalization branch (N_{RP}) and the rejection branch (REJ_E), which are then used to calculate the expected number of events in the normalization branch by means of $B = N_{RP}/(R_E - 1)$. This second bifurcation method gives smaller uncertainty, providing a way to optimize the phase space cut positions to reject the $K_{\pi 2}$ background with less acceptance loss.

The second bifurcation is performed from the cut positions: $Rdev > 1.70$, $Edev > 1.45$ and $Pdev > 1.45$. The expected number of events at these cut positions is compared to the observed from the first bifurcation analysis and is observed to be about 10% less than the observed. This is due to some level of correlation between the range and energy measurements in the stopping layer.

Figure 41 shows the expected $K_{\pi 2}$ background from the first bifurcation and the second bifurcation in the one-third normalization branch as a function of the $Edev$ cut position. Both are consistent except that the first bifurcation run out of the statistics when extending to the signal region. The acceptance is measured using the simulated $K^+ \rightarrow \pi^+ \nu \bar{\nu}$ sample.

The expected number of events from the second bifurcation is used to give the result for the normalization branch, which is then used to give the estimated background level for the one-third sample as shown in Table 8.

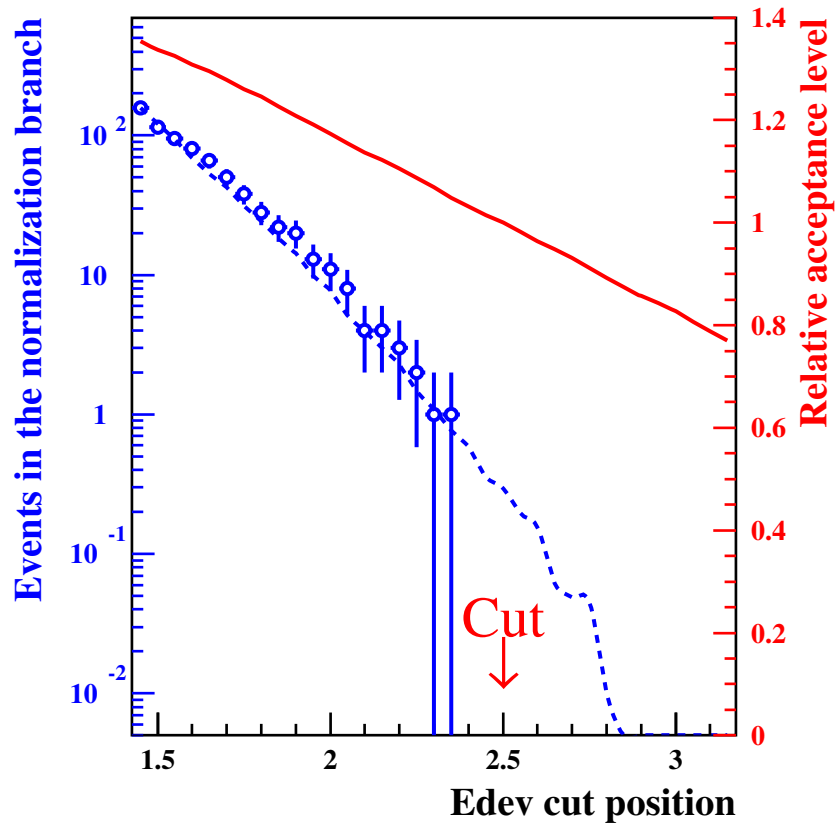


Fig. 41. The expected K_{π^2} background from the first bifurcation (open circles) and the second bifurcation (dashed curves) in the one-third normalization branch as a function of the E_{dev} cut position. Also shown is the relative acceptance change as the E_{dev} cut position (solid curve). The arrow indicates the cut position.

3.7.2 μ^+ Background

The μ^+ background consists of the $K_{\mu 2}$ range tail events and the μ^+ band events as indicated in Figure 19. All of these μ^+ 's lose energy and eventually come to rest in RS. Both of them can migrate into the signal region through a resolution effect if the TD cuts fail.

The two bifurcation cuts with the most powerful rejection are chosen from the RS dE/dx cuts in the KIN cut category and the TD cuts. The μ^+ background sample is selected from the Skim 5 sample by applying the PV cuts and the PS cuts, in order to remove the $K_{\pi 2}$ and beam backgrounds (corresponding to the first row in Figure 23).

In the normalization branch, the μ^+ events are obtained by inverting the TD cuts ($\overline{\text{CUT1}}$). The KIN cuts (CUT2) are applied to the above selected μ^+ sample, leaving only one event ($B = 1$) in the normalization branch (corresponding to the second row in Figure 23).

In the rejection branch, the μ^+ events are selected by inverting the RS dE/dx cuts in the KIN cut category ($\overline{\text{CUT2}}$), getting 7119 events for the region $C + D$. The TD cuts (CUT1) are applied to the μ^+ events, leaving 16 events in the region C (corresponding to the third row in Figure 23).

The result from the bifurcation analysis has large statistical uncertainty, since only one event remain in the normalization branch. The $K_{\mu 2}$ range tail and the μ^+ band events are the only two possible μ^+ backgrounds in the signal region. These two backgrounds are due to the momentum and the range resolution effects. Once these resolution effects can be know precisely in the signal region, one can also get a better estimate of corresponding events B in the normalization branch. In this analysis, the events with momentum greater than 225 MeV/c are regarded as the $K_{\mu 2}$ range tail background.

The momentum resolution effect can be well described by using a template momentum distribution from the $K_{\mu 2}$ range peak events. In the study of the normalization branch, the RS dE/dx cuts are removed from the KIN cuts. Also removed are the upper boundary cuts on the range, energy and momentum. The $K_{\mu 2}$ range peak events are selected by requiring the range to be greater than 50 cm. The selected $K_{\mu 2}$ peak events in the *pnn1* trigger are found to have longer ranges in the target, leading to a bias of 0.5 MeV/c higher momentum measurement when applying a pion hypothesis to the contribution from the energy loss in the target. After subtracting this bias for each $K_{\mu 2}$ peak event, the momentum distribution was seen in good agreement with that from the $K_{\mu 2}$ range tail events and with more statistics in the signal region defined below 229 MeV/c. Normalizing the number of $K_{\mu 2}$ range peak events to that of the $K_{\mu 2}$ range tail events gives the expected number of events B in the normalization branch as shown in Figure 42. The estimated background level is given in Table 8.

Enhancing the range-momentum resolution effect can be achieved by removing the PV cuts and the RS dE/dx cuts in the normalization branch sample. This is due to the fact that the range and momentum measurement are independent of the energy measurement except for that in the stopping counter. The RS dE/dx cuts should not change the range-momentum distribution even if there are accidental hits or photon activities in the RS. Within the statistical uncertainty, both distributions were seen to be consistent except that the one without both the PV cuts and the RS dE/dx cuts can give eight times more statistics. This distribution can give an estimate of events with higher statistics in the normalization branch (see Figure 43). The estimated background level for the μ^+ band is given in Table 8.

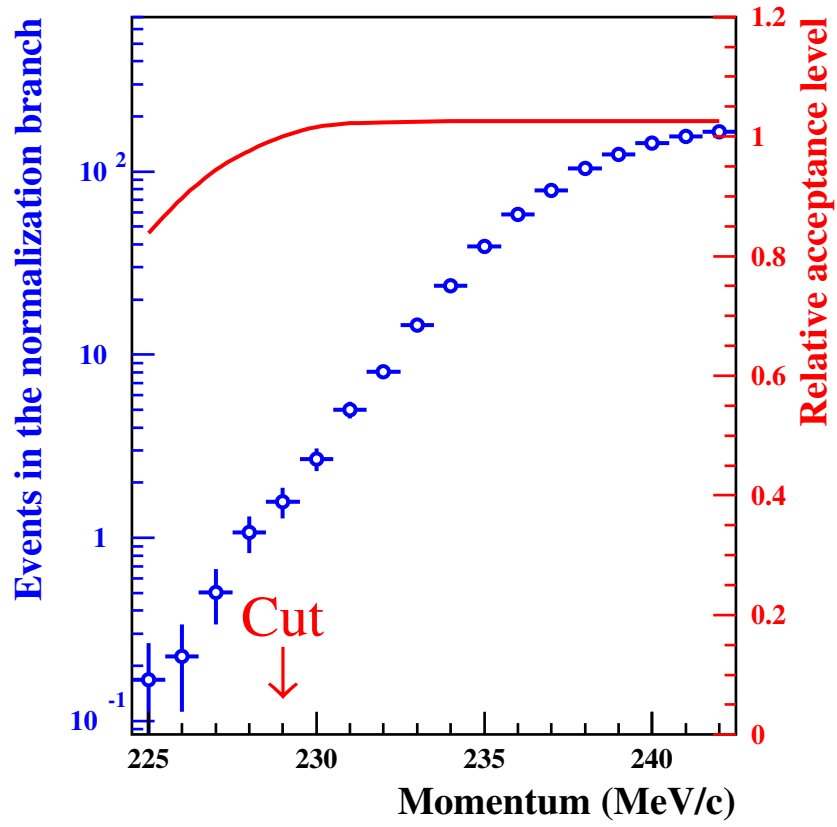


Fig. 42. The expected $K_{\mu 2}$ range tail background (open circles) in the one-third normalization branch as a function of the momentum cut. The relative acceptance change is also shown. The arrow indicates the cut position. See text for more details.

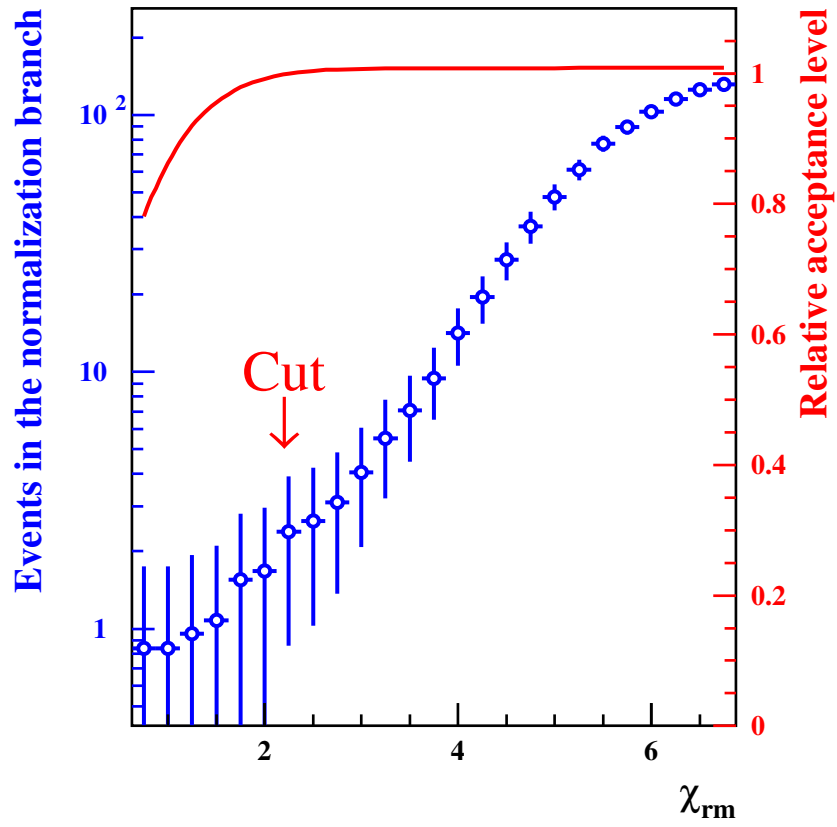


Fig. 43. The expected μ^+ band background (open circles) in the one-third normalization branch as a function of the momentum cut. The arrow indicates the cut position. The relative acceptance change is also shown. See text for more details.

3.7.3 Single Beam Background

The single beam background events are defined as either the beam π^+ 's scattering or the beam K^+ 's decaying in flight between the Čerenkov counter and target. The two bifurcation cuts chosen are the delayed coincidence (DC) cuts and the B4 energy loss cut. The events are selected from the Skim 6 sample by applying the PV cuts, the KIN cuts, the TD cuts, and the PS cuts except for the DC cuts and the B4 energy loss cut (corresponding to the first row in Figure 23).

In the normalization branch, the single beam events are selected by inverting the DC cuts ($\overline{\text{CUT1}}$). The B4 energy loss cut (CUT2) are applied to the above selected single sample, leaving 8 events in the region B for the normalization branch (corresponding to the second row in Figure 23).

In the rejection branch, the single beam events are selected by inverting the B4 energy loss cut ($\overline{\text{CUT2}}$), leaving 29100 events for the region $C + D$. The DC cuts (CUT1) are applied to these selected events, getting 4 events in the region C (corresponding to the third row in Figure 23). The rejection is applied for both the π^+ scattering events and the K^+ decay-in-flight events, since there is no reason to have the different rejections for them. It is noted that the probability for the second case is much smaller than the first case.

The background estimate for the single beam background is given in Table 8.

3.7.4 Double Beam Background

The double beam events are the same as the single beam event, except that an earlier K^+ exists and fooling the DC condition cuts. These backgrounds include those with extra K^+ 's or π^+ 's in addition to the K^+ 's that come at first. When both beam particles are K^+ 's, this event is called as a $K^+ - K^+$ event. When the π^+ comes after the studied K^+ , this event is called as a $K^+ - \pi^+$ event.

Because of the time difference between these two beam particles, the timings used in the DC cuts are not the usual meaning of $t_{\pi^+} - t_{K^+}$, and cannot be used to remove the double beam background. One way to reject this background is to use the timing of each beam particle registered by the beam instrumentation, including the C_K and C_π , BWPCs and B4, since the second beam particle is the source of the π^+ track. Another independent way is to use the target pattern recognition to find out the extra particles other than the initial K^+ hit.

The two bifurcation cuts chosen are the BWPC timing cuts and the B4 timing cuts. The events are selected from the Skim 6 sample by applying the PV cuts, the KIN cuts, the TD cuts and the PS cuts except for the BWPC and the B4 timing cuts. These cuts remove the $K_{\pi 2}$, μ^+ and single beam backgrounds. (corresponding to the first row in Figure 23).

In the normalization branch, there is no event left over if the B4 timing cuts (CUT2) are applied. In order to give a more precise estimate, the second bifurcation is adopted. time measurements including the trailing edge TDC time from the C_K and C_π are used to select the $K^+ - K^+$ events and $K^+ - \pi^+$, separately. The bifurcation analyzes are then performed between the B4 timing cuts and the target pattern recognition. Results are given in Table 8.

In the rejection branch, the double beam background events are selected by inverting the B4 timing cuts ($\overline{\text{CUT2}}$). The $K^+ - K^+$ and $K^+ - \pi^+$ events are tagged by requiring the C_K and C_π , separately; this resulted in 1170 and 22150 events for both cases. Applying the BWPC timing cuts (CUT1) results in 10 and 3 events observed for the $K^+ - K^+$ and $K^+ - \pi^+$ backgrounds, respectively. The resulting rejections are given in Table 8.

The background estimate for the double beam background is given in Table 8. The $K^+ - K^+$ background dominates the two beam background.

3.7.5 Charge Exchange Background

Since there is no reliable way to isolate the CEX events from the $pnn1$ trigger data, the background study relied on Monte Carlo simulation. A proper CEX simulation needs inputs for regeneration location,

and K_L^0 momenta, etc. Since a K^0 almost equally go to K_L^0 and K_S^0 . A special CEX trigger was designed to tag events with two charged tracks from the K_S^0 decay to $\pi^+\pi^-$. The K_S^0 's are reconstructed in the two-pion invariant mass and then used to measure the K_S^0 production rate, momentum spectrum, decay vertex distribution, and pattern of target K^+ fibers' time and energy. The K_L^0 production rate is

$$Rate_{K_L^0} \equiv \frac{N_{K_S^0}}{\epsilon_{K_S^0} \cdot A_{PV} \cdot \mathcal{B}(K_S^0 \rightarrow \pi^+\pi^-) \cdot KB_{live}/PS}, \quad (24)$$

$$= 2.73 \times 10^{-5}, \quad (25)$$

where the quantities used this calculation are summarized in Table 9. Monte Carlo simulates both $K_L^0 \rightarrow$

Description	Parameter	Values
# of selected K_S^0 events	$N_{K_S^0}$	8086
K_S^0 selection efficiency	$\epsilon_{K_S^0}$	0.138
Photon Veto efficiency	A_{PV}	0.680
$K_S^0 \rightarrow \pi^+\pi^-$ Branching Ratio	$\mathcal{B}(K_S^0 \rightarrow \pi^+\pi^-)$	0.686
# of K^+ Triggers (10^{12})	KB_{live}	1.77
Prescaling Factor	PS	384
K_L^0 Production Rate	$R_{K_L^0}$	2.73×10^{-5}

Table 9. K_L^0 production rate and the quantities that are used to estimate it.

$\pi^+\mu^-\bar{\nu}_\mu$ ($K_{\mu 3}^0$) and $K_L^0 \rightarrow \pi^+e^-\bar{\nu}_e$ ($K_{e 3}^0$) decays to estimate the CEX background level. In total, there are 2.076×10^{11} events generated for each decay mode, divided by the K_L^0 production rate gives 7.604×10^{15} for the corresponding number of K^+ entering the target.

These Monte Carlo events pass through all of the selection criteria, except for the $\pi^+ \rightarrow \mu^+ \rightarrow e^+$ decay sequence cuts and the beam cuts that are not related to the target quantities. Seventy-seven K_L^0 events survive in the signal region. It is observed that 56 events are from the $K_{e 3}^0$ decay mode and 21 are from the $K_{\mu 3}^0$ decay mode. Therefore, the expected CEX events can be estimated by means of

$$\begin{aligned} N_{CEX} &= \left(N_{pass}^{K_{e 3}^0} \times \frac{KB_{live}^{real}}{KB_{live}^{MC}} + N_{pass}^{K_{\mu 3}^0} \times \frac{KB_{live}^{real}}{KB_{live}^{MC}} \right) \times A \\ &= \left(56 \times \frac{1.77 \times 10^{12}}{7.604 \times 10^{15}} + 21 \times \frac{1.77 \times 10^{12}}{7.604 \times 10^{15}} \right) \times 0.250 \\ &= 0.00448 \pm 0.00051(stat.), \end{aligned} \quad (26)$$

where $N_{pass}^{K_{e 3}^0}$ and $N_{pass}^{K_{\mu 3}^0}$ are the numbers of $K_{e 3}^0$ and $K_{\mu 3}^0$ events surviving all the cuts, KB_{live}^{real} is the KB_{live} for the real data and A is the acceptance of the cuts that are not used for the Monte Carlo CEX events, and estimated to be 0.250.

3.7.6 Total background Evaluated from One-Third Sample

From the results of the one-third sample given in Table 8 and the CEX background estimated by Equation (26), one can derive $0.048 \pm 0.008_{stat.}$ events for the total background. This value is much smaller than the goal of 0.1 event set at the beginning of the signal search. In addition to the total background level, the bifurcation analyzes also give the corresponding background functions for the TD, the PV and the kinematic cuts, with which one can get the expected background level and relative acceptance change for a given cut position. The features were used in optimizing the selection criteria, studying the correlation of two bifurcation cuts and determining the branching ratio as well.

Cuts	Loosening factor	Acceptance gain
$\pi^+ \rightarrow \mu^+ \rightarrow e^+$	4.2	$\times 1.12$
$K_{\pi 2}$ kinematic	9.5	$\times 1.12$
Photon Veto	4.0	$\times 1.07$
Total acceptance gain		$\times 1.31$

Table 10. Loosening factors for the $\pi^+ \rightarrow \mu^+ \rightarrow e^+$ decay sequence cuts, the $K_{\pi 2}$ kinematic cuts and the photon veto cuts (second column) with their acceptance gains (third column).

3.7.7 Optimization of Signal Region

The distributions of both signals and backgrounds in the cut space are described well by the background functions. Since the background level from the one-third sample is much less than 0.1 event, the definition of signal region can be enlarged.

The cuts to be loosened are the TD, PV and KIN cuts, which are related to the $\pi^+ \rightarrow \mu^+ \rightarrow e^+$, PV and $K_{\pi 2}$ kinematic functions illustrated in Figure 38, 40 and 41. The cuts for the μ^+ and beam backgrounds are not loosened, because the cut positions for the $K_{\mu 2}$ range tail and μ^+ band backgrounds are at the knee in the background level v.s. acceptance curve; loosening them does not provide much acceptance gain. However, simultaneous loosening the cut positions of the $\pi^+ \rightarrow \mu^+ \rightarrow e^+$, PV and $K_{\pi 2}$ kinematic functions increases the background levels. When one of the three cuts is loosened, the cut positions of the other two are kept unchanged. The revised (enlarged) signal region consists of the standard signal region, plus three extensions. Hereafter, the revised and standard signal regions are referred to as the extended signal region and the standard region, respectively. The regions created by loosening the $\pi^+ \rightarrow \mu^+ \rightarrow e^+$ decay sequence cuts, PV cuts, and $K_{\pi 2}$ kinematic cuts are referred to as $\pi^+ \rightarrow \mu^+ \rightarrow e^+$ extended, PV extended, and $K_{\pi 2}$ kinematics extended regions, respectively. All of which include the standard region. The loosening factors for the cuts ($f_{\pi\mu e}$, $f_{K\pi 2}$ and f_{PV}) summarized in Table 10 are developed so that the background levels after loosening them are still acceptable. The loosening factors for these three cuts, $f_{\pi\mu e} = 4.2$, $f_{K\pi 2} = 9.5$ and $f_{PV} = 4.0$, mean 4.2-times more background related to the $\pi^+ \rightarrow \mu^+ \rightarrow e^+$ identification, 9.5-times more $K_{\pi 2}$ background and 4.0-times more background related to the photon veto. The total acceptance gain by enlarging the signal region is 31% (12% from $K_{\pi 2}$, 12% from $\pi^+ \rightarrow \mu^+ \rightarrow e^+$ identification, and 7% from the photon veto).

3.7.8 Correlation and Single Cut Failure Study

Bifurcation assumes that the two bifurcation cuts are not correlated. This assumption can be tested by comparing the predicted and observed rates near but outside the signal region. If the distributions of each background source is well understood with the two functions associated with the bifurcation cuts, the amount of the background can be estimated correctly for both near and outside the extended signal region.

A schematic representation of the region near, but outside, the signal region is shown in Figure 44. A near region outside the signal region (A' without the black region in Figure 44) is defined by loosening two bifurcation cuts (CUT1 and CUT2) simultaneously by the fixed factors a and b , respectively. If the background functions associated with the CUT1 and CUT2 are correct, the expected number of background events in the near region is estimated by either the direct bifurcation method

$$BG' = B'C'/D' - BC/D \quad (27)$$

If any deviation is seen between the observed and the predicted in the near region, then a correlation between the bifurcation cuts could be indicated and the background estimate may be unreliable. The observation is performed in the same way as the bifurcation method used in the background estimation

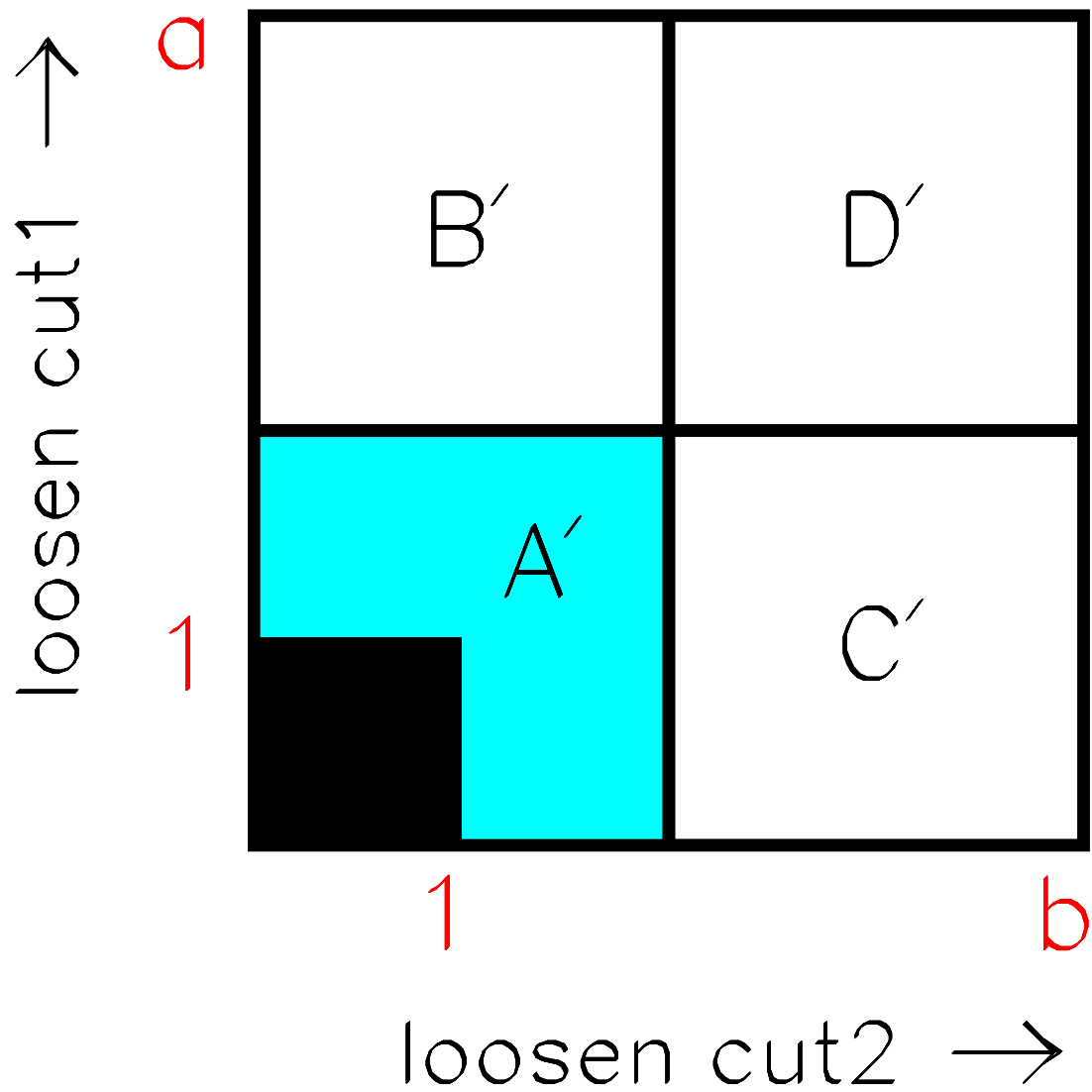


Fig. 44. Pictorial explanation of the correlation study using the events near, but outside the signal region. The vertical axis “ a ” and the horizontal axis “ b ” are for the loosen factors, while the 1×1 black region represents the signal region.

$K_{\pi 2}$ (1/3)	(Photon Veto) \times ($K_{\pi 2}$ kinematics)				
Loosen factor	10 \times 10	20 \times 20	20 \times 50	50 \times 50	50 \times 100
Bifurcation	0.5 \pm 0.3	2.3 \pm 0.9	4.3 \pm 1.4	8.1 \pm 3.6	24.3 \pm 7.4
Bkg func.	0.4 \pm 0.1	1.8 \pm 0.2	4.6 \pm 0.5	11.7 \pm 1.2	23.4 \pm 2.1
Observation	1	3	7	17	28
$K_{\mu 2}$ Range Tail (1/3)	$(\pi^+ \rightarrow \mu^+ \rightarrow e^+) \times (K_{\mu 2}$ kinematics)				
Loosen factor	10 \times 10	20 \times 20	50 \times 50	80 \times 50	120 \times 50
Bifurcation	0.2 \pm 0.2	1.2 \pm 0.6	7.0 \pm 3.1	9.5 \pm 3.5	12.0 \pm 4.0
Bkg func.	0.5 \pm 0.0	2.1 \pm 0.1	13.2 \pm 0.1	21.2 \pm 0.2	31.8 \pm 0.3
Observation	0	2	12	23	30
μ^+ Band (1/3)	$(\pi^+ \rightarrow \mu^+ \rightarrow e^+) \times (K_{\mu 2}$ kinematics)				
Loosen factor	10 \times 10	20 \times 20	50 \times 20	80 \times 20	80 \times 40
Bifurcation	0.7 \pm 0.4	1.2 \pm 0.7	6.7 \pm 2.2	8.1 \pm 2.6	65.8 \pm 24.2
Bkg func.	0.6 \pm 0.1	2.4 \pm 0.1	6.0 \pm 0.3	9.6 \pm 0.5	19.2 \pm 0.4
Observation	1	3	5	19	15

Table 11. Results of a correlation study for the $K_{\pi 2}$ (top), $K_{\mu 2}$ range tail (middle) and μ^+ band (bottom) backgrounds. The first row in each background represents the loosening factors of the bifurcation cuts; the second represents the predicted number of events in each outside-the-box region, which is obtained from Equation (27); the third represents the predicted number of events in each outside-the-box region; and the fourth represents the number of observed events in each region. The errors in the predictions are statistical uncertainties.

in the signal region, except that two bifurcation cuts are loosened by factors of a and b . The results of the correlation study for the $K_{\pi 2}$, $K_{\mu 2}$ range tail and μ^+ band backgrounds are summarized in Table 11. A good agreement is observed between the observed and the predicted (either from the bifurcation or the background function method). It is noted that the direct bifurcation still suffer relative large statistical fluctuation even loosening the bifurcation cuts by large amount. The test results are from the comparisons between the observed and the predicted from the background function method.

In addition to the study of correlation between the cuts used for the bifurcation method, events that failed a single cut are examined to check if each cut operates as designed for the appropriate background mechanism. Such a study can also provide a way to discover any new type of background. In the one-third sample, six of the eight events that failed a single cut were far from the cut position, while the other two events showed potential analysis flaws. The first flaw would artificially increase the measured range and momentum of π^+ s from $K_{\pi 2}$ decay that exited the upstream end of the target through the gap between the front face of the target and the B4 hodoscope. Additional cuts with minimal acceptance loss are devised to eliminate such events. The second revealed a possible correlation between the photon veto and the π^+ dip angle that was subsequently eliminated with a relative acceptance loss of 0.96%. All the cuts designed at this stage are referred as the pathology cuts as already described in Section 3.6.1.

3.7.9 Final Background Evaluated from Two-Thirds Sample

Evaluation of the final background levels come from the two-thirds sample. To get the values for the extended box, the corresponding values are scaled by the loosen factors given in Section 3.7.7, respectively. The TD rejection and PV rejection are measured to be 445 ± 111 and 84 ± 1 from the two-thirds sample. These values are in good agreement with those obtained from the one-third sample given in Table 8. The final results are summarized in Table 12. Good agreement is observed in both results from the one-third and the two-thirds samples.

The total background level in the extended signal region is estimated to be $0.33 \pm 0.03_{stat.}$ events, which is dominated by the $K_{\pi 2}$ background contribution. As the background distribution is not uniform in the signal region, the background functions obtained in the background study can be exploited to interpret any possible candidate event observed and to give proper branching ratio measurement by using the likelihood technique described in Section 4.

Background	Standard (1/3)	Standard (2/3)	Extended (1/3)	Extended (2/3)
$K_{\pi 2}$	0.014 ± 0.004	0.019 ± 0.004	0.174 ± 0.021	0.216 ± 0.023
$K_{\mu 2}$ range tail	0.012 ± 0.001	0.009 ± 0.001	0.054 ± 0.005	0.039 ± 0.003
μ^+ band	0.016 ± 0.005	0.013 ± 0.002	0.080 ± 0.021	0.065 ± 0.010
1-Beam	0.004 ± 0.002	0.004 ± 0.002	0.003 ± 0.002	0.006 ± 0.002
2-Beam	0.001 ± 0.001	0.003 ± 0.002	0.002 ± 0.002	0.003 ± 0.002
CEX	0.004 ± 0.001	0.004 ± 0.001	0.005 ± 0.001	0.005 ± 0.001
Total	0.051 ± 0.007	0.052 ± 0.005	0.318 ± 0.031	0.334 ± 0.025

Table 12. Total background level and the contribution from each background source for both standard and extended signal regions. The errors are statistical.

3.7.10 Systematic Uncertainty

Systematic uncertainty arises from the possible correlation between the two bifurcation cuts. The correlation is investigated using the two-thirds sample, the results are given in Table 13.

The observations over predictions gives a ratio c is used to quantify the degree of consistency in Table 13. Since the direct bifurcation method still suffer large statistical fluctuation, the predicted values are from the background function method. The uncertainty on the ratio c is within 25%. The systematic uncertainty is taken as the variation in the ratio c when the prediction number is varied by its uncertainty. The value of c for each background source is consistent with unity and confirms that the background estimations via the bifurcation method are reliable.

$K_{\pi 2}$ (2/3)	(Photon Veto) \times ($K_{\pi 2}$ kinematics)				
Loosen factor	10 \times 10	20 \times 20	20 \times 50	50 \times 50	50 \times 100
Bifurcation	1.0 \pm 0.4	4.0 \pm 1.1	9.5 \pm 2.1	42.2 \pm 9.9	55.8 \pm 11.9
Bkg function	1.1 \pm 0.2	4.9 \pm 0.6	12.4 \pm 1.3	31.1 \pm 3.1	62.4 \pm 5.6
Observation	3	4	9	22	53
$K_{\mu 2}$ Range Tail (2/3)	$(\pi^+ \rightarrow \mu^+ \rightarrow e^+) \times (K_{\mu 2}$ kinematics)				
Loosen factor	10 \times 10	20 \times 20	50 \times 50	80 \times 50	120 \times 50
Bifurcation	0.3 \pm 0.2	1.3 \pm 0.5	11.3 \pm 3.2	28.0 \pm 7.3	44.6 \pm 13.2
Bkg function	0.6 \pm 0.0	2.3 \pm 0.0	14.7 \pm 0.1	23.6 \pm 0.2	35.4 \pm 0.3
Observation	0	1	15	22	33
μ^+ Band (2/3)	$(\pi^+ \rightarrow \mu^+ \rightarrow e^+) \times (K_{\mu 2}$ kinematics)				
Loosen factor	10 \times 10	20 \times 20	50 \times 20	80 \times 20	80 \times 40
Bifurcation	1.1 \pm 0.5	4.3 \pm 1.5	6.9 \pm 2.2	8.8 \pm 2.8	15.3 \pm 5.2
Bkg function	0.9 \pm 0.1	3.5 \pm 0.1	8.9 \pm 0.3	14.2 \pm 0.5	28.4 \pm 0.5
Observation	1	5	12	16	35

Table 13. Results of a correlation study for the $K_{\pi 2}$ (top), $K_{\mu 2}$ range tail (middle) and μ^+ band (bottom) backgrounds. The first row in each background represents the loosening factors of the bifurcation cuts; the second represents the predicted number of events in each outside-the-box region; and the third represents the predicted number of events in each outside-the-box region from the background function method; and the fourth represents the number of observed events in each region. The errors in the predictions are statistical uncertainties.

Cut	Acceptance
RS tracking cuts	0.99996 ± 0.00001
UTC and Target tracking cuts	0.99568 ± 0.00010
Beam cuts	0.50779 ± 0.00074
The photon veto cuts	0.76784 ± 0.00218
γ -veto in RSSC	0.98195 ± 0.00015
μ -veto in RS	0.99591 ± 0.00057
$A_{K_{\mu 2}}$	0.3796 ± 0.0013

Table 14. Acceptances of the $K^+ \rightarrow \pi^+ \nu \bar{\nu}$ selection cuts measured from the $K_{\mu 2}$ monitor trigger data. The acceptance of beam cuts does not include those using the energy measurement in the target. The errors are statistical.

3.8 Acceptance and Sensitivity

To reduce the background level much less than one event in the signal region, this analysis utilizes many selection criteria, in which many of them cannot be estimated precisely from data. They are therefore split into several parts, which can then be measured separately using the monitor trigger data with the same detector responses and Monte Carlo, which gives the estimates on the decay phase space, the trigger efficiency and the nuclear interaction effects. Single event sensitivity is defined as the inverse product of the total number of K^+ 's stop in the target multiplying the acceptance.

3.8.1 Acceptance Factors from $K_{\mu 2}$ Events

Since the $K_{\mu 2}$ events have the same features as the signal regarding to the K^+ beam, the charged track and the event topology, the acceptances associated to the relevant cuts as listed in Table 14 can be directly measured using the $K_{\mu 2}$ monitor trigger data. Below are the details of the measurements.

Tracking in RS

To measure the acceptance of RS tracking, the above sample should have further cleaning (also called “set-up cuts”) to ensure an expected good track in RS without using the RS measurement. The event should have an IC hit, at least 5 ns IC time delay with respect to the C_K time, at least 1.2 MeV energy deposit in B4, and successful tracking in both UTC and target. All survival $K_{\mu 2}$ events are checked by the RS tracking requirement. This gives a measurement on the acceptance of RS tracking.

Tracking in UTC and Target

Because there is no photon activity for $K_{\mu 2}$ peak events, the $K_{\mu 2}$ monitor is an ideal sample to measure the acceptance of target pattern recognition. The sample is from the events surviving the RS tracking cuts above. To get rid of possible beam background contamination, this sample should also meet all the timing requirements on the beam instruments. A 5 ns timing consistency is also required between the IC time and the track time. Since the sample may contain some $K_{\mu 2\gamma}$ events, also required are all the photon veto cuts except that uses the BV and BVL information. This is due to the fact that longer range $K_{\mu 2}$ events can often reach up to the BV and BVL. Events surviving from the above set-up cuts are then checked with the UTC and target requirements, giving a measurement on the relevant acceptance.

Cut	Acceptance
Opposite side of π^+ cluster veto	0.98464 ± 0.00108
Target kinematic cuts	0.89224 ± 0.00275
$A_{K_{\pi 2}}$	0.8785 ± 0.0029

Table 15. Acceptances of the $K^+ \rightarrow \pi^+ \nu \bar{\nu}$ selection cuts from the $K_{\pi 2}$ monitor trigger data. The errors are statistical only.

Beam selection criteria

The $K_{\mu 2}$ events are chosen from those satisfying the requirement on tracking in UTC and Target described above but without the timing requirements on the beam instruments. To further ensure these $K_{\mu 2}$ events with no beam background contamination, the momentum deviation is required to be less than $\pm 2\sigma$'s around the $K_{\mu 2}$ peak and, the absolute cosine of polar angle of track should be less than 0.5. Also required is that there is no scattering of track found in the RS. The remaining events then pass through all the beam cuts except for those using energy and range measurement information in the target, providing a measurement on the corresponding beam selection criteria. Because of the clean feature of $K_{\mu 2}$ events, the DC trigger efficiency is also measured and included in the acceptance of beam selection criteria.

Photon veto

Since the pure $K_{\mu 2}$ events do not contain any photon, they can also provide an ideal sample to measure the acceptance of photon veto. To ensure a clean sample, all the selection criteria used in above acceptance are applied except for the photon veto cuts. In addition, the stopping layer is required prior to the 19th RS layer. All the photon veto cuts including the online photon veto can thus be measured.

γ -veto in RSSC

To reject the associated photon activity, events are required not to stop in the 14th RS layer with a prompt RSSC hit in the same sector or one sector clockwise of any 14th RS layer hit, leading to acceptance loss. Using the $K_{\mu 2}$ monitor events and applying the above cut to those with hits in the second layer of RSSC can give a measurement on the corresponding acceptance value.

μ -veto in RS

The $pnn1$ trigger involves a μ -veto in the last RS layer, requiring that there should not be a hit in the 19th RS layer associated with a $T \cdot 2$ in the same sector or the two previous sectors. This can result in acceptance loss when accidental hit happens in this layer in an otherwise good signal candidate event. This loss is also measured by using the $K_{\mu 21}$ monitor events. The sample is selected by applying all the cuts used in above studies except for the momentum cut. The stopping layer is required to be at 17. To further clean the sample, the range is required to be longer than 40 cm. In this selected sample, the online trigger bit for the 19th RS layer is checked, giving a measurement on the acceptance.

3.8.2 Acceptance Factors from $K_{\pi 2}$ Events

The $K_{\pi 21}$ monitor trigger data are used to measure the acceptances for the target cuts involving the energy and range measurement, since the cut positions are particle-type dependent. The $K_{\pi 2}$ events are selected with all cuts applied except for those to be measured. To ensure good $K_{\pi 2}$ events, the momentum, range and energy are required to be within 2σ 's of the $K_{\pi 2}$ peak positions. A $\pi^0 \rightarrow \gamma\gamma$ should also be found in each event. The results are given in Table 15.

3.8.3 Kinematic Acceptance Factors from Beam π^+ Events

The beam π^+ monitor trigger data can provide a pure π^+ sample, which can be used to measure all the selection criteria related to the particle type in UTC and RS: the UTC track quality cuts, the range-momentum consistency cut, the RS dE/dx cuts, the RS track quality cuts and the stopping layer cut. The events are required to pass the PASS 1 cuts and the TD π^+ selection cuts. The cuts on beam instruments are inverted to select beam π^+ 's. The IC time agrees with the track time within 5 ns. The phase space cuts are additionally applied to select the events in the same signal phase space. The acceptance is measured to be

$$A_{\text{Beam}\pi^+} = 0.6161 \pm 0.0085_{\text{stat.}} \pm 0.0189_{\text{sys.}} \quad (28)$$

Since these π^+ 's come from the beam π^+ scattering in the target and not from the K^+ decays at rest. Classification of the K^+ fibers and π^+ fibers may be screwed up because their timings are close to each other, and energy deposits of the incoming and outgoing particles around the vertex point are somehow different between scatterings and decays at rest. Both of these features would result in more uncertainties in the momentum, energy and range measurements in these π^+ events. Systematic uncertainty is therefore investigated by loosening or tightening the phase space cuts by ± 1 standard deviation. The variation is treated as the systematic uncertainty.

3.8.4 $\pi^+ \rightarrow \mu^+ \rightarrow e^+$ Decay Acceptance from Beam π^+ Events

The acceptance of $\pi^+ \rightarrow \mu^+ \rightarrow e^+$ decay sequence (TD cuts) is measured by using the Beam π^+ monitor trigger data. This acceptance measurement includes both of the online and offline π^+ identification cuts. The online ones include Level-1.1 and Level-1.2 in trigger. The sample is selected using the same cuts as those used in measuring $A_{\text{Beam}\pi^+}$ except for the TD cuts to be measured here. It should be noted that this measurement includes the pion absorption and pion decay-in-flight, which will be estimated using Monte Carlo in Section 3.8.5. A 1.4% correction estimated by the simulation is already applied to the acceptance given below

$$A_{\pi^+ \rightarrow \mu^+ \rightarrow e^+} = 0.3523 \pm 0.0077_{\text{stat.}} \pm 0.0067_{\text{sys.}}, \quad (29)$$

getting rid of the double counting problem of the acceptance. Since the TD cuts may be correlated to the KIN cuts regarding to the particle identification, the acceptance is investigated with and without the dE/dx cuts. The observed 2% variation on the acceptance is assigned as the systematic uncertainty.

3.8.5 Acceptance Factors from Monte Carlo Simulation

The acceptance measurements using the Monte Carlo simulation of the $K^+ \rightarrow \pi^+ \nu \bar{\nu}$ are for the trigger acceptance, the phase space acceptances, the acceptance loss due to the π^+ absorption and π^+ decay-in-flight, and the π^+ nuclear interaction.

Trigger Bits

All the trigger conditions as described in Section 2.8 are simulated in Monte Carlo except for the DC, Level-1.1 and Level-1.2, which have already been measured using the $K_{\mu 2}$ and Beam π^+ monitor trigger data. The π^+ nuclear interaction is not included in this simulation and is considered separately. The acceptance for the rest is

$$A_{\text{trig}} = 0.1796 \pm 0.0010_{\text{stat.}} \pm 0.0059_{\text{sys.}}, \quad (30)$$

where the systematic uncertainty is estimated to be 3.3% from the measurement on the branching ratio of $K_{\pi 2}$. It is noted that the trigger acceptance measured here is all actually the phase space dependence.

Phase Space

The phase space acceptance is for the offline cuts on the momentum, range and energy. To measure the phase space acceptances (A_{PS}), events are first taken from those surviving from the trigger in Monte Carlo simulation, and then are applied with the phase space cuts. The π^+ nuclear interaction is also not included in this simulation. The acceptance is measured to be

$$A_{PS} = 0.3630 \pm 0.0029_{stat.}, \quad (31)$$

which includes the loss due to both the π^+ absorption and π^+ decay-in-flight.

Correction for Nuclear Interaction

The nuclear interaction effect is investigated separately, in order to study the systematic uncertainty associated to it. The $K^+ \rightarrow \pi^+ \nu \bar{\nu}$ events are generated with and without nuclear interaction, respectively. The ratio between both the trigger acceptances multiplying the ratio between both the phase space acceptances gives the correction for nuclear interaction

$$A_{nuc.} = 0.4953 \pm 0.0077_{stat.} \pm 0.0248_{sys.}, \quad (32)$$

where the systematic uncertainty takes into account the observed 0.15σ difference on the range resolution. This difference can affect the acceptance due to the $Rdev$ cut and is translated into a 5% uncertainty in the acceptance. It should be pointed that this definition can count all the losses associated with the nuclear interactions. For example, if there are extra splashes of energy in the detector associated with the nuclear interactions that cause the photon veto to fire. This loss is not included in the $K_{\mu 2}$ -based acceptance $A_{K_{\mu 2}}$ given in Table 14, because μ^+ 's do not undergo nuclear interactions.

3.8.6 Correction to $T \cdot 2$ Inefficiency

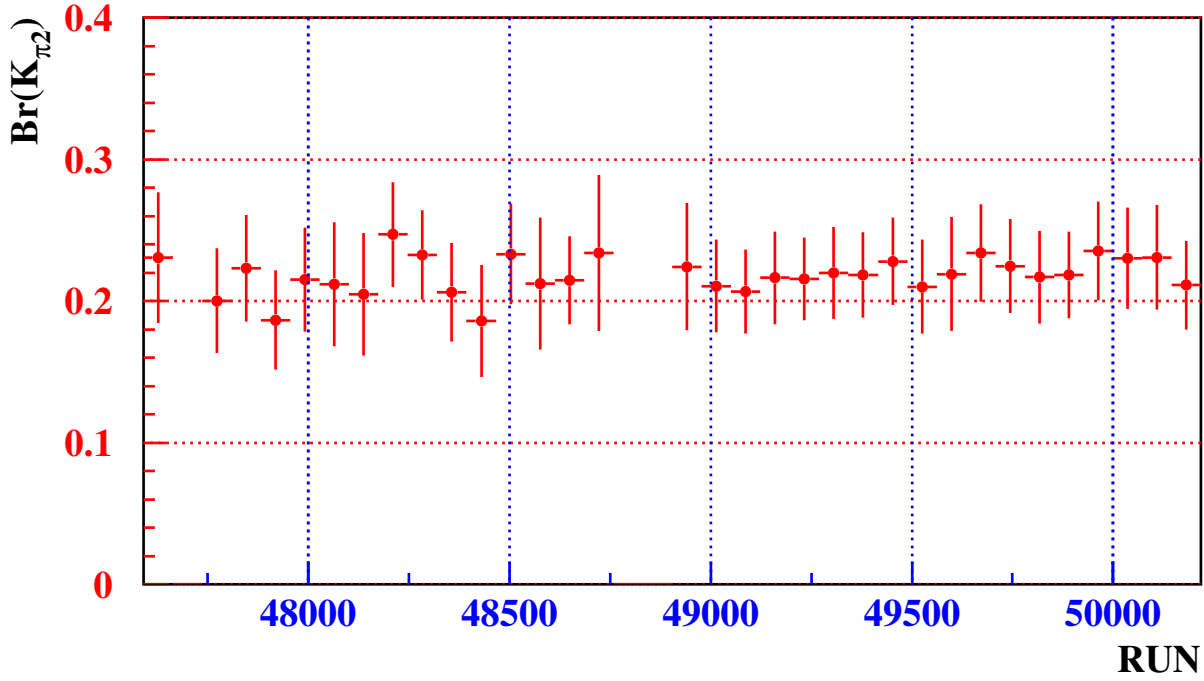
It is observed that the $T \cdot 2$ simulation result doesn't include the acceptance loss due to the geometrical and counter inefficiencies of the T-Counters. The geometrical inefficiency represents the inefficiency due to the track passing through an azimuthal gap between two adjacent T-Counters. The $T \cdot 2$ inefficiency is measured by using the $K_{\mu 2}$ and $K_{\pi 2}$ events in the beam K^+ monitor data. Using the UTC track extrapolation gives the expected $T \cdot 2$ counter. The online $T \cdot 2$ bits of the reconstructed events are checked to measure the $T \cdot 2$ efficiency for both $K_{\mu 2}$ and $K_{\pi 2}$ events, separately. Since the signal energy deposit in the $T \cdot 2$ counter from the $K_{\mu 2}$ and $K_{\pi 2}$ events is somewhat different, simulations are done for all these two decay modes to get the average energy deposits. Using the energy extrapolation gives the correction to the $T \cdot 2$ inefficiency for the signal

$$A_{T \cdot 2} = 0.9358 \pm 0.0011(stat.) \pm 0.0140(sys.), \quad (33)$$

where the systematic uncertainty accounts for the fact that there is 1.5% variation when changing the z requirement on the UTC track extrapolation to the $T \cdot 2$ counter.

3.8.7 Normalization to $K_{\mu 2}$ Branching Ratio

Since the K^+ beam can decay before entering the target or travel all the way through the target, the total number of K^+ 's counted by the C_K should be corrected with the stopping fraction. This fraction is obtained by normalizing the total K^+ exposures with the $K_{\mu 2}$ branching ratio. The $K_{\mu 2}$ events are selected from the $Km2$ monitor trigger data with the same selection criteria as those used for signal, excluding all the cuts related to the π^+ particle type, the BV and the BVL. The momentum, range and energy cuts are substituted with a minimum 40 cm range requirement. The acceptance measurement is



[t]

Fig. 45. Measurement of the $K^+ \rightarrow \pi^+ \pi^0$ branching ratio as a function of run number in E949.

also preformed in the same way as that for the signal. This stopping fraction is computed by

$$\begin{aligned}
 f_s &= \frac{N_{K_{\mu 2}}}{K_{Blive}^{eff.}(K_{\mu 2}) \cdot Acc(K_{\mu 2})}, \\
 &= 0.7740 \pm 0.0011_{stat.}
 \end{aligned} \tag{34}$$

where the $N_{K_{\mu 2}}$ is the number of survival $K_{\mu 2}$ events. The $K_{Blive}^{eff.}$ is the total K^+ exposures (1.77×10^{12}) with pre-scaling factor (from 81920 to 327680) to the $Km2$ monitor trigger during the entire data acquisition period. The $Acc(K_{\mu 2})$ is the acceptance.

3.8.8 Confirmation by $K_{\pi 2}$ Branching Ratio

Measurement of the $K_{\pi 2}$ branching ratio confirmed the correctness in evaluating the acceptances of the $K^+ \rightarrow \pi^+ \nu \bar{\nu}$ selection cuts. Stopped $K_{\pi 2}$ events are selected from the $Kp21$ monitor trigger data by imposing the cuts similar to the $K^+ \rightarrow \pi^+ \nu \bar{\nu}$ selection criteria except for those used for the photon veto and for defining the kinematic signal region. Good $K_{\pi 2}$ events also meet the requirements on the energy, momentum and range, which are defined to be within the $\pm 3\sigma$ region of the $K_{\pi 2}$ peaks. The acceptance of the $K_{\pi 2}$ mode is estimated in the same way as that of the $K^+ \rightarrow \pi^+ \nu \bar{\nu}$ mode except that the phase cuts are different and the photon veto PV is removed. Figure 45 shows the variation of the measured $K_{\pi 2}$ branching ratio as a function of run number. A stable branching ratio is observed. The $K_{\pi 2}$ branching ratio is measured to be $\mathcal{B}(K_{\pi 2}) = 0.2190 \pm 0.0050(stat.)$. This value agrees with the PDG value 0.212 ± 0.001 within 3.3%, indicating the validation of the acceptance measurement. This error is treated as the systematic uncertainty and assigned to the acceptance A_{trig} in Equation (30).

Contribution	Acceptance
$A_{K_{\mu 2}}$	$0.3796 \pm 0.0013_{stat.}$
$A_{K_{\pi 2}}$	$0.8785 \pm 0.0029_{stat.}$
$A_{Beam\pi^+}$	$0.6161 \pm 0.0085_{stat.} \pm 0.0189_{sys.}$
$A_{\pi^+ \rightarrow \mu^+ \rightarrow e^+}$	$0.3523 \pm 0.0077_{stat.} \pm 0.0067_{sys.}$
A_{trig}	$0.1796 \pm 0.0010_{stat.} \pm 0.0059_{sys.}$
A_{PS}	$0.3630 \pm 0.0029_{stat.}$
$A_{nucl.}$	$0.4953 \pm 0.0077_{stat.} \pm 0.0248_{sys.}$
$A_{T.2}$	$0.9358 \pm 0.0011_{stat.} \pm 0.0140_{sys.}$
f_s	$0.7740 \pm 0.0011_{stat.}$
$A_{total}^{standard} (\times 10^{-3})$	$1.69 \pm 0.05_{stat.} \pm 0.14_{sys.}$

Table 16. A breakdown of the acceptances for the $K^+ \rightarrow \pi^+ \nu \bar{\nu}$ selection cuts.

3.8.9 Summary of Acceptance and Sensitivity

The acceptances of the $K^+ \rightarrow \pi^+ \nu \bar{\nu}$ decay were split into several parts as already given above. Table 16 summarizes all the contributions to the total acceptance in the standard region $A_{total}^{standard}$. To get the acceptance in the extended signal region, the scaling factors given in Section 3.7.7 are applied to the acceptances for $A_{\pi \rightarrow \mu \rightarrow e}$, $A_{K_{\mu 2}}$ and A_{PS} , yielding the final acceptance as

$$Acc. = (2.22 \pm 0.07_{stat.} \pm 0.15_{sys.}) \times 10^{-3}. \quad (35)$$

This value also includes the contribution from the stopping fraction. In the physics run of the E949 the number of the K^+ flux is measured to 1.77×10^{12} . Therefore, the single event sensitivity of the E949 2002 run is given by

$$Sen. = (2.55 \pm 0.08_{stat.} \pm 0.18_{sys.}) \times 10^{-10}. \quad (36)$$

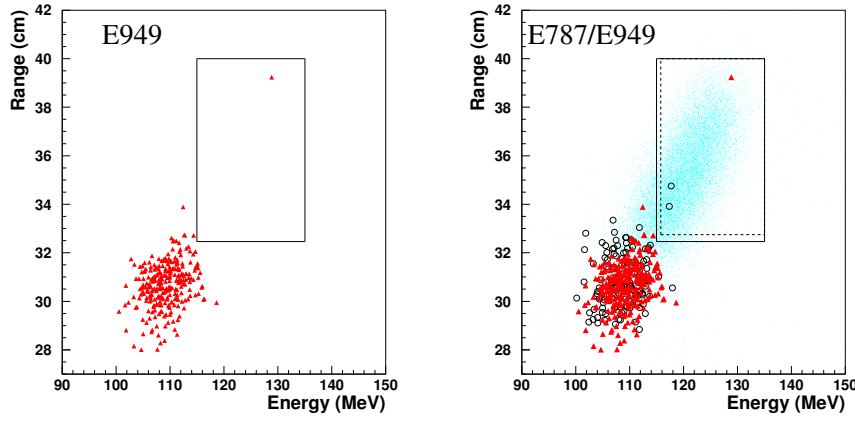


Fig. 46. Range vs kinetic energy of the events satisfying all of the cuts, except for the phase space cuts on both the range and energy. The plots are shown separately for E949 only (left) and E787 plus E949 results. The rectangle represents the signal region defined in E787 (dashed lines) and E949 (solid lines). Events around $E = 110 \text{ MeV}/c$ are due to $K_{\pi 2}$, which are not removed by the photon veto cuts.

3.9 Examining Signal Region

After the background analysis and the acceptance measurement are completed and satisfactory, all the selection criteria can then be applied to the data (referred as “open the signal box”). At the stage of examining the signal region, no cut can be changed.

One candidate event is observed inside the signal region. Figure 46 shows the range and kinetic energy of the events that pass all of the selection criteria, except for the phase space cuts on both the range and energy. This candidate together with the other two observed in E787 are shown in the same plot (also see Figure 46). As indicated in the plot, the signal box definition in E949 is extended in comparison to that in E787. Figure 47 is an event display for this candidate. This event has a momentum of $227.3 \text{ MeV}/c$, a kinetic energy of 128.9 MeV , a range of 39.2 cm and a χ_{rm} value of 0.6 . Kinematically, this candidate event agrees with all the requirements as a signal, though it exists in a relatively small acceptance region.

The expected signal distributions in the study of selection criteria are used to construct the probability of each cut quantity for this candidate. The probabilities for the single K^+ beam requirements and the decay π^+ kinematic requirements show a rather flat distribution, which is consistent with the expected signal distribution. There is no photon activity at all for this candidate. The distribution of the probability values for all the quantities used the $\pi^+ \rightarrow \mu^+ \rightarrow e^+$ decay sequence is somewhat in favor of the μ^+ hypothesis because of the observed shorter π^+ lifetime, as also shown in the display of the TD data in the π^+ stopping counter in Figure 47.

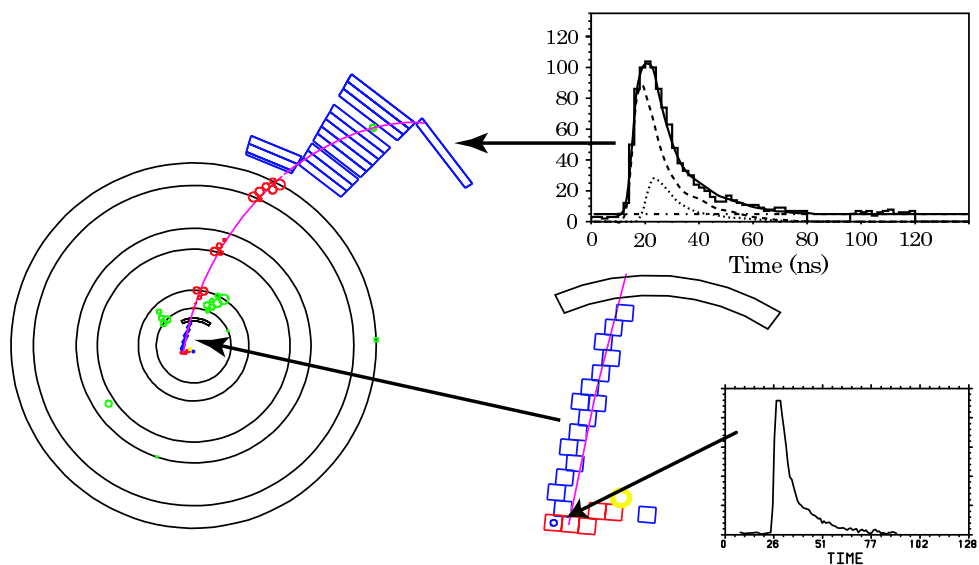


Fig. 47. Reconstruction of the candidate event (end view). Also displayed are the TD data in the π^+ stopping counter and the reconstruction in the target.

Function	Bin	Relative background
$K_{\pi 2}$ kinematics	$0.0 \leq N_{K\pi 2} < 0.2$	0.00
PV	$0.1 < N_{PV} < 0.2$	0.11
Muon Band	$0.0 < N_{Band} < 0.5$	0.29
$K_{\mu 2}$ Range Tail	$0.4 < N_{Tail} < 0.6$	0.51
$\pi^+ \rightarrow \mu^+ \rightarrow e^+$	$1.0 < N_{\pi \rightarrow \mu \rightarrow e} < 1.5$	1.23
1-Beam	$0.0 \leq N_{1beam} < 0.2$	0.00
2-Beam	$0.0 \leq N_{2beam} < 0.2$	0.00

Table 17. Bin in each background function and relative level for each background component for the candidate event.

4 Results

In this section we describe the method used to extract the $K^+ \rightarrow \pi^+ \nu \bar{\nu}$ branching ratio and the impact of the E949 and E787 $K^+ \rightarrow \pi^+ \nu \bar{\nu}$ candidates on the unitarity triangle. We also describe the implication of the observed candidates on the hypothetical decay $K^+ \rightarrow \pi^+ X^0$ where X^0 is a stable, massless, non-interacting particle[29].

4.1 Likelihood Method

We use as a test statistic the likelihood ratio X defined as

$$X \equiv \prod_{i=1}^n X_i \quad (37)$$

with

$$X_i \equiv \frac{e^{-(s_i+b_i)}(s_i+b_i)^{d_i}}{d_i!} \bigg/ \frac{e^{-b_i}b_i^{d_i}}{d_i!} \quad , \quad (38)$$

where s_i and b_i are the estimated signal and background in the i^{th} cell, d_i is the number of signal candidates in the i^{th} cell and the product runs over all cells[58]. In addition the likelihood estimator X_{obs} is defined as the value of X given the observed candidates. Cells are defined based on the background functions described in Section 3. The background functions show that there is additional background rejection within the signal region that can be exploited by division of the signal region into 3781 cells. The division was performed prior to the examination of the signal region.

The cell containing the candidate event is defined by the bins in the background functions and is shown in Table 17. The estimated levels of each component of the background as well as the acceptance in the cell containing the signal candidate are summarized in Table 18. The largest contribution to the total background level in this cell (5.745×10^{-5} events) is the $K_{\mu 2}$ Range Tail background (4.917×10^{-5} events). The ratio of the acceptance in this cell to the total acceptance in the standard region ($A_{total}^{standard} = 0.001694$) is estimated to be 1.21×10^{-4} . The expected number of signal events in this cell is therefore calculated as

$$\begin{aligned} s_i &= N_K \cdot \mathcal{B} \cdot A_{total}^{1 \times 1} \cdot A_i \\ &= 1.770 \times 10^{12} \cdot \mathcal{B} \cdot 0.001694 \cdot 1.21 \times 10^{-4} \\ &= 3.628 \times 10^5 \cdot \mathcal{B}, \end{aligned} \quad (39)$$

where \mathcal{B} represents the $K^+ \rightarrow \pi^+ \nu \bar{\nu}$ branching ratio and N_K is the total number of stopped K^+ .

Source	Background
$K_{\pi 2}$	0.029×10^{-5}
Muon (Muon Band) ($K_{\mu 2}$ Range Tail)	5.632×10^{-5} (0.715×10^{-5}) (4.917×10^{-5})
1 Beam (including CEX)	0.058×10^{-5}
2 Beam	0.026×10^{-5}
Total Background b_i	5.745×10^{-5}
Relative Cell Acceptance A_i	1.210×10^{-4}

Table 18. Contribution of each background source to the estimated number of background events in the cell containing the candidate event. The ratio of the acceptance of the cell to the total acceptance of the 1×1 region is also tabulated in this table.

4.2 Branching Ratio of $K^+ \rightarrow \pi^+ \nu \bar{\nu}$

The central value of the branching ratio, defined as the value of \mathcal{B} that maximizes X_{obs} [60], is 0.96×10^{-10} . With the E949 data only, we determine $\mathcal{B}(K^+ \rightarrow \pi^+ \nu \bar{\nu}) = (0.96_{-0.47}^{+4.09}) \times 10^{-10}$ where the quoted 68% confidence level (CL) interval is determined from the behavior of X as described in Ref.[58] and includes only the statistical uncertainty. The estimated probability that the E949 candidate is due to background alone is 0.074.

The results from both E787 and E949 are combined to calculate the branching ratio for $K^+ \rightarrow \pi^+ \nu \bar{\nu}$. In the E787 $K^+ \rightarrow \pi^+ \nu \bar{\nu}$ analysis, two $K^+ \rightarrow \pi^+ \nu \bar{\nu}$ candidate events were observed in the signal region[34,35]. The 3781 cells describing the E949 signal region are augmented by 488 cells that define the signal regions for the E787 analyses to produce a likelihood estimator X_{obs} for the combined data.

The evaluated confidence intervals for the combined E787 and E949 results take into account the estimated systematic uncertainty in the signal acceptance and the background rates. The systematic uncertainty of each background source was estimated to 25% based upon the results of the correlation study. From the sensitivity calculation described in Chapter 3.8, the systematic uncertainty on the acceptance was estimated to be 10%. The systematic uncertainty of each background component and the acceptance were assumed to be uncorrelated and to follow a normal distribution with the magnitudes given above regarded as one standard deviation. With these assumptions, the $K^+ \rightarrow \pi^+ \nu \bar{\nu}$ branching ratio for the combined E787 and E949 result is $\mathcal{B}(K^+ \rightarrow \pi^+ \nu \bar{\nu}) = (1.47_{-0.89}^{+1.30}) \times 10^{-10}$ where the uncertainty denotes the 68% CL interval. The corresponding 80% and 90% CL intervals are $(0.42, 3.22) \times 10^{-10}$ and $(0.27, 3.84) \times 10^{-10}$, respectively. The estimated probability that all the $K^+ \rightarrow \pi^+ \nu \bar{\nu}$ candidates observed in E787 and E949 are due to background is 0.001. The inclusion of the estimated systematic uncertainties has an almost negligible effect on the CL intervals due to the relatively poor statistical precision inherent in a sample of three candidate events.

4.3 Implication for $\mathcal{B}(K^+ \rightarrow \pi^+ X^0)$

The experimental signature of a $K^+ \rightarrow \pi^+ X^0$ event is identical to that of $K^+ \rightarrow \pi^+ \nu \bar{\nu}$ except that the kinematic signature afforded by the two-body decay ($P(\pi) = 227.1$ MeV, $E(\pi) = 127.0$ MeV, $R(\pi) = 38.6$ cm) permits the definition of a relatively high-acceptance, low-background signal region. The analysis method is identical to that used for the $K^+ \rightarrow \pi^+ \nu \bar{\nu}$ analysis except that the signal region is defined to be within two standard deviations of the expected momentum, energy and range of the charged pion with the upper limits of the tightened to $P \leq 229$ MeV/c, $E \leq 135$ MeV, and $R \leq 40$ cm to suppress $K^+ \rightarrow \mu^+ X$ background. The expected background level is small (0.05 events), because the region is far from the $K_{\pi 2}$ peak.

The candidate event observed in the signal region for $K^+ \rightarrow \pi^+ \nu \bar{\nu}$ E949 analysis is also in the $K^+ \rightarrow \pi^+ X^0$ signal region.

The acceptance studies for $K^+ \rightarrow \pi^+ X^0$ decay parallel those for the $K^+ \rightarrow \pi^+ \nu \bar{\nu}$ and the sensitivity for the E949 $K^+ \rightarrow \pi^+ X^0$ analysis is estimated to be $(0.82 \pm 0.02 \pm 0.06) \times 10^{-10}$, where the first and second errors are the statistical and systematic uncertainties, respectively.

No candidates were observed in the $K^+ \rightarrow \pi^+ X^0$ signal region of E787[34,35]. The combined E787 and E949 sensitivity is 0.196×10^{-10} and, interpreting the one observed candidate without subtraction of the estimated background, the upper limit on the branching ratio is $\mathcal{B}(K^+ \rightarrow \pi^+ X^0) < 0.747 \times 10^{-10}$ at 90% CL using the Feldman-Cousins method[61]. This limit is larger than the previous 90% CL limit of 0.59×10^{-10} of E787[34,35] due to the candidate event in E949.

4.4 Impact on Unitarity Triangle

As described in Section 1, the $K^+ \rightarrow \pi^+ \nu \bar{\nu}$ branching ratio is directly proportional to the real and imaginary parts of $\lambda_t \equiv V_{ts}^* V_{td}$ (Eqn. 9). In Figure 48 the regions of the complex λ_t plane allowed by the $K^+ \rightarrow \pi^+ \nu \bar{\nu}$ branching ratio determined from the combined E787 and E949 results is compared to the regions allowed by other recent measurements with small theoretical uncertainties[62]. The region favored by other CKM-sensitive measurements is at the edge of the 68% CL region allowed by the $K^+ \rightarrow \pi^+ \nu \bar{\nu}$ measurement.

The other CKM-sensitive results[62] used to produce the confidence level intervals in Figure 48 are dominated by measurements of B meson decays. The possible discrepancy between the λ_t regions allowed by the B measurements and by $\mathcal{B}(K^+ \rightarrow \pi^+ \nu \bar{\nu})$ could be an indication of physics beyond the standard model. As emphasized in[63], the clean theoretical interpretation of $K \rightarrow \pi \nu \bar{\nu}$ remains valid in most extensions of the SM in distinct contrast to the B measurements currently used to determine the CKM parameters. Thus a precision measurement of $\mathcal{B}(K^+ \rightarrow \pi^+ \nu \bar{\nu})$ ($\mathcal{O}(10\%)$) would provide an unambiguous test of the flavor sector of the SM.

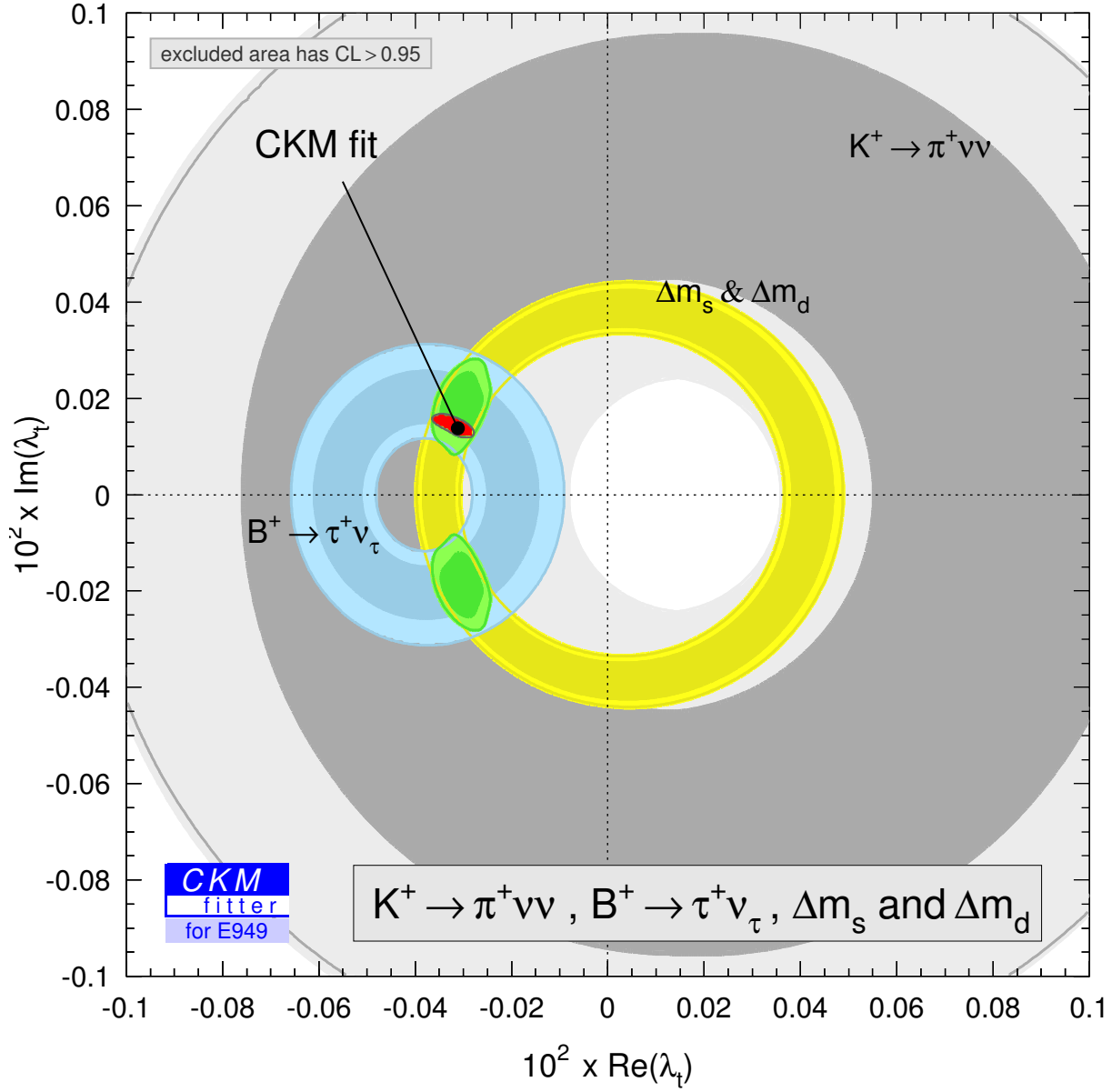


Fig. 48. The allowed regions in the λ_t plane allowed by the combined E787 and E949 determination of the $K^+ \rightarrow \pi^+ \nu \bar{\nu}$ branching ratio (gray), $B^+ \rightarrow \tau^+ \nu$ (blue) and B-mixing measurements (yellow). The regions outside the lighter (darker) shading have CL > 0.95 (0.68). The area excluded by $K^+ \rightarrow \pi^+ \nu \bar{\nu}$ at CL > 0.95 is indicated by the gray line. The red-shaded region is allowed by the combination of these measurements and the small black region denotes the region allowed by all CKM-related measurements as evaluated by the CKMfitter group[62].

5 Conclusion

The rare decay $K^+ \rightarrow \pi^+ \nu \bar{\nu}$ is a flavor-changing-neutral-current process and proceeds via 1-loop diagrams that mediate the top quark. This decay involves the coupling of top to down quarks. The branching ratio of $K^+ \rightarrow \pi^+ \nu \bar{\nu}$ is expressed by the magnitude of the CKM matrix element, $|V_{td}|$. Measuring $\mathcal{B}(K^+ \rightarrow \pi^+ \nu \bar{\nu})$ is one of the cleanest ways to extract $|V_{td}|$.

BNL-E949 is a successor to BNL-E787. The E949 detector was upgraded to achieve better measurements in the beam rate, twice that of E787. E949 examined stopped K^+ decays. A high-intensity K^+ beam was produced at the Alternating Gradient Synchrotron (AGS) by exposing 65 trillion protons per spill to a platinum target. Kaons with 710 MeV/c were transported to the E949 detector, and came to rest in a scintillating fiber target. 3.9×10^6 K^+ 's decayed at rest in the target per spill. The data were collected in 2002, which corresponded to 1.77×10^{12} K^+ decays.

The data were analyzed by a blind analysis. The Signal Region was masked out until the selection criteria were determined and the background levels were estimated. The development of the cuts and the estimation of the background levels were performed by using the Bifurcation Method. The Signal Region was enlarged compared to that in E787 with an increased confidence in the likelihood analysis. The enlargement of the Signal Region increased the acceptance by 30%. The total background level in the Signal Region was estimated to be 0.30 ± 0.02 events.

An examination of the Signal Region yielded one event near the upper kinematic limit of the $K^+ \rightarrow \pi^+ \nu \bar{\nu}$ decay. Based on the candidate event, an upper limit was set to be $\mathcal{B}(K^+ \rightarrow \pi^+ \nu \bar{\nu}) < 8.76 \times 10^{-10}$ at the 90% CL. E787 and E949 results were combined and the branching ratio was measured to be $(1.47^{+1.60}_{-0.93}) \times 10^{-10}$ at the 68% CL interval based on three events observed in the momentum region $211 \leq P \leq 229$ MeV/c. The measured branching ratio was twice as large as the SM prediction of $(0.78 \pm 0.12) \times 10^{-10}$, but was consistent within the error. At the measured central value of the branching ratio, the candidate event had a signal-to-background ratio of 0.9.

From the measured branching ratio, we set the limits on both $|\lambda_t|$ and $|V_{td}|$ to be

$$0.107 \times 10^{-3} < |\lambda_t| < 1.256 \times 10^{-3} \quad \text{and} \quad 0.0024 < |V_{td}| < 0.0322,$$

at the 90% CL interval, which was consistent with the current experimental range of $0.0048 < |V_{td}| < 0.014$ at the 90% CL interval.

6 Acknowledgements

We gratefully acknowledge the support and efforts of the BNL Collider-Accelerator Division for the high quality of kaon beam. We wish to thank Jose Ocariz of the CKMfitter group for producing Figure 48. We acknowledge the monetary support of the appropriate agencies in Japan, Russia, Canada and the US (**details of agency names and grant numbers here**). Due to a financial shortfall brought about by possible mismanagement of other DOE High Energy Physics projects, E949 was abruptly terminated after receiving only 20% of its approved running time. We wish to thank the managers of these other projects for changing our careers and throwing the prospects of future international cooperation into disarray.

1. W. Buchmiller, hep-ph/0306047
2. A.D. Sakharov, JETP Lett 5(1967) 24
3. V.A. Rubakov, M.E. Shaposhnikov, Usp. Fiz Nauk 166 (1996) 493; Phys. Usp. 39 (1996) 461; A Riotto and M. Trodden, Annu. Rev. Nucl. Part. Sci. 49(1999) 35.
4. M. Kobayashi and T. Maskawa, Prog. Theor. Phys. **49**, 652 (1973).
5. L. Wolfenstein, Phys. Rev. Lett. **51**, 1945 (1983).
6. C. Jarlskog, Phys. Rev. Lett. **55**, 1039 (1985); C. Jarlskog, Z. Phys. **C29**, 491 (1985); C. Jarlskog and R. Stora, Phys. Lett. **B208**, 268 (1988).
7. Particle Data Group, S. Eidelman *et al.*, Phys. Lett. **B592**, 1 (2004)
8. A.J. Buras, F. Schwab, and S. Uhlig, arXiv:hep-ph/0405132 (2004).
9. T. Inami and C.S. Lim, Prog. Theor. Phys. **65**, 297 (1981).
10. G. Buchalla and A.J. Buras, Nucl. Phys. **B548**, 309 (1999).
11. G. Buchalla and A.J. Buras, Nucl. Phys. **B398**, 285 (1993).
12. M. Musiak and J. Urban, Phys. Lett. **B451**, 161 (1999).
13. W.J. Marciano and Z. Parsa, Phys. Rev. **D53**, 1 (1996).
14. Particle Data Group, K. Hagiwara *et al.*, Phys. Rev. **D66**, 010001 (2002).
15. A.J. Buras, M.E. Lautenbacher, and G. Ostermaier, Phys. Rev. **D50**, 3433 (1994).
16. D. Rein and L.M. Sehgal, Phys. Rev. **D39**, 3325 (1989); J.S. Hagelin and L.S. Littenberg, Prog. Part. Nucl. Phys. **23**, 1 (1989); M. Lu and M.B. Wise, Phys. Lett. **B324**, 461 (1994); S. Fajfer, arXiv:hep-ph/9602322 (1996); C.Q. Geng, I.J. Hsu, and Y.C. Lin, Phys. Rev. **D54**, 877 (1996).
17. A. J. Buras, M. Gorbahn, U. Haisch and U. Nierste, arXiv:hep-ph/0508165.
18. G. Isidori, F. Mescia and C. Smith, Nucl. Phys. B **718**, 319 (2005)[arXiv:hep-ph/0503107].
19. K. Anikeev *et al.*, Workshop Report "B Physics at the Tevatron: Run II and Beyond", arXiv:hep-ph/0201071 (2002).
20. R. J. Oakes, Phys. Rev. **183**, 1520 (1969).
21. U. Camerini *et al.*, Phys. Rev. Lett. **23**, 326 (1969).
22. D. Ljung and D. Cline, Phys. Rev. **D8**, 1307 (1973).
23. J.H. Klems, R.H. Hildebrand, and R. Steining, Phys. Rev. **D4**, 66 (1971).
24. G.D. Cable *et al.*, Phys. Rev. **D8**, 3807 (1973).
25. A. Belyaev *et al.*, Kaon Physics working Group Report "Kaon Physics with a High-intensity Proton Driver", arXiv:hep-ph/0107046 (2001); G. Isidori, arXiv:hep-ph/0110255 (2001); G. Buchalla, arXiv:hep-ph/0110313 (2001).
26. A.J. Buras, arXiv:hep-ph/0402191 (2004); G. Isidori, arXiv:hep-ph/0301159 (2003).
27. A.J. Buras *et al.*, arXiv:hep-ph/0402112 (2004); A.J. Buras *et al.*, arXiv:hep-ph/0408142 (2004).
28. Y. Grossman and Y. Nir, Phys. Lett. **B398**, 163 (1997).
29. F. Wilczek, Phys. Rev. Lett. **49**, 1549 (1982); J.L. Feng *et al.*, Phys. Rev. **D57**, 5875 (1998).
30. Y. Asano *et al.*, Phys. Lett., **B107**, 159 (1981).
31. M.S. Atiya *et al.*, Nucl. Instr. Meth. **A321**, 129 (1992).
32. S. Adler *et al.*, Phys. Rev. Lett. **76**, 1421 (1996).
33. M.S. Atiya *et al.*, Phys. Rev. **D48**, R1 (1993).
34. S. Adler *et al.*, Phys. Rev. Lett. **79**, 2204 (1997).
35. S. Adler *et al.*, Phys. Rev. Lett. **88**, 041803 (2002); S. Adler *et al.*, Phys. Rev. Lett. **84**, 3768 (2000);
36. B. Bassalleck *et al.*, E949 proposal, BNL-67247, TRI-PP-00-06 (1999), <http://www.phy.bnl.gov/e949/>.
37. T. Yoshioka *et al.*, IEEE Trans. Nucl. Sci. **51**, 199 (2004).
38. J. Doornbos *et al.*, Nucl. Instr. Meth. **A444**, 546 (2000).
39. D.A. Bryman *et al.*, Nucl. Instr. Meth. **A396**, 394 (1997).
40. M. Atiya *et al.*, Nucl. Instr. Meth. **A279**, 180 (1989).
41. E.W. Blackmore *et al.*, Nucl. Instr. Meth. **A404**, 295 (1998).
42. R.A. McPherson, "Chasing the Rare Decay $K^+ \rightarrow \pi^+ \nu \bar{\nu}$ ", Princeton University, Ph.D. Thesis, November, 1995.

43. I.H. Chiang *et al.*, IEEE Trans. Nucl. Sci. **42**, 394 (1995).
44. T.K. Komatsubara *et al.*, Nucl. Instr. Meth. **A404**, 315 (1998).
45. T. Yoshioka *et al.*, IEEE Trans. Nucl. Sci. **51**, 334 (2004).
46. blah blah
47. blah blah
48. blah blah
49. C. Caso *et al.*, European Physical Journal **C3**, 1 (1998).
50. P. Meyers, "A modified Version of the UMC Multiple Scattering Routine MSCAT1", E787 Technical Note No.77 (1985). Unpublished.
51. A.J. Stevens, "Nuclear Interactions in CH revisited", E787 Technical Note No.140 (1987). Unpublished.
52. W.R. Nelson *et al.*, "The EGS4 Code System", SLAC 265, SLAC (1985).
53. T. Sekiguchi, "Development of Silicon Strip Detector for Rare Kaon Decay Experiments", University of Tokyo, Master Thesis, January, 2002.
54. N. Khovansky *et al.*, NIM. A351 (1994), 317
55. J.B. Birks, Proc. Phys. Soc. **A64**, 874 (1951).
56. The reference manual can be found in
<http://paw.web.cern.ch/paw/mlpfit/pawmlp.html>.
The PDF version of the reference manual can also be available in
<http://schwind.home.cern.ch/schwind/MLPfit/doc/pawmlp.pdf>.
57. S. Adler *et al.*, Phys. Rev. Lett. **85**, 2256 (2000); M.R. Convery, "First Measurement of Structure Dependent $K^+ \rightarrow \mu^+ \nu_\mu \gamma$ ", Princeton University, Ph.D. Thesis, November, 1996.
58. T. Junk, Nucl. Instr. Meth. **A434**, 435 (1999).
59. The branching ratio published by the E949 collaboration (V.V. Anisimovsky *et al.*, Phys. Rev. Lett. **93**, 031801 (2004)), $(1.47^{+1.30}_{-0.89}) \times 10^{-10}$, was based on a statistical technique developed by T. Junk[58].
60. This definition of the central value of the branching ratio has the desirable feature that in the limit of N_{obs} observed candidates with high signal-to-background, the central value is the same as that given by the product of the sensitivity (Section 3.8) and N_{obs} which is the fundamental definition of the branching fraction.
61. G.J. Feldman and R.D. Cousins, Phys. Rev. **D57**, 3873 (1998).
62. CKMfitter Group (J.Charles *et al.*, Eur. Phys. J. **C41**, 1, (2005), arXiv:hep-ph/0406184, updated results and plots available at <http://ckmfitter.in2p3.fr>.
63. D. Bryman *et al.*, Int. J. Mod. Phys., **A21**, 487 (2006).